Direct Yaw Moment Control for Electric Vehicles with Independent Motors

by

Chunyun Fu

B. Eng.

A thesis submitted in fulfillment of the requirements for the degree of
Doctor of Philosophy (Mechanical and Manufacturing Engineering)

at the

School of Aerospace, Mechanical and Manufacturing Engineering
College of Science, Engineering and Health
RMIT University

August 2014

Declaration of Authorship

I, Chunyun Fu, declare that:

- Except where due acknowledgement has been made, the work is that of the candidate alone;

- The work has not been submitted previously, in whole or in part, to qualify for any other academic award;

- The content of the thesis is the result of work which has been carried out since the official commencement date of the approved research program;

- Any editorial work, paid or unpaid, carried out by a third party is acknowledged.

Signed:

Date: 25 August 2014

Dedicated to my beloved family.

Acknowledgements

Contents

List of Figures

List of Tables

Abbreviations

2WD	**2**-**W**heel-**D**rive
2WS	**2**-**W**heel-**S**teering
4WD	**4**-**W**heel-**D**rive
4WS	**4**-**W**heel-**S**teering
ABS	**A**nti-lock **B**raking **S**ystem
AFS	**A**ctive **F**ront-wheel **S**teering
ARCS	**A**ctive **R**oll **C**ontrol **S**ystem
CVT	**C**ontinuously **V**ariable **T**ransmission
DoF	**D**egree-**o**f-**F**reedom
DYC	**D**irect **Y**aw-moment **C**ontrol
ECU	**E**lectronic **C**ontrol **U**nit
ESC	**E**lectronic **S**tability **C**ontrol
ESP	**E**lectronic **S**tability **P**rogram
HEV	**H**ybrid **E**lectric **V**ehicle
HIL	**H**ardware-**I**n-the-**L**oop
I	**I**ntegral
ICC	**I**ntegrated **C**hassis **C**ontrol
ICE	**I**nternal **C**ombustion **E**ngine
LQR	**L**inear **Q**uadratic **R**egulator
LSD	**L**imited **S**lip **D**ifferential
MRAS	**M**odel **R**eference **A**daptive **S**ystem
PD	**P**roportional-**D**erivative
PI	**P**roportional-**I**ntegral
PID	**P**roportional-**I**ntegral-**D**erivative
PMBDCM	**P**ermanent **M**agnet **B**rushless **D**irect **C**urrent Motor

RNN   **R**ecurrent **N**eural **N**etwork

SMO   **S**liding **M**ode **O**bserver

TCS   **T**raction **C**ontrol **S**ystem

TTC   **T**ire **T**est **C**onsortium

VDC   **V**ehicle **D**ynamics **C**ontrol

VSC   **V**ehicle **S**tability **C**ontrol

WLS   **W**eighted **L**east **S**quare

Publications

CONFERENCE PAPERS

- **C. Fu**, R. Hoseinnezhad, S. Watkins, and R. N. Jazar, "Direct torque control for electronic differential in an electric racing car," in *Proceedings - 4th International Conference on Sustainable Automotive Technologies, ICSAT 2012*, Melbourne, Australia, 2012, pp. 177-183.

- **C. Fu**, R. Hoseinnezhad, R. N. Jazar, A. Bab-Hadiashar, and S. Watkins, "Electronic differential design for vehicle side-slip control," in *Proceedings - 2012 International Conference on Control, Automation and Information Sciences, ICCAIS 2012*, Ho Chi Minh City, Vietnam, 2012, pp. 306-310.

JOURNAL PAPERS

- **C. Fu**, R. Hoseinnezhad, and A. Bab-Hadiashar, "Side-slip control for nonlinear vehicle dynamics by electronic differentials," *Nonlinear Engineering*, vol. 1, no. 1-2, pp. 1-10, 2012.

- **C. Fu**, R. Hoseinnezhad, A. Bab-Hadiashar, R. N. Jazar, and S. Watkins, "Electronic differential for high-performance electric vehicles with independent driving motors," *International Journal of Electric and Hybrid Vehicles*, vol. 6, no. 2, pp. 108-132, 2014.

- M. Hu, H. Xie, and **C. Fu**, "Study on EV transmission system parameter design based on vehicle dynamic performance," *International Journal of Electric and Hybrid Vehicles*, vol. 6, no. 2, pp. 133-151, 2014.

- **C. Fu**, R. Hoseinnezhad, A. Bab-Hadiashar, and R. N. Jazar, "Direct yaw moment control for electric and hybrid vehicles with independent motors," *International Journal of Vehicle Design*, accepted.

- M. Hu, J. Zeng, S. Xu, **C. Fu**, and D. Qin "Efficiency study of a dual-motor coupling EV powertrain," *IEEE Transactions on Vehicular Technology*, accepted, doi: 10.1109/TVT.2014.2347349.

- **C. Fu**, R. Hoseinnezhad, A. Bab-Hadiashar, and R. N. Jazar, "Electric vehicle side-slip control via electronic differential," submitted to *International Journal of Vehicle Autonomous Systems*.

Abstract

Direct Yaw Moment Control (DYC) systems generate a corrective yaw moment to alter the vehicle dynamics by means of active distribution of the longitudinal tire forces, and they have been proven to be an effective means to enhance the vehicle handling and stability. The latest type of DYC systems employs the on-board electric motors of electric or hybrid vehicles to generate the corrective yaw moment, and it has presented itself as a more effective approach than the conventional DYC schemes.

In this thesis, a wide range of existing vehicle dynamics control designs, especially the typical DYC solutions, are investigated. The theories and principles behind these control methods are summarized, and the features of each control scheme are highlighted. Then, a full vehicle model including the vehicle equivalent mechanical model, vehicle equations of motion, wheel equation of motion and *Magic Formula* tire model is established.

Using the derived vehicle equations of motion, the fundamental mathematical relationships between the corrective yaw moment produced by the DYC system and the crucial vehicle states (the yaw rate and vehicle side-slip) are derived. Based on these relationships, two DYC systems are proposed for electric vehicles (or hybrid vehicles) by means of individual control of the independent driving motors. These two systems are designed to track the desired yaw rate and vehicle side-slip, respectively. Extensive simulation results verify that these systems are effective in improving vehicle dynamic performance.

Apart from the two systems that adjust yaw rate or vehicle side-slip individually, a novel sliding mode DYC scheme is proposed to regulate both vehicle states simultaneously, aiming to better enhance the vehicle handling and stability. This control scheme guarantees the simultaneous convergences of both the yaw rate and vehicle side-slip errors to zero, and eliminates the limitations presented in the common sliding mode DYC solutions. Comparative simulation results indicate that the vehicle handling and stability are significantly enhanced with the proposed DYC system on-board. Also, this DYC scheme is shown to outperform its corresponding counterparts in various driving conditions.

Chapter 1

Introduction

1.1 BACKGROUND AND SCOPE

Not long ago, restricted by the control techniques of the day, the braking torques generated by a vehicle braking system were evenly distributed between the left and right wheels. Also, the driving torque produced by an Internal Combustion Engine (ICE) was transferred equally to the left and right driving wheels, or mechanically altered between the left and right wheels using, for example, a Torsen differential. As a result, the longitudinal tire forces (braking or traction forces) were not utilized to actively generate yaw moments to regulate the vehicle motions. Yaw moments were, at large, generated by the lateral tire forces through tire slip angles during steering motions.

The lack of control on yaw moment has brought about some problems. In some critical driving scenarios (e.g. the vehicle enters a road with uneven surface conditions or the vehicle corners sharply at a high speed), the yaw moment that is naturally generated by the lateral tire forces may be excessive or insufficient to keep the vehicle stable, and can result in accidents. On the other hand, passenger cars are normally designed to have understeer characteristic to gain more stability margin. Note that the level of understeer varies as the driving condition changes. For example, if the lateral load transfer of the front wheels is greater than that of the rear wheels, then the level of understeer intensifies; otherwise the level of understeer attenuates. In extreme cases, the lateral load transfer can even force the vehicle to switch from understeer to oversteer. A conventional vehicle cannot consistently remain in a desirable steer characteristic, say, neutral steer.

In view of the above problems, several types of electronic control systems have been proposed in the last three decades, aiming to regulate the vehicle yaw motion by means of active distribution of longitudinal tire forces (both braking and traction forces). A

(a) ESP configuration (b) ESP components
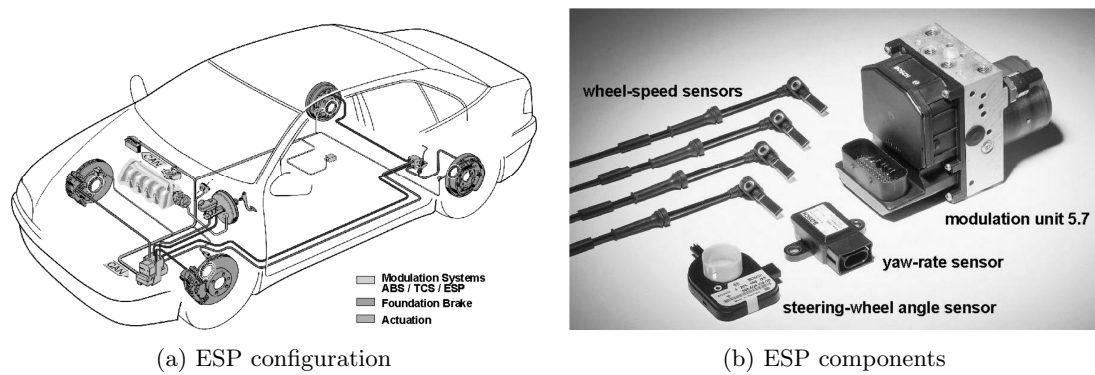
FIGURE 1.1: Bosch ESP system [6].

yaw moment is directly generated through individual control of longitudinal tire forces. Thus, these systems are normally termed as direct yaw moment control systems [1].

1.1.1 Vehicle stability control

The most popular type of DYC is the Vehicle Stability Control (VSC) systems. They are sometimes referred to as the Vehicle Dynamics Control (VDC), Electronic Stability Control (ESC) or Electronic Stability Program (ESP). The VSC systems apply individual braking torques to each wheel to produce a corrective yaw moment, in order to prevent the vehicle from spinning or drifting out in critical situations. It is shown in [2–4] that VSC systems have significantly reduced the incidence of traffic accidents. So far, the VSC systems have been the most adopted type of DYC and they have become mandatory fitments on new cars in some countries.

The first VSC system was the Bosch ESP introduced in 1995 for the Mercedes-Benz S-Class sedans [5]. Since then, the Bosch ESP has been widely employed by many vehicle manufacturers and has become the most popular VSC system. A schematic of the Bosch ESP is shown in Figure 1.1. This Bosch ESP employs the components of the already available Anti-lock Braking System (ABS) and Traction Control System (TCS), as well as several additional sensors, to apply individual braking torque to each wheel and control the engine torque output [6].

The core of all VSC systems is the corrective yaw moment generated via active distribution of individual braking forces. The braking motions inevitably give rise to deceleration and loss of vehicle speed, which may be intrusive to the driver [7, 8]. Besides, the engine driving torque cannot be actively distributed between the driving wheels by VSC systems. In other words, as a braking-based system, the VSC mainly operates in dangerous situations where the vehicle is about to lose control, however in normal driving
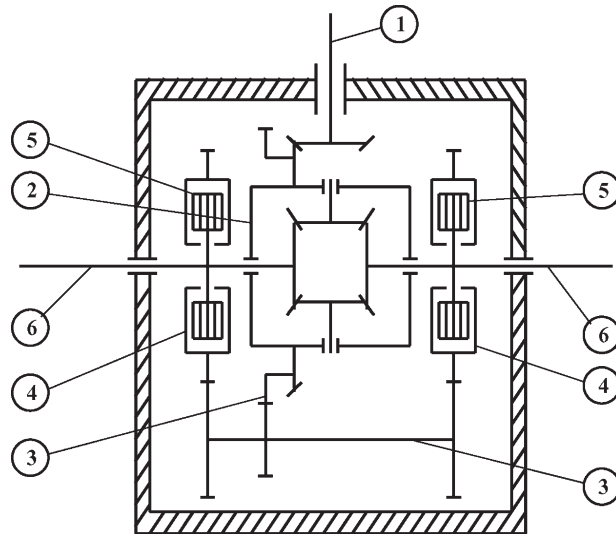
FIGURE 1.2: Schematic of an example rear active differential [9]. 1 - input shaft, 2 - bevel gear differential, 3 - additional gearing, 4 - clutch housings, 5 - clutch disks, 6 - output axles.

conditions, VSC systems cannot work continuously to adjust the driving (traction) force on each wheel to enhance the vehicle handling.

1.1.2 Actively controlled mechanical differentials

The second type of DYC systems is the actively controlled mechanical differentials (hereafter called active differentials for short). Compared to the braking-based VSC systems, these active differentials control individually the driving torques delivered to the left and right driving axles, and in turn generate a yaw moment to improve the vehicle handling. Also, they operate continuously in various driving conditions rather than work only in critical situations. This type of DYC is generally a combination of one conventional open differential and two electronically controlled clutches [7–10], as schematically shown in Figure 1.2. The input torque from the engine is transmitted to the conventional bevel gear differential through the input shaft. When torque transfer is needed, one of the clutches will be engaged to alter the torques delivered to the left and right axles.

Unlike the conventional Limited Slip Differentials (LSD) which always transfer torque to the slower wheel, the active differentials are able to control both the magnitude and direction of the torque transfer [7, 8]. Also, the magnitude of the torque transfer can be any value within the saturation limit, regardless of the input driving torque and wheel angular velocities [7, 9]. The asymmetric driving torques on the left and right wheels bring about a yaw moment which is tuned to improve the vehicle handling.
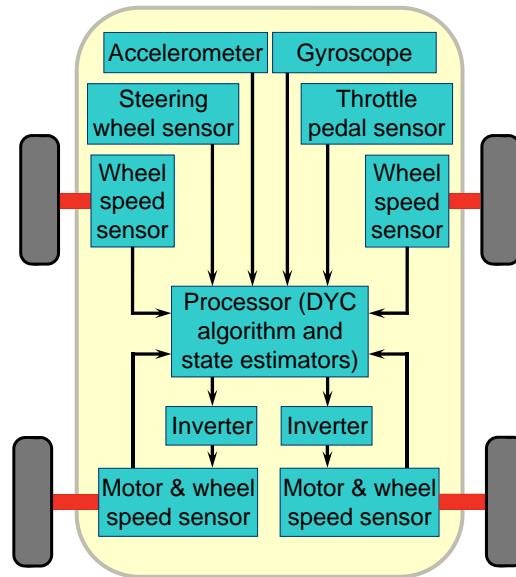
FIGURE 1.3: Schematic of a typical DYC system for an electric/hybrid vehicle equipped with independent rear motors.

Active differentials present themselves as good solutions to enhancing the vehicle handling, however they still have a number of shortcomings. Firstly, the need for two electronically controlled clutches to manage the torque transfer between the left and right driving axles complicates the differential structure and adds extra weight to the vehicle. Secondly, the dynamics of clutch engagement (which is commonly actuated by an electro-hydraulic system [9, 11] or an electro-magnetic system [7]) is relatively slow, compared to electric motors which are employed to constitute the latest type of DYC (see next section). Furthermore, when the speed difference between the left and right wheels is sufficiently large, torque transfer becomes possible to only one of the wheels [8, 10, 12], i.e. the direction of torque transfer is no longer controllable. Lastly, the sliding of the clutch disks inevitably results in energy loss.

1.1.3 Direct yaw moment control using independent electric motors

The latest type of DYC employs electric motors to generate a corrective yaw moment through individual control of longitudinal tire forces. This type of DYC is mainly designed for electric vehicles or hybrid vehicles equipped with independent driving motors. Figure 1.3 shows the schematic of a typical DYC system of such type. The processor of the control system receives signals from different on-board sensors, such as the gyroscope and throttle pedal sensor. Based on the sensor signals and state observation information, the processor calculates the left and right motor torque commands according to the DYC algorithm. Then the torque commands are sent to the inverters to drive the electric motors.

Thanks to the independent electric motor configuration, this new DYC type presents several advantages over the aforesaid two types of DYC:

- Unlike the braking-based VSC systems, the new DYC systems do not result in undesirable deceleration and loss of vehicle speed.

- The new DYC systems generate continuous corrective yaw moment to enhance the vehicle handling and stability at all times, as opposed to operating only in critical driving conditions.

- The generation of motor torque is swift and accurate, and the motor torque is measurable. These attributes facilitate the design and implementation of DYC schemes.

- The effectiveness of the new DYC systems does not depend on the speed difference between the left and right wheels.

- The elimination of clutches makes the new DYC type more energy efficient as no energy is dissipated in friction.

- Motors can generate negative torque in the electrical braking mode [13], which assists the conventional braking system and enhances energy efficiency by regenerative braking.

The above advantages have attracted increasing research focus on this new DYC type in the recent literature [14–16]. Along with the development of electric and hybrid vehicles with independent motors, this DYC type has presented itself as a promising approach to enhancing the vehicle handling and stability. Thus, the scope of this thesis is focused on these new DYC systems. Specifically, this study looks into the DYC design for electric and hybrid vehicles with two independent rear driving motors, as schematically shown in Figure 1.3.

1.2 RESEARCH QUESTIONS

1.2.1 Control variables

How to produce a desirable yaw moment that would enhance the vehicle handling and stability has been widely discussed in the published DYC solutions. In general, the existing DYC methods employ the yaw rate and/or vehicle side-slip as the main control variable(s), since these two vehicle states have been shown to be the fundamental states
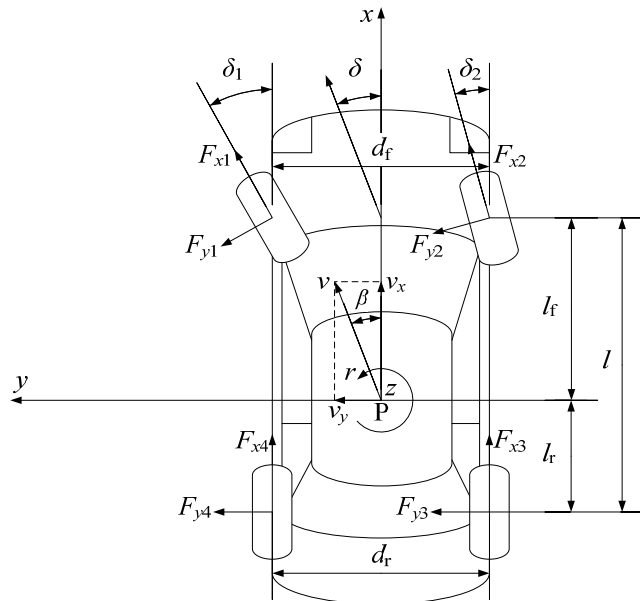
FIGURE 1.4: Vehicle top view.

that govern vehicle handling and stability [17–19]. As shown in Figure 1.4, the yaw rate (denoted by r) is the vehicle angular velocity about the z axis of the vehicle local coordinate x-y-z (the establishment of coordinate x-y-z will be introduced in Chapter 3), and the vehicle side-slip (denoted by β) is the angle between the vehicle heading direction (the positive direction of the x axis in the vehicle local coordinate x-y-z) and the velocity vector $\boldsymbol{v}$ of point P[1].

The yaw rate plays a crucial roll in vehicle dynamics control. Firstly, the steady-state yaw rate (derived from the common bicycle model [20]) is a function of the front wheel steer angle. Thus, it can be interpreted as the vehicle response desired by the driver. Secondly, this steady-state yaw rate value defines the steer characteristic (i.e. under, over, or neutral steer) of the vehicle. For these reasons, the yaw rate is closely related to the vehicle handling and it should be selected as one of the major control variables.

The vehicle side-slip is also an essential vehicle state which, ideally, requires to be minimized. It has been shown that as the vehicle side-slip increases to large values, the yaw moment generated by the lateral tire forces generally descends [21]. When the vehicle side-slip is sufficiently large, the generated yaw moment becomes negligible and it can hardly be increased by changing the steer angle. Thus, the vehicle tends to lose its stability. Besides, a small vehicle side-slip implies a consistency of the vehicle heading direction with the velocity vector $\boldsymbol{v}$, which provides the driver with superior sense of control during cornering [22]. Due to the above reasons, the vehicle side-slip is closely

---

[1]P is a point under the vehicle mass center. See page 37 for the detailed explanation on P.

connected to the vehicle stability and driver's sense of control, and it should also be chosen as the control variable.

Note that even though the yaw rate is more related to the vehicle handling and the vehicle side-slip is mainly connected to the vehicle stability, these two vehicle states are not independent, instead, they are intrinsically related by the vehicle dynamics (see vehicle equations of motion in Chapter 3). Hence, they both affect the vehicle handling and stability.

1.2.2   Research questions

Various DYC designs for controlling one or both of the above states have been introduced in the literature. However, a basic question is often neglected by researchers and it has not been well answered, which is: How does the additional yaw moment produced by a DYC system change vehicle dynamics, i.e., what are the mathematical relationships between the additional yaw moment and the vehicle states (yaw rate and vehicle side-slip)?

The discovery of the above fundamental mathematical relationships should reveal the essence of a DYC system, which leads to the second research question: How to design a yaw rate-based or vehicle side-slip-based DYC system, based on the derived fundamental mathematical relationships?

In order to improve DYC robustness as well as combine the benefits of controlling the yaw rate and vehicle side-slip individually, many recent DYC works adopt both states simultaneously as the control variables and such solutions have exhibited superior control performance to the systems controlling one state only [17, 23–26]. However, in some certain scenarios these solutions still present some imperfections and limitations. Thus, the third research question is: How to design a DYC system to control both the yaw rate and vehicle side-slip simultaneously, to improve the performance of the state-of-the-art DYC systems?

The objectives of this thesis are to answer the above three research questions through mathematical derivations and new DYC designs, and verify the proposed schemes by means of extensive computer simulations. The following chapters will elaborate on the design processes and verifications of the proposed DYC systems.

1.3   CONTRIBUTIONS

The contributions of this study lie in three aspects. First of all, the fundamental mathematical correlations between the vehicle states (i.e. yaw rate and vehicle side-slip) and the additional yaw moment generated by the DYC system are formulated and analyzed. These relationships reveal how the DYC system influences the vehicle dynamics and provide implications for controller design. Secondly, based on the discovered relationships, a yaw rate-based DYC system and a vehicle side-slip-based DYC system are proposed. These systems are verified through extensive simulations to be effective in tracking the desired yaw rate and desired vehicle side-slip, respectively. Lastly, a novel sliding mode DYC scheme controlling both vehicle states is proposed to enhance the control performance of the existing sliding mode DYC methods. Extensive simulations demonstrate that the proposed method provides superior control performance to the conventional solutions.

1.4   THESIS OUTLINE

This thesis consists of seven chapters. In Chapter 1, an introduction to the research background, research scope and research questions is given. Then in Chapter 2, a comprehensive literature review of various types of DYC systems, from the very basic systems to the state-of-the-art DYC solutions, is presented.

In Chapter 3, a full vehicle model including the vehicle equivalent mechanical model, vehicle equations of motion, wheel equation of motion and *Magic Formula* tire model is established. The vehicle equations of motion governing the vehicle longitudinal, lateral, roll and yaw motions are employed in Chapters 4–6 for DYC system design. The full vehicle model is programed in MATLAB/Simulink environment to generate simulation results.

In Chapter 4, based on the investigation of the vehicle equations of motion, a fundamental mathematical relation governing the yaw dynamics with a DYC system on-board is derived. Based on this relationship, a yaw rate-based DYC system which aims to achieve neutral steer performance is proposed. In Chapter 5, a similar mathematical equation is derived for vehicle side-slip, based on which a vehicle side-slip-based DYC system that tracks zero side-slip is devised. The yaw rate and vehicle side-slip-based DYC systems are verified through computer simulations to be effective in improving the vehicle handling and stability, respectively.

In Chapter 6, a new sliding mode-based DYC method is proposed for simultaneous tracking of the desired yaw rate and vehicle side-slip. This DYC scheme directly employs the complete nonlinear vehicle equations of motion established in Chapter 3 without simplification to achieve a more effective control law. Also, the proposed DYC design introduces a novel switching function that guarantees simultaneous convergences of both the yaw rate and vehicle side-slip errors to zero. The effectiveness of the proposed DYC in enhancing the vehicle handling and stability is verified through comparative simulations in various challenging driving scenarios.

In Chapter 7, conclusions on the entire study are given and recommendations for future work are presented.

Chapter 2

Literature Review

In this chapter, a comprehensive literature review of various types of DYC systems is presented. Based on the control variable(s) used, the DYC systems are classified into three main categories: the yaw rate-based DYC, the vehicle side-slip-based DYC and the simultaneous control of the yaw rate and vehicle side-slip. In order to show how DYC systems have evolved, two basic types of control systems for managing independent electric motors, the equal torque methods and Ackerman methods, are introduced first. For each type of control methods, the theoretical concepts and principles are summarized, the features and characteristics are highlighted, and their control performances are analyzed. This literature review lays the foundation for the analysis in the subsequent chapters.

2.1   EQUAL TORQUE METHODS

The most straightforward way of controlling two independent motors is to send equal torque commands to the two motors. The control methods using this approach are referred to as the equal torque methods, and they emulate the behavior of an open differential (the most used mechanical differential) which applies equal torques to both wheels and allows speed differentiation at the same time. The equal torque methods provide the electric vehicle with a cornering performance similar to an ICE vehicle equipped with an open differential. Note that the equal torque methods cannot be categorized as DYC systems, as no active yaw moment is generated to regulate the vehicle motions. They are introduced here to show how simple control solutions evolved to sophisticated DYC systems to enhance the control performance.

Magallán et al. proposed an equal torque method in their works [27, 28], as schematically shown in Figure 2.1. In this solution, the torque commands sent to the motors are
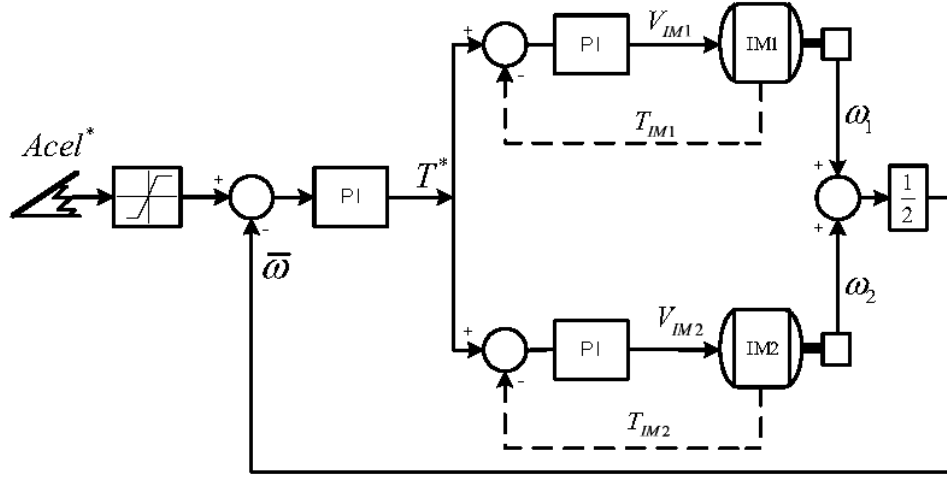
FIGURE 2.1: An example equal torque method [27, 28].

determined based on the difference between the speed required by the driver (read from the throttle pedal and denoted by $Acel^*$) and the average of the two driving wheel speeds (denoted by $\bar{\omega}$). The speed error is then sent to a Proportional-Integral (PI) controller to generate equal torque references for the two motor controllers.

When a vehicle is driving at a very low speed and does not have wheel slips, the average of the two driving wheel speeds is proportional to the vehicle longitudinal speed and the open differential behavior is reproduced by the proposed method in [27, 28]. However, when the vehicle is running very fast or in driving conditions involving relatively high wheel slips, the average of the two driving wheel speeds is no longer proportional to the vehicle longitudinal speed. As a result, the proposed equal torque method would not generate proper driving commands. For instance, when one driving wheel is locked, the other one will be sped up to twice the reference speed [27, 28], resulting in severe tire slip and undesirable yaw moment.

To solve this problem, a modified equal torque method with self-blocking function is proposed in [28], as schematically shown in Figure 2.2. When the speed difference between the two driving wheels is not excessively large (i.e. the speed ratio does not exceed 1.5), the control system works in the same way as the original equal torque method introduced above. Once the speed ratio reaches 1.5, the self-blocking control is activated and the feedback signal for the PI controller is switched to the larger wheel speed. By this means, the wheel speed of the faster wheel is maintained in a safe region.

Apart from the above schemes, other equal torque methods are also proposed in the literature, such as [29–33]. All these methods share the feature of sending the same torque commands to the driving motors. They present themselves as the most straightforward approach to controlling two independent motors, and bring benefits to the vehicle such
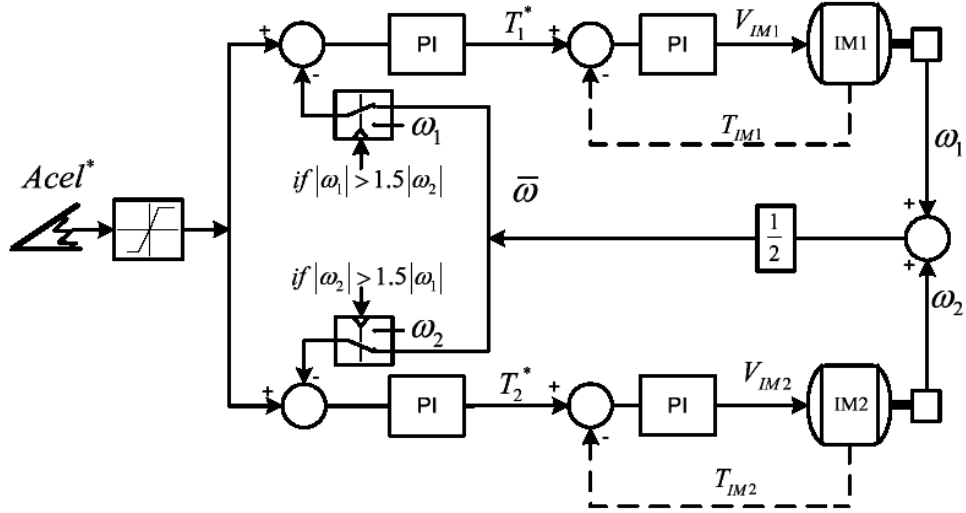
FIGURE 2.2: An example equal torque method with self-blocking function [28].

as swift torque response, reduction in mechanical parts and friction. However, as the system constantly delivers equal torques to the driving wheels, the dynamic performance of the electric vehicle is similar to the normal ICE vehicles with open differentials and the independent motor configuration is not fully exploited for improving the vehicle dynamic performance.

2.2 ACKERMAN METHODS

2.2.1 Background

When a vehicle runs at a very low speed, the well-known Ackerman steering geometry [34, 35] enables the inner and outer wheels to spin without wheel slips. The Ackerman steering geometry is shown in Figure 2.3, and it is mathematically expressed by:

$$\cot \delta_2 - \cot \delta_1 = \frac{d_\mathrm{r}}{l}, \tag{2.1}$$

where d_r denotes the rear track width, l represents the wheel base, and δ_1 and δ_2 are the steer angles of the front left and front right wheels, respectively. When the vehicle speed is very low, the centrifugal force applied on the vehicle is negligible and no lateral tire forces are generated. As a result, the tire slip angles are zero and the turning radius O is on the extension of the rear axle, as shown in Figure 2.3.

Given that the Ackerman steering geometry is satisfied and the vehicle runs very slow, the desired angular velocities of the left and right rear driving wheels without any slips,
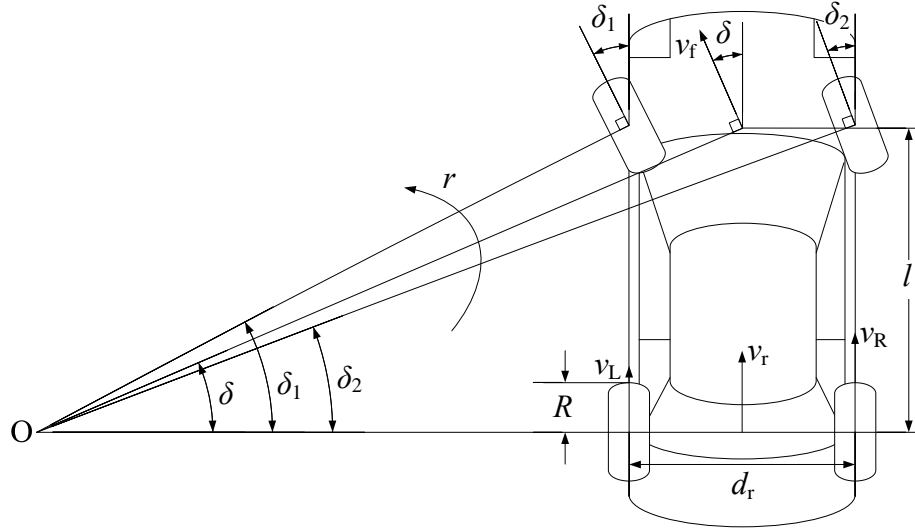
FIGURE 2.3: Ackerman steering geometry.

ω_L and ω_R, are derived as follows:

$$\omega_L = \frac{v_L}{R} = \frac{v_r}{R}(1 - \frac{d_r \tan \delta}{2l}) \tag{2.2}$$

$$\omega_R = \frac{v_R}{R} = \frac{v_r}{R}(1 + \frac{d_r \tan \delta}{2l}), \tag{2.3}$$

where R represents the tire radius, δ stands for the front wheel steer angle (cot-average of the left and right front wheel steer angles, i.e. $\cot \delta = (\cot \delta_1 + \cot \delta_2)/2$), v_r denotes the velocity of the rear axle center, and v_L and v_R are the velocities of the left and right rear wheel centers, respectively.

It has been proven by simulation [36] and experimentally [37] that at low speed equations (2.2) and (2.3) predict the actual wheel angular velocities with satisfactory accuracy. As a result, maintaining the wheel angular velocities at the these desired levels has become the main objective of many existing solutions for controlling independent motors on electric vehicles [38–46]. These control systems are often referred to as the "electric differential", "electrical differential" or "electronic differential" in the literature. In this study, they are all categorized as the Ackerman methods.

All Ackerman methods share the same working principle: when an electric vehicle enters a corner, the control system acts immediately on both motors, reducing the angular velocity of the inner wheel while increasing that of the outer wheel [38] to their desired values defined by equations (2.2) and (2.3). Note that to track these desired angular velocity values, the knowledge of the actual angular velocities, vehicle velocity and front wheel steer angle is required.

The Ackerman methods focus on the regulation of the driving wheel angular velocities, as opposed to the yaw moment. Although a yaw moment may be generated by the
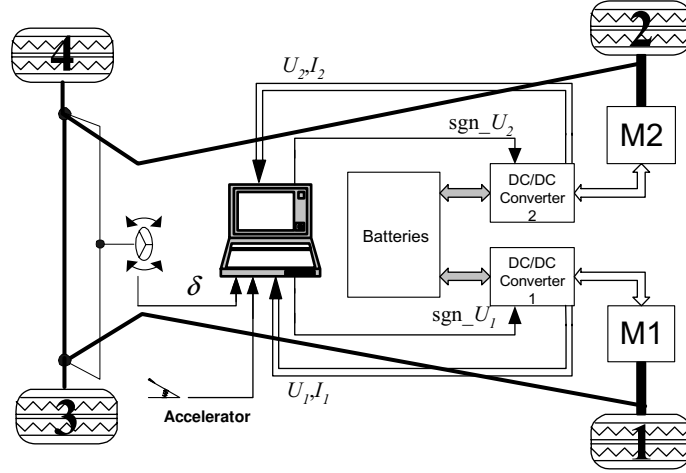
FIGURE 2.4: Electric vehicle configuration proposed by Cordeiro et al. [39].

control methods in the course of angular velocity regulation, the moment is not directly controlled. Thus, the Ackerman methods are not categorized as DYC systems, either. They are introduced here to show how control solutions evolved from simple methods to sophisticated DYC systems.

2.2.2 Control methods based on Ackerman steering geometry

Cordeiro et al. [39] designed a control scheme that employs the Ackerman steering geometry to control two independent DC motors. The proposed electric vehicle features two independent permanent magnet brushed DC motors fed by two classic DC-DC converters, as shown in Figure 2.4. The Ackerman steering geometry is utilized to calculate the reference angular velocities for the left and right driving wheels. The actual angular velocities are estimated using the knowledge of the motor parameters and the information from the motor voltage and current sensors. The reference and actual angular velocities of each wheel form the error for a sliding mode controller which drives the actual angular velocity towards the reference value. The switching function s for the sliding mode controller is a first-order differential equation expressed by:

$$s = \dot{e}_\omega + k_e e_\omega, \tag{2.4}$$

where e_ω is the angular velocity error and k_e is a design parameter. The global model (schematic) of the complete electrical drive is shown in Figure 2.5.

Haddoun et al. [40] devised an electrical differential control system for an electric vehicle with two independent induction motors for the rear wheels. In this design, the rotor speeds of the induction motors (thus the actual wheel angular velocities) are estimated using a speed estimation method based on a Recurrent Neural Network (RNN) with two
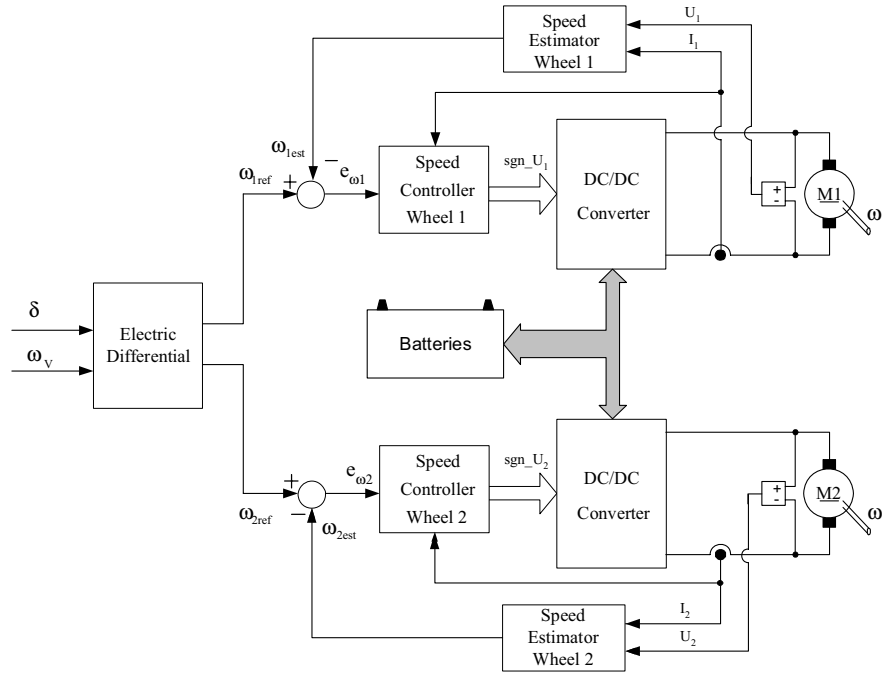
FIGURE 2.5: Electrical drive proposed by Cordeiro et al. [39].
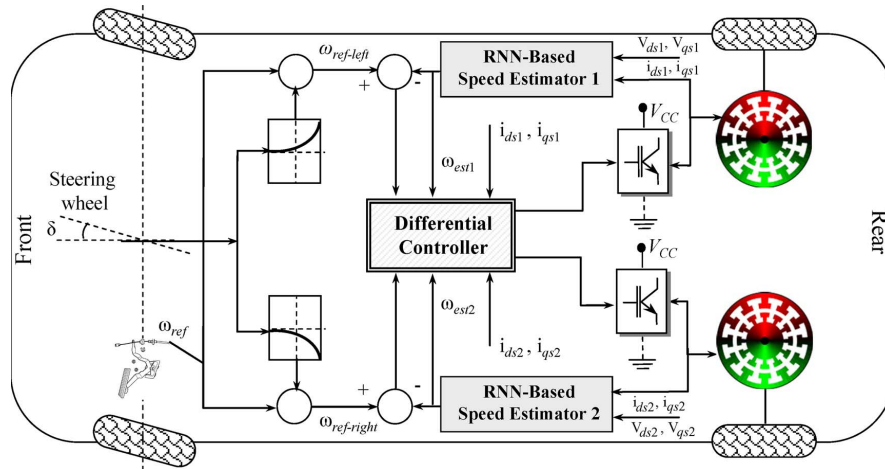
FIGURE 2.6: Schematic of electrical differential system proposed by Haddoun et al. [40].

hidden layers. The multilayer and recurrent structure of the neural network provides robustness against the parameter variations and system noise. The actual wheel angular velocities are regulated by the electrical differential system according to the Ackerman steering geometry. The schematic of the proposed electrical differential system is shown in Figure 2.6.

Haddoun et al. [41] proposed another Ackerman method employing equations (2.2) and (2.3) as the reference angular velocities. The main feature of this control scheme lies in the utilization of a motor speed observer based on the Model Reference Adaptive System (MRAS) approach which provides robustness against the external disturbances

and system uncertainties. The actual angular velocities are estimated by the MRAS-based observer, and are fed back to an electric differential system to regulate the wheel angular velocities.

In the works of Zhao et al. [42, 43], an electronic differential system is designed for an electric vehicle with two Permanent Magnet Brushless Direct Current Motors (PMBD-CMs). A fuzzy logic control algorithm is employed in this design to achieve the desired wheel angular velocities derived from the Ackerman steering geometry.

Perez-Pinal et al. [44] proposed an electric differential design for a rear-wheel-drive electric vehicle. This solution employs a motor synchronization control approach, aiming to prevent deviation from the desired vehicle path. The synchronization strategy is realized through a fictitious general master controller which provides each wheel with a speed reference based on the Ackerman steering geometry.

In the work of Nasri et al. [45], a fuzzy logic control scheme is applied to control the two independent induction motors to obtain better efficiency and enhanced robustness against the parameter variation. In this design, the Ackerman steering geometry is employed to compute the speed references for the two driving motors.

The Ackerman steering geometry can also be employed in the control designs for 4-Wheel-Drive (4WD) electric vehicles. Zhou et al. [46] developed an electronic differential system for controlling a prototype electric vehicle with four brushless DC in-wheel motors. When the vehicle moves in a straight line, this control system ensures that all wheels rotate at the same speed as the slowest one, if they are not consistent. When the vehicle makes a turn, the controller adjusts the wheel angular velocities to the desired levels derived from the Ackerman steering geometry. Meanwhile, the vehicle speed during cornering is held constant by the controller.

2.2.3 Remarks

It is important to note that the Ackerman steering geometry is a purely kinematic condition that is accurate only when the vehicle speed is very low. This is because the centrifugal force and tire slip angles are neglected in the Ackerman steering geometry. As a result, neither the tire cornering characteristics nor the vehicle dynamics is taken into account. On the other hand, the desired wheel angular velocities derived from the Ackerman steering geometry assume no wheel slips. In reality, wheel slips are ubiquitous in various driving conditions, and absolute zero wheel slip is impractical. For these reasons, control designs based on the Ackerman steering geometry are only suitable for

certain low-speed vehicle applications in which the tire slips are negligible during cornering. In the following chapters, simulation results obtained from high speed maneuvers will expose the inherent shortcomings of the Ackerman steering geometry-based control solutions.

2.3 YAW RATE-BASED DYC

2.3.1 Background

As discussed in the preceding sections, both the equal torque methods and Ackerman methods present obvious downsides and do not provide optimum control performances. This has led researchers to seek new control solutions towards making full advantage of independent driving motors and achieving better control performance. In this effort, various DYC designs have been proposed in the literature. The major advantage of DYC systems over the previous two types of methods is that they take the vehicle dynamics into account, and directly adjust the yaw moment generated by the individual motor torques to regulate the target vehicle state(s) and in turn remould the vehicle dynamics.

It has been pointed out in Chapter 1 that the yaw rate r plays a crucial role in vehicle dynamics and should be selected as the control variable in DYC systems. In the literature, numerous DYC designs have been proposed to drive the actual yaw rate towards a desired (reference) yaw rate value, aiming to enhance the vehicle handling and stability.

The vast majority of existing DYC solutions employ the steady-state yaw rate response (or its variation/modification) derived from the two Degree-of-Freedom (DoF) planar vehicle model (bicycle model) [20] as the desired (reference) yaw rate. This value can be expressed in the following general form [20, 35]:

$$r = \frac{v_x \delta}{l(1 + K v_x{}^2)},$$
(2.5)

where v_x denotes the vehicle longitudinal velocity, δ represents the front wheel steer angle, l stands for the wheel base, K is called the "stability factor" and given by:

$$K = \frac{m}{l^2}\left(\frac{l_{\mathrm{r}}}{C_{\alpha\mathrm{f}}} - \frac{l_{\mathrm{f}}}{C_{\alpha\mathrm{r}}}\right),$$
(2.6)

where m is the total vehicle mass, l_{f} and l_{r} are the distances from the mass center to the front axle and rear axle respectively, and $C_{\alpha\mathrm{f}}$ and $C_{\alpha\mathrm{r}}$ are the total cornering stiffnesses of the front tires and rear tires respectively.

On the one hand, the above steady-state yaw rate response is a reflection of the driver's control inputs. It is seen that the yaw rate r is a function of the front wheel steer angle δ and the vehicle longitudinal velocity v_x. Because δ is commanded by the driver through steering wheel and v_x is controlled by the driver via throttle or brake pedal, therefore the yaw rate response given by equation (2.5) can be interpreted as the steady-state vehicle response desired by the driver.

On the other hand, by means of vehicle turning radius, this yaw rate response defines the vehicle's steer characteristic which affects the vehicle handling and stability. The vehicle steady-state turning radius can be derived from the yaw rate response equation. Kinematically, the vehicle turning radius L is known as:

$$L = v/r, \tag{2.7}$$

where v denotes the resultant velocity of the mass center, and r represents the yaw rate. Since the velocity lateral component v_y is considerably smaller than the longitudinal component v_x, the turning radius can be approximated by:

$$L = v_x/r. \tag{2.8}$$

Substituting equation (2.5) in equation (2.8) leads to the following steady-state turning radius expression:

$$L = \frac{l(1 + Kv_x{}^2)}{\delta}. \tag{2.9}$$

When the stability factor K is positive, it is seen from equation (2.9) that for a certain front wheel steer angle δ the steady-state turning radius L increases with the longitudinal velocity v_x. This steer characteristic is defined as "understeer". The driver has to steer more if he/she wishes to keep the same turning radius when accelerating. An understeer vehicle is stable and safe, as it is "reluctant" to turn. Most vehicles are designed to understeer for safety purposes, but understeer is not optimum for the vehicle handling.

When the stability factor K is negative, the turning radius L drops as the longitudinal velocity v_x increases, for a certain steer angle δ. This steer characteristic is defined as "oversteer". An oversteer vehicle is unstable and dangerous, because when v_x increases to a certain value (i.e. critical speed [20]) the turning radius reaches zero and the vehicle spins about itself.

The last situation is "neutral steer", when $K = 0$. A neutral steer vehicle makes the turning radius L independent of the longitudinal velocity v_x. In other words, the driver does not need to change the steer angle to keep the same turning radius whenever the

vehicle accelerates or decelerates in a corner. Neutral steer is the ideal steer characteristic, as it not only keeps the vehicle stable but also provides good handling. However, it is impractical to constantly maintain neutral steer (i.e. $K = 0$) without any electronic systems, because the stability factor K is a function of the cornering stiffnesses $C_{\alpha f}$ and $C_{\alpha r}$ which constantly change with the driving condition.

To sum up, the steady-state yaw rate response, equation (2.5), not only represents the vehicle response commanded by the driver, but also influences the vehicle handling and stability through the stability factor K. In the following section, the typical yaw rate-based DYC solutions that employ equation (2.5) (or its variation/modification) as the desired (reference) response are reviewed. Note that apart from the yaw rate-based DYC systems with independent motor configuration, other typical yaw rate-based DYC solutions such as the differential braking systems and active differentials are also reviewed, since they share similar design principles and provide insights into new DYC design.

2.3.2 Typical yaw rate-based DYC methods

The yaw rate can be controlled by means of wheel slip ratio regulation. One such control scheme was designed by Doniselli et al. [47] for front-wheel-drive vehicles. The overall control structure is shown in Figure 2.7[1]. The front wheel steer angle δ, yaw rate r and vehicle longitudinal velocity v_x are employed in the main control law to calculate the following desired slip ratio difference between the left and right driving wheels:

$$\Delta\lambda^* = k_1(r - \frac{v_x\delta}{l}), \tag{2.10}$$

where l denotes the wheel base and k_1 represents a design parameter. Note that the term $\dfrac{v_x\delta}{l}$ in equation (2.10) is the yaw rate corresponding to neutral steer (stability factor $K = 0$). The desired slip ratio difference $\Delta\lambda^*$ and the actual slip ratio difference $\Delta\lambda$ are used by the torque split law to generate a correction torque M_c given by:

$$M_c = k_2(\Delta\lambda^* - \Delta\lambda), \tag{2.11}$$

where k_2 is another design parameter. This correction torque is scaled and then added to/subtracted from half the engine torque to form the torque inputs to the left and right driving wheels, as shown in Figure 2.7. An important feature of the main control law is

---

[1]Symbols u, Δs_x^* and Δs_x are used in [47] to denote the vehicle longitudinal velocity, desired slip ratio difference and actual slip ratio difference, respectively. In this thesis, to maintain consistent usage of symbols, v_x, $\Delta\lambda^*$ and $\Delta\lambda$ are employed instead of u, Δs_x^* and Δs_x.
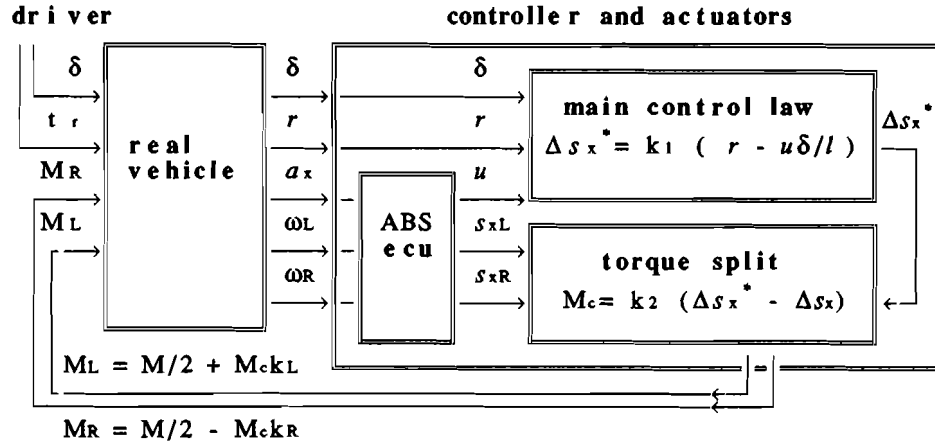
FIGURE 2.7: Schematic of torque split control proposed by Doniselli et al. [47].

that it sets the desired $\Delta\lambda^*$ in such a way that the vehicle steer characteristic becomes as close as possible to neutral steer.

The idea of controlling the yaw rate by means of wheel slip ratio regulation was also employed by Buckholtz [25]. In his design, an upper level fuzzy logic controller is proposed to track the desired yaw rate response by assigning an appropriate wheel slip ratio to each wheel. The input to this fuzzy logic controller is defined as:

$$d = \dot{e} + \gamma e, \tag{2.12}$$

where $e = |r| - |r^*|$ denotes the yaw rate error and γ is a design parameter. The outputs from this controller are the target (reference) wheel slip ratios for the four wheels. Four lower level controllers are adopted for the four wheels to track the target wheel slip ratios commanded by the upper level fuzzy logic controller, in order to generate the desired corrective yaw moment.

Tahami et al. [48] developed a stability enhancement system for a four-motor-wheel electric vehicle. This system employs a fuzzy logic controller to regulate the yaw rate, using equation (2.5) as the reference response r^*. A multi-sensor data fusion method is introduced to estimate the vehicle speed in order to compute r^*. The inputs to the fuzzy logic controller are the yaw rate error $e = r - r^*$ and its derivative $\dot{e}$. The output of this controller is added to or subtracted from a uniform throttle command applied to each motor, by which means a corrective yaw moment is generated to regulate the vehicle yaw motion. Besides, a fuzzy logic controller for each wheel is used to limit the motor torque so that the wheel slip ratio remains in the safe region. Each slip controller receives the wheel slip ratio and wheel angular acceleration as the inputs, and generates the amount of torque that should be reduced from the total torque output of each motor if severe wheel slip occurs.

In the work of Motoyama et al. [49], a control method is proposed for traction force distribution between the left and right driving wheels. An ordinary Proportional-Derivative (PD) controller is employed to control the vehicle yaw rate, aiming to achieve neutral steer characteristic. This PD control law is written as:

$$\alpha = \alpha' + K_1(r - r^*) + K_2(\dot{r} - \dot{r}^*), \tag{2.13}$$

where r and r^* are the actual yaw rate and desired yaw rate (expressed by equation (2.5) with $K = 0$), respectively, K_1 and K_2 are the control parameters of the PD controller, α denotes the traction force distribution ratio between the left and right wheels, and α' represents the distribution ratio at the last sampling time.

Zhou and Liu [50] proposed a vehicle yaw stability control system using equation (2.5) as the desired (reference) yaw rate response. This cascade yaw stability control system consists of two interconnected parts. In the first part, a Sliding Mode Observer (SMO) is employed to estimate the longitudinal and lateral tire forces which are used to update the time-varying parameters in the vehicle and wheel models. In the second part, the control input is computed in a backstepping control framework and through sliding mode control in each step.

Nam et al. [51] developed an adaptive sliding mode control design for robust yaw stabilization of an electric vehicle with two rear in-wheel motors. A sliding mode controller is adopted in this design to make the vehicle track the desired yaw rate r^*, which is defined as:

$$r^* = \frac{r'}{1 + \tau p}, \tag{2.14}$$

where r' is the same reference yaw rate as equation (2.5), τ denotes the time constant and p represents the Laplace transform variable. This low-pass filter, $\dfrac{1}{1 + \tau p}$, is used to filter out the noise in the reference yaw rate signal. Besides, a parameter adaptation law is employed to estimate the changing vehicle parameters and is incorporated into the sliding mode control framework, which compensates the parameter uncertainties and disturbances that vary with the driving condition. In the work of Yamamoto [52], a desired yaw rate in the same form as equation (2.14) is employed. To track this reference value, a control law is designed as follows:

$$\Delta F_x = k(r^* - r), \tag{2.15}$$

where ΔF_x denotes the longitudinal tire force difference between the left and right driving wheels, k represents the control parameter, and r^* and r are the desired and actual yaw rates, respectively.

Chen et al. [15] designed a sliding mode-based DYC solution for in-wheel motor electric vehicles. This method takes into account the driver's behavior, and applies a modified version of equation (2.5) as the reference yaw rate. In the modified equation, instead of the measured front wheel steer angle δ, an optimal steer angle δ_{SW}^* is utilized to reflect the driver's steering intention based on a single point preview driver model [53]. Besides, an upper bound, $\mu g/v_x$, is applied to the desired yaw rate, where μ and g are the friction coefficient and gravitational acceleration, respectively. This is because the vehicle lateral acceleration a_y is limited by the friction coefficient [18], i.e. $|a_y| \leqslant \mu g$, and in steady state $a_y = v_x r$. A sliding mode controller is employed to drive the actual yaw rate towards the reference value, using a simple sliding surface defined as follows:

$$s = r - r^*. \tag{2.16}$$

Goodarzi et al. [54] devised two related DYC solutions based on Linear Quadratic Regulator (LQR) for motorized wheel electric vehicles. These schemes aim to enhance the vehicle handling by tracking the reference yaw rate response described by equation (2.5). The cost function of the proposed LQRs is defined as:

$$J = \frac{1}{2} \int_0^\infty \left(w M_z^2 + (r^* - r)^2 \right) \mathrm{d}t, \tag{2.17}$$

where M_z represents the generated corrective yaw moment (control input), r^* and r are the desired yaw rate (equation (2.5)) and actual yaw rate, respectively, and factor w denotes the relative importance of the yaw rate error and the energy expenditure due to control action. Note that the control performance is greatly influenced by the choice of the weighting factor w. When w reaches zero, the best yaw rate convergence is attained with the cost of infinite control input M_z. In practice, the maximum achievable yaw moment is limited by the road condition and maximum motor torque, which in turn restricts the permissible range of w.

A similar DYC approach that also employs the optimal control technique was proposed by Hancock et al. [10]. Instead of using the independent motor configuration, the proposed DYC scheme was realized by means of an actively controlled mechanical differential, particularly, an overdriven active rear differential, as schematically shown in Figure 2.8. This active differential employs two clutches to control the magnitude and direction of the torque transfer between the left and right wheels. When a torque transfer to the left wheel is required, the left hand clutch is engaged, and if a torque transfer to the right wheel is needed, the right hand clutch is engaged. An LQR is employed by this scheme to control the yaw moment generated by this torque transfer.
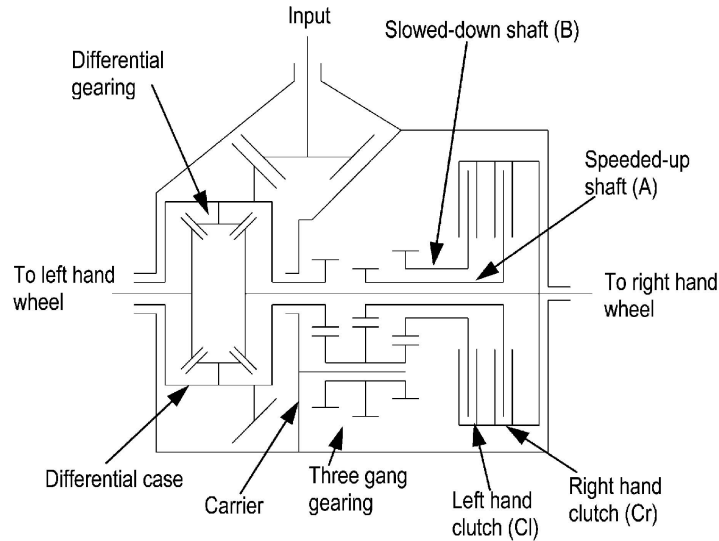
FIGURE 2.8: Schematic of DYC proposed by Hancock et al. [10].

The neutral steer yaw rate response (derived from equation (2.5) by setting $K = 0$) is used to form the error in the cost function of the LQR.

lkushima and Sawase [55] developed another DYC system based on an actively controlled mechanical differential. This system consists of a conventional differential, a Continuously Variable Transmission (CVT) and a torque transfer shaft, as shown in Figure 2.9. The CVT element A is directly connected to the right wheel axle, while the element B is connected to the left wheel axle through the shaft and gearing system. When a corrective yaw moment is not required, the same compressive forces are applied to the CVT elements A and B, leading to an equal torque distribution between the left and right wheels. If a clockwise yaw moment is needed, the compressive force on the element A is increased and torque is then transferred from the right wheel axle to the left wheel axle. On the contrary, when a counter-clockwise yaw moment is required the compressive force on the element B is increased, then torque is transferred from the left wheel axle to the right wheel axle. The amount of transferred torque is determined by the required corrective yaw moment that is controlled using a PI controller. This controller receives the actual yaw rate and reference yaw rate (calculated from equation (2.5)), and determines the amount of yaw moment to be generated based on the yaw rate error. The advantage of this active differential over the one presented in [10] lies in the reduction in energy loss, since it utilizes a CVT instead of clutches which rely on friction to operate.

To compute the stability factor K (equation (2.6)) in the desired (reference) yaw rate response, the knowledge of the cornering stiffnesses $C_{\alpha f}$ and $C_{\alpha r}$ is necessary. However, it is difficult to obtain accurate values of $C_{\alpha f}$ and $C_{\alpha r}$ in real time as they constantly change
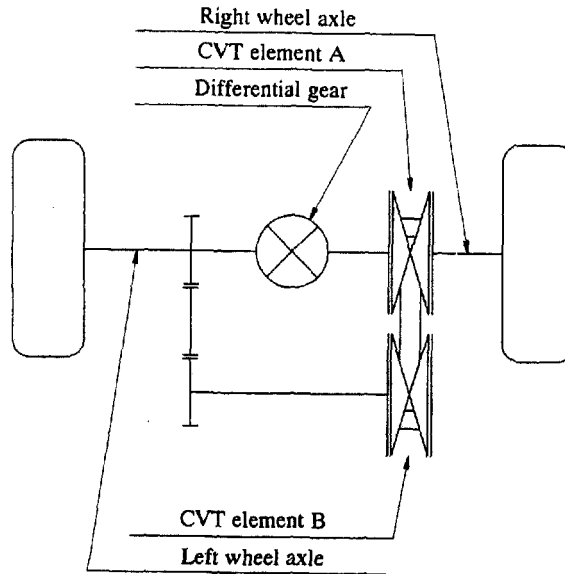
FIGURE 2.9: Schematic of DYC proposed by lkushima and Sawase [55].

with the driving condition. To avoid this difficulty, Tahami et al. [56] proposed a feed-forward neural network to generate a reference yaw rate response which approximates equation (2.5). The proposed reference response r^* is expressed as follows:

$$r^* = \frac{v_x}{l}\delta + r_{\text{correction}}(\delta, v_x),\qquad(2.18)$$

where v_x, l and δ denote the vehicle speed, wheel base and front wheel steer angle, respectively. The first term in equation (2.18) represents the yaw rate response that leads to neutral steer ($K = 0$), and the second term is the correction term produced by a feed-forward neural network which is trained using sinusoidal steering input and varying vehicle speed. To enhance the vehicle stability, similar to [48], a fuzzy logic controller is used to drive the actual yaw rate towards the reference value, and another four fuzzy logic controllers are employed to maintain the slip ratio of each wheel within the stable region.

2.3.3   Remarks

Numerous typical yaw rate-based DYC methods have been reviewed in this section. In these solutions, various control techniques are employed to tackle the problem of tracking the desired (reference) yaw rate response, aiming at enhancing the vehicle handling and stability. However, apart from the yaw rate, the vehicle side-slip is also an essential vehicle state that requires to be controlled. The yaw rate-based systems do not take into account the effect of the vehicle side-slip, thus their control performances may not be optimum. In the following, the DYC methods that control the vehicle side-slip only will

be first reviewed, followed by the introduction to more comprehensive and sophisticated DYC solutions which regulate both the yaw rate and vehicle side-slip simultaneously.

2.4 VEHICLE SIDE-SLIP-BASED DYC

2.4.1 Background

As introduced in Chapter 1, in addition to the yaw rate r, the vehicle side-slip β is also an essential vehicle state that needs to be controlled. Ideally, the vehicle side-slip requires to be minimized for two reasons. Firstly, according to the findings reported in [21], when the vehicle side-slip increases to large values, the tire cornering stiffnesses decrease and the yaw moment generated by the lateral tire forces descends. Since the slopes of the yaw moment curves (see Fig. 5 in [21]) are close to zero, the generated yaw moment can hardly be increased by changing the steer angle. This means that no sufficient yaw moment can be generated at large vehicle side-slip, which may lead the vehicle to lose its stability. Secondly, a small vehicle side-slip indicates a consistency of the vehicle heading direction with the velocity vector $\boldsymbol{v}$ (shown in Figure 1.4). This consistency provides the driver with superior sense of control during cornering [22], as the driver intuitively assumes that the vehicle heading direction is the direction where the vehicle is going. Due to these reasons, zero desired vehicle side-slip, $\beta^* = 0$, is often employed in the vehicle dynamics and control literature.

Note that $\beta^* = 0$ is a strict condition to be satisfied. Indeed, many existing DYC solutions aim to limit β in a stable region or control β to follow some prescribed dynamics, in order to prevent it from diverging and maintain the vehicle stability. For example, the steady-state vehicle side-slip response (or its variation/modification) derived from the two DoF planar vehicle model [20] is often employed as the desired (reference) vehicle side-slip. This value can be expressed in the following general form [35]:

$$\beta = \frac{\left(l_{\mathrm{r}} - \dfrac{m l_{\mathrm{f}} v_x^2}{l C_{\alpha \mathrm{r}}}\right)\delta}{l(1 + K v_x^2)}, \tag{2.19}$$

where the symbols used are consistent with those in equation (2.5).

In the following section, the typical vehicle side-slip-based DYC solutions are reviewed. These methods either constrain β in a stable region, or track a desired (reference) response, i.e. zero vehicle side-slip or equation (2.19) (or its variation/modification). Note

that apart from the vehicle side-slip-based DYC systems for electric vehicles with independent motors, other typical types of vehicle side-slip-based DYC methods (e.g. differential braking systems) are also reviewed, as they share similar design principles and lay the foundation for new DYC designs.

2.4.2 Typical vehicle side-slip-based DYC methods

Abe et al. [57] proposed a DYC control method employing zero desired vehicle side-slip, $\beta^* = 0$. In this design, the transfer function of the vehicle side-slip response with the DYC system on-board is expressed as follows:

$$\beta(p) = \frac{B_f(p)\delta(p) + B_M M(p)}{G(p)}, \tag{2.20}$$

where p denotes the Laplace transform variable, $\beta(p)$, $\delta(p)$ and $M(p)$ are the Laplace transformations of the vehicle side-slip, steering wheel angle and corrective yaw moment generated by the DYC, respectively, and $B_f(p)$, B_M and $G(p)$ are coefficients expressed by the vehicle parameters (see [57]). Setting this vehicle side-slip response to zero leads to the following control law:

$$\frac{M}{\delta}(p) = -\frac{B_f}{B_M}(p). \tag{2.21}$$

Comparative simulation results indicate that the proposed DYC is less effective than 4-Wheel-Steering (4WS) in achieving zero vehicle side-slip, but it provides a more responsive yaw rate response than 4WS.

To analyze the vehicle stability graphically, a phase-plane method considering two vehicle states (vehicle side-slip β and its derivative $\dot{\beta}$) is proposed by Inagaki et al. [58]. In view of the fact that the vehicle stability is intrinsically related to the vehicle lateral motion, this method plots the state trajectories of the vehicle system on the $\beta - \dot{\beta}$ phase-plane. The stable and unstable regions, as well as how the trajectories evolve with time, are clearly portrayed on the phase-plane, which provides insights into how vehicle stability control systems should be designed to keep the vehicle stable. The state trajectories are kept in the stable region if the following condition is satisfied:

$$|C_1\beta + C_2\dot{\beta}| < 1, \tag{2.22}$$

where C_1 and C_2 are two constants.

Based on this method, different DYC systems (e.g. [58–63]) have been devised to achieve the task of maintaining the vehicle state trajectories within the stable region. Yasui et al. [61] designed a vehicle stability enhancement system to achieve this task by controlling

the wheel slip ratio of the front-outer wheel. The target wheel slip ratio is defined as follows:

$$\lambda^* = K_1\beta + K_2\dot{\beta}, \tag{2.23}$$

where K_1 and K_2 are two design parameters. The brake pressure for the front-outer wheel is regulated to track this desired wheel slip ratio so that the state trajectories remain in the stable region. In the work of Tian et al. [62], when the point $(\beta, \dot{\beta})$ on the phase-plane is outside the stable region, a DYC system is activated to drive it back to the stable region. The nearest distance between the point $(\beta, \dot{\beta})$ and the boundary of the stable region is defined as d. A simple PI controller is employed by the DYC to drive d to zero, with the distance d being the input and the corrective yaw moment M being the output. When the point $(\beta, \dot{\beta})$ is inside the stable region, an AFS system based on sliding mode control is adopted to track the response of a reference vehicle model. An analogous DYC approach which also adopts the distance d to determine the control effort is proposed by He et al. [63].

Uematsu and Gerdes [17] proposed a sliding mode control scheme that employs the vehicle side-slip and its derivative in the sliding surface design. This sliding surface can be written as:

$$s = \dot{\beta} + \alpha\beta = 0, \tag{2.24}$$

where α is a positive design parameter. To drive the state trajectory towards the sliding surface, the following sliding condition should be satisfied:

$$\dot{s} = -ks, \tag{2.25}$$

where k represents the convergence rate at which the state trajectory approaches the sliding surface. It should be pointed out that this control design faces an implementation challenge as the control input requires the derivatives of the lateral tire forces due to the involvement of $\dot{\beta}$ in the sliding surface.

Furukawa and Abe [64, 65] devised a DYC strategy to regulate the vehicle side-slip in conjunction with 4WS by means of sliding mode control. In this design, the vehicle states are driven towards the sliding surface defined as follows:

$$s = \dot{\beta} + c(\beta + a\dot{\beta}) = 0, \tag{2.26}$$

where a and c are two design parameters. To guarantee that the above sliding surface is reached, the following sliding condition is mandated:

$$\dot{s} = -ks, \tag{2.27}$$

where k denotes the convergence rate. The information of β required to generate the control command is estimated by integrating the lateral tire forces computed from an on-board tire model. When the control strategy is applied to a 2-Wheel-Steering (2WS) vehicle, the sliding surface is modified as follows:

$$s = \dot{\beta} + c(\beta - \beta^*) = 0, \tag{2.28}$$

where β^* is the steady-state vehicle side-slip response expressed by equation (2.19).

In the works of Abe et al. [66–68], a model following control by means of sliding mode control is proposed to compensate for the loss of stability due to the nonlinear tire characteristics. The model response to be followed is derived from the common two DoF planar vehicle model (bicycle model), and it can be expressed in the form of a transfer function as follows:

$$\frac{\beta}{\delta}(p) = G\frac{1 + Tp}{1 + \dfrac{Q}{P}p + \dfrac{1}{P}p^2}, \tag{2.29}$$

where p denotes the Laplace transform variable, G is the vehicle side-slip gain constant (the value of β in response to δ in steady state), and T, Q and P are constants expressed by the vehicle parameters (see [66]). A sliding mode controller is adopted for the model following control. The sliding surface is achieved by rewriting equation (2.29) in the following form:

$$s = \ddot{\beta} + Q\dot{\beta} + P\beta - PGT\dot{\delta} - PG\delta = 0. \tag{2.30}$$

The sliding condition to be satisfied is written as:

$$\dot{s} = -ks, \tag{2.31}$$

where k represents the convergence rate. By this means, the vehicle side-slip response is controlled to follow the model response expressed by equation (2.29), which in turn enhances the vehicle stability. Abe et al. [66] concluded that: the vehicle side-slip-based DYC is more effective than the yaw rate-based DYC and 4WS in stabilizing the vehicle.

2.4.3 Remarks

The implementation of the vehicle side-slip-based DYC schemes requires the real-time information of the vehicle side-slip angle β, therefore a properly designed state observer is necessary to estimate this state as no standard sensors are available for low-cost measurements. The estimation of β is outside the scope of this study, but it has become

a research focus and numerous estimation methods have been proposed in the literature [69–74].

So far, the typical control methods that regulate the yaw rate only and the vehicle side-slip only have been reviewed in two seperate sections. Even though the yaw rate and vehicle side-slip are intrinsically related by the vehicle dynamics (see the vehicle equations of motion in Chapter 3), controlling only one of them may not lead to optimum dynamic performance in terms of the vehicle handling and stability. Indeed, integrated control of both vehicle states has been shown to be generally more effective. In the following, the more comprehensive and sophisticated DYC solutions that regulate both the yaw rate and vehicle side-slip simultaneously are reviewed.

2.5 SIMULTANEOUS CONTROL OF YAW RATE AND VEHICLE SIDE-SLIP

2.5.1 Background

As introduced in Chapter 1, the yaw rate and vehicle side-slip are known to be the two fundamental states that govern the vehicle handling and stability. It has been pointed out in the literature that controlling one state only may bring about problems in some certain circumstances. For instance, on low friction roads, controlling the yaw rate only may be insufficient to prevent the vehicle side-slip from diverging, and in turn the vehicle may lose its stability and spin [17–19]. On the other hand, controlling the vehicle side-slip only guarantees the vehicle stability but may not produce desirable yaw rate response (i.e. favorable steer characteristic) [24]. As a result, in order to eliminate the downsides resulting from controlling one state only and combine the benefits of controlling the yaw rate and vehicle side-slip individually, numerous recent DYC works adopt both states simultaneously as the control variables. These solutions have presented superior control performance to the systems controlling one state only [17, 23–26].

2.5.2 Typical control methods

Sliding mode control provides robustness against system uncertainties and external disturbances [75–77]. Thanks to this property, sliding mode control is ideal for controlling nonlinear plants such as the vehicle systems, and it has been commonly adopted in the recent DYC system designs. One critical step in designing a sliding mode controller is the choice of switching function (thus sliding surface). The most common switching

function design in the recent DYC systems employs a linear combination of the yaw rate and vehicle side-slip errors, which takes the following general form [17, 23, 24, 78–81]:

$$s = r - r^* + \xi(\beta - \beta^*), \tag{2.32}$$

where r^* and β^* are the desired (reference) yaw rate and vehicle side-slip, respectively, and ξ is a positive design parameter. Both the yaw rate and vehicle side-slip errors are adopted in this switching function, hence both vehicle states, the yaw rate and vehicle side-slip, are regulated simultaneously by the sliding mode controller.

Yi et al. [23] devised a differential braking strategy for vehicle stability control. The corrective yaw moment generated from differential braking is derived by means of sliding mode control using a three DoF planar vehicle model. The proposed sliding mode controller employs equation (2.32) as the switching function. Zero desired vehicle side-slip, $\beta^* = 0$, is employed in this scheme. To allow for the tire-road friction limit, the desired (reference) yaw rate r^* is defined as follows:

$$r^* = \begin{cases} r_{\mathrm{t}} & \text{if } |r_{\mathrm{t}}| < \dfrac{\mu g}{v_x}, \\ \dfrac{\mu g}{v_x}\,\mathrm{sgn}(r_{\mathrm{t}}) & \text{if } |r_{\mathrm{t}}| \geqslant \dfrac{\mu g}{v_x}, \end{cases} \tag{2.33}$$

where μ represents the friction coefficient, g denotes the gravitational acceleration and r_{t} is the same yaw rate response as described by equation (2.5).

The switching function, equation (2.32), was utilized by Li and Cui [78] to devise a sliding mode controller for an electric vehicle with four independent driving wheels. The desired yaw rate r^* is the same as [23], while the desired vehicle side-slip is defined as follows:

$$\beta^* = (\frac{l_{\mathrm{r}}}{v_x} - \frac{l_{\mathrm{f}} m v_x}{l})r^*. \tag{2.34}$$

This desired vehicle side-slip value is indeed the same as equation (2.19). In this design, the front and rear motor torques are maintained at a fixed ratio, thereby eliminating the task of motor torque distribution between the four driving wheels. However, this simplified scheme does not make proper use of the adhesion condition of individual wheels, thus it may not achieve optimum control performance. To tackle this problem, some works have been proposed in the literature to dynamically and effectively distribute the longitudinal tire forces to obtain a certain corrective yaw moment [82, 83].

Tchamna and Youn [24] proposed a braking-based sliding mode DYC design considering the vehicle longitudinal dynamics, with equation (2.32) chosen as the switching function. The feature of this design lies in that it does not adopt the simplifying assumptions such as constant vehicle longitudinal velocity and small vehicle side-slip angle. These

assumptions are commonly used in the control design process as many works are based on the two DoF planar vehicle model (bicycle model) which is valid only under these assumptions. Note that the vehicle side-slip is mathematically defined as $\beta = \arctan \frac{v_y}{v_x}$, where v_x and v_y denote the vehicle longitudinal and lateral velocities, respectively. The conventional control methods assume small vehicle side-slip angle and constant vehicle longitudinal velocity, which leads to the following approximations:

$$\beta \approx \frac{v_y}{v_x} \tag{2.35}$$

$$\dot{\beta} \approx \frac{\dot{v}_y}{v_x}. \tag{2.36}$$

However, the proposed method does not adopt these assumptions and it employs the following derivative that is directly derived from the vehicle side-slip definition:

$$\dot{\beta} = (1 + \tan^2 \beta)^{-1}(\frac{\dot{v}_y}{v_x} - \frac{\dot{v}_x}{v_x} \tan \beta). \tag{2.37}$$

This expression is employed in the sliding mode control design to produce a more effective control input. The simulation results presented in [24] show that the proposed scheme produces superior control performance to the conventional solutions that use these assumptions.

Yim and Yi [79] developed an Active Roll Control System (ARCS) with Integrated Chassis Control (ICC) for a hybrid 4WD vehicle. The hybrid power-train, as shown in Figure 2.10, features an ICE for the front wheels and two independent motors for the rear wheels. The ARCS based on sliding mode control is employed to minimize the roll angle and roll rate using an active anti-roll bar. However, simulation results indicate that using the ARCS alone leads the vehicle to oversteer and impairs the vehicle stability even though the roll angle can be reduced. To solve this problem, an ICC with a two-level structure is adopted to work in tandem with the ARCS to restore the vehicle stability and maneuverability. The upper level of the ICC generates a corrective yaw moment to regulate the yaw rate and vehicle side-slip, by means of sliding mode control with equation (2.32) being the switching function. The lower level distributes this corrective yaw moment to the ESC, AFS and 4WD systems available on the hybrid vehicle based on a Weighted Least Square (WLS) approach. It is validated through simulations that the proposed ARCS with ICC can effectively reduce the roll angle and roll rate while maintaining the vehicle stability.

Mashadi and Majidi [80] designed an integrated AFS/DYC sliding mode controller for a Hybrid Electric Vehicle (HEV). This HEV possesses an ICE for the front wheels and two electric motors for the rear wheels, similar to the vehicle configuration in [79]. These two motors produce equal torques in opposite directions, which generates a corrective
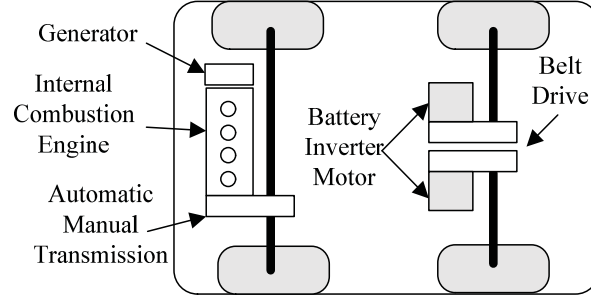
FIGURE 2.10: Schematic of the hybrid power-train [79].

yaw moment and does not change the vehicle longitudinal dynamics. The integrated AFS/DYC sliding mode controller employs a modified version of equation (2.32) as the switching function, which is expressed as follows:

$$s = r - r^* + w \times (\beta^* - \beta) \times u(|\beta| - |\beta^*|), \tag{2.38}$$

where w is a design parameter, and $u(|\beta| - |\beta^*|)$ is a function defined as:

$$u(|\beta| - |\beta^*|) = \begin{cases} 1 & \text{if } |\beta| > |\beta^*|, \\ 0 & \text{if } |\beta| \leqslant |\beta^*|. \end{cases} \tag{2.39}$$

Using this switching function, the proposed sliding mode controller aims to track the desired yaw rate while maintaining the absolute value of the actual vehicle side-slip equal to or smaller than the desired one. The output of this controller is the total corrective yaw moment generated by the AFS and DYC systems, and it is distributed to the AFS and DYC systems according to the driving condition.

Apart from the above single sliding surface designs, several multi-surface sliding mode DYC solutions have also been proposed in the literature [17, 84–86]. Similar to the single sliding surface case, both the yaw rate and vehicle side-slip are regulated simultaneously by these multi-surface sliding mode controllers. In the multi-surface designs, each vehicle state is individually involved in one of the sliding surfaces, as opposed to being linearly combined in a single surface. One common feature of these multi-surface works is their hierarchical sliding surface configuration. Specifically, the primary sliding surface is defined as the vehicle side-slip error, and the secondary sliding surface is defined as the yaw rate error with a certain reference yaw rate value to match the vehicle side-slip objective. For example, in the work of Uematsu and Gerdes [17], the primary and secondary sliding surfaces are defined as:

$$s_1 = \beta \tag{2.40}$$

$$s_2 = r - r^*. \tag{2.41}$$

In order to achieve the primary control objective – zero vehicle side-slip, considering the two DoF planar vehicle model, the following desired yaw rate must be tracked:

$$r^* = \frac{\sum F_y}{mv_x} - \dot{\beta}, \tag{2.42}$$

where $\sum F_y$ denotes the total external forces acted on the vehicle in the lateral direction. The limitation of this sliding surface configuration is that the desired yaw rate in the secondary surface has to be a certain function, and cannot be assigned an arbitrary reference value as in the single-surface case. In other words, the yaw rate and vehicle side-slip cannot actually be independently controlled. Comparative simulations presented in [17] show that both the single-surface and multi-surface schemes present superior control performances to the systems employing only one vehicle state as the control variable. In particular, the multi-surface system provides better robustness but slower yaw rate response than the single-surface scheme.

Even though sliding mode control has become the most popular control technique in the recent DYC solutions for regulating the yaw rate and vehicle side-slip simultaneously, other typical types of control techniques are also employed in the literature to tackle the same problem. Chumsamutr and Fujioka [87] proposed a DYC scheme based on optimal control theory to control the driving and braking torques for an electric vehicle. The two DoF planar vehicle model used in the proposed design can be expressed with the following state-space representation:

$$\dot{\boldsymbol{x}} = \boldsymbol{A}\boldsymbol{x} + \boldsymbol{B}M + \boldsymbol{E}\delta, \tag{2.43}$$

where $\boldsymbol{x} = [\beta \ \ r]^{\mathrm{T}}$ denotes the state vector, M represents the corrective yaw moment, δ stands for the front wheel steer angle, and $\boldsymbol{A}$, $\boldsymbol{B}$ and $\boldsymbol{E}$ are the coefficient matrices expressed by the vehicle parameters (see [87]). The steady-state responses of β and r derived from the two DoF model with $M = 0$ are taken as the desired responses, denoted by $\boldsymbol{x}_{\mathrm{des}}$. Then, the vehicle dynamics in terms of the error vector $\boldsymbol{e} = \boldsymbol{x} - \boldsymbol{x}_{\mathrm{des}}$ is described as:

$$\dot{\boldsymbol{e}} = \boldsymbol{A}\boldsymbol{e} + \boldsymbol{B}M. \tag{2.44}$$

The corrective yaw moment M is determined in such a way that the following cost function is minimized:

$$J = \int_0^\infty \left(\boldsymbol{e}^{\mathrm{T}}\boldsymbol{Q}\boldsymbol{e} + \varepsilon M^2\right)\mathrm{d}t, \tag{2.45}$$

where ε is a design parameter and $\boldsymbol{Q}$ is a design matrix. The simulation results indicate that in the linear region of the tire characteristics, the proposed controller provides the vehicle with a faster cornering response, while in the nonlinear region, the controller ensures the vehicle stability by driving the vehicle side-slip close to zero. Several similar

control approaches have also been proposed [1, 88–92] to regulate the yaw rate and vehicle side-slip simultaneously by means of optimal control theory.

Fuzzy logic control techniques are also employed by DYC systems to regulate both the yaw rate and vehicle side-slip, as fuzzy logic control provides the benefit of not requiring a mathematical model of the plant while still being highly robust [25]. Zhao et al. [93] proposed a DYC solution based on fuzzy logic control for a four-in-wheel-motor drive electric vehicle. In this design, equation (2.5) is used as the desired yaw rate response and zero vehicle side-slip is adopted as the desired vehicle side-slip response. The inputs to this fuzzy logic controller are the yaw rate error and vehicle side-slip error, and the output from this controller is the corrective yaw moment. This control scheme is proven to be effective in controlling the yaw rate and vehicle side-slip by both simulations and experiments. A similar fuzzy logic control approach to the above solution is available in the work of Kim et al. [94].

Buckholtz [26] devised a fuzzy logic yaw rate control scheme with vehicle side-slip limitation. This fuzzy logic controller tracks the desired yaw rate by assigning an appropriate wheel slip ratio to each wheel. The yaw rate tracking is activated only when the error quantity, $e = r^* - r + k(\dot{r}^* - \dot{r})$ ($k > 0$ is a design parameter), exceeds a user-defined threshold. Using this indirect approach, the vehicle side-slip magnitude is restricted and no information of the vehicle side-slip is required.

In the work of Sun et al. [95], a fuzzy logic control algorithm is developed to integrate the DYC and AFS. This fuzzy logic controller produces control commands for the DYC and AFS to track the desired yaw rate and vehicle side-slip simultaneously. The two inputs to the fuzzy logic controller are the yaw rate and vehicle side-slip errors, and the outputs from this controller are the corrective yaw moment generated by the DYC and the corrective front wheel steer angle produced by the AFS.

2.5.3 Remarks

Aiming at eliminating the downsides resulting from controlling one state only and combining the benefits of controlling the yaw rate and vehicle side-slip individually, numerous DYC solutions have been proposed in the recent literature to regulate both states simultaneously. In this section, typical DYC systems of such type have been reviewed. For each DYC control scheme, the theories and principles behind the control technique are clearly explained. Note that sliding mode control has become the most prevalent control technique in this field due to its robustness against disturbances and uncertainties for controlling nonlinear systems. Different variations of sliding mode DYC schemes, for example various sliding surface designs, are currently being extensively discussed in the

literature. The implementations of these sliding mode controllers require real-time information of the yaw rate and vehicle side-slip, which necessitates the design of appropriate measuring and/or estimation methods. Besides, more experimental results are needed to comprehensively and thoroughly validate the effectiveness of these sliding mode DYC approaches.

Chapter 3

Full Vehicle Model

To validate the DYC designs proposed in the subsequent chapters through comprehensive computer simulations, an accurate full vehicle model that reflects closely the vehicle dynamics in reality is required to establish the simulation model in the MATLAB/Simulink environment. The vehicle equations of motion, as part of the full vehicle model, are the mathematical representation of the plant (i.e. the vehicle) and they express the dynamics of the vehicle longitudinal motion, lateral motion, roll motion and yaw motion. These equations are required in the subsequent chapters for control system design. For these reasons, a full vehicle model, including the vehicle equivalent mechanical model, vehicle equations of motion, wheel equation of motion and *Magic Formula* tire model, is introduced in this chapter.

3.1   VEHICLE EQUIVALENT MECHANICAL MODEL

In order to obtain the vehicle equations of motion, we must first establish a vehicle equivalent mechanical model. As a vehicle consists of two major parts: sprung mass and unsprung mass, we regard these two parts as two rigid bodies in the mechanical model. Figure 3.1 shows the vehicle equivalent mechanical model and the attached coordinate systems. This mechanical model consists of two rigid bodies, with the top body denoting the vehicle sprung mass and the bottom one representing the unsprung mass. The coordinate system x-y-z is attached to the unsprung rigid body. The origin of the coordinate system, P, is right under the mass center of the entire vehicle when the vehicle is stationary. The x axis coincides with the vehicle longitudinal direction, the y axis goes laterally to the left from the driver's view, and the z axis directs vertically upwards. The other coordinate system x'-y'-z' is fixed to the sprung rigid body with the same origin P. When the vehicle is stationary, the two coordinate systems coincide.
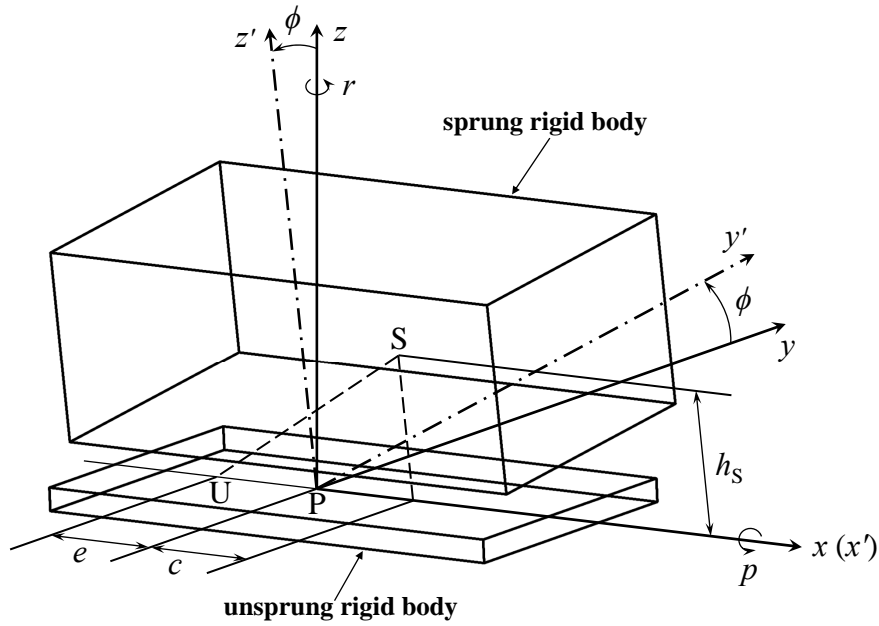
FIGURE 3.1: Vehicle equivalent mechanical model and vehicle coordinate systems [97].

The two rigid bodies are assumed to produce the same yaw motion about the z axis, thus the x axis and the x' axis always coincide. Also, the sprung rigid body is assumed to roll about the x' axis, while the roll motion of the unsprung rigid body is neglected. The vertical motion and pitch motion of the two masses are neglected, because these motions are mainly related to vehicle ride [96] while the focus of this study is on vehicle stability and handling.

The points S and U represent the mass centers of the sprung mass and the unsprung mass, respectively. The point U is located on the x axis. h_S denotes the distance between S and the x' axis, c represents the distance between S and P on the x' axis, and e is the distance between U and P. r and p are the yaw rate and the roll rate respectively, and ϕ is the sprung mass roll angle. The positive directions of the angular displacement and the angular velocities are shown in Figure 3.1. The more detailed explanation on this vehicle mechanical model is available in [97].

3.2 VEHICLE EQUATIONS OF MOTION

The vehicle equations of motion are of great significance in this study. They mathematically represent the plant to be controlled in the DYC system and they are employed in the following chapters for control system design. Besides, they are adopted in the simulation model to compute the vehicle states of the simulated vehicle. In this section, the vehicle equations of motion are derived based on the vehicle equivalent mechanical
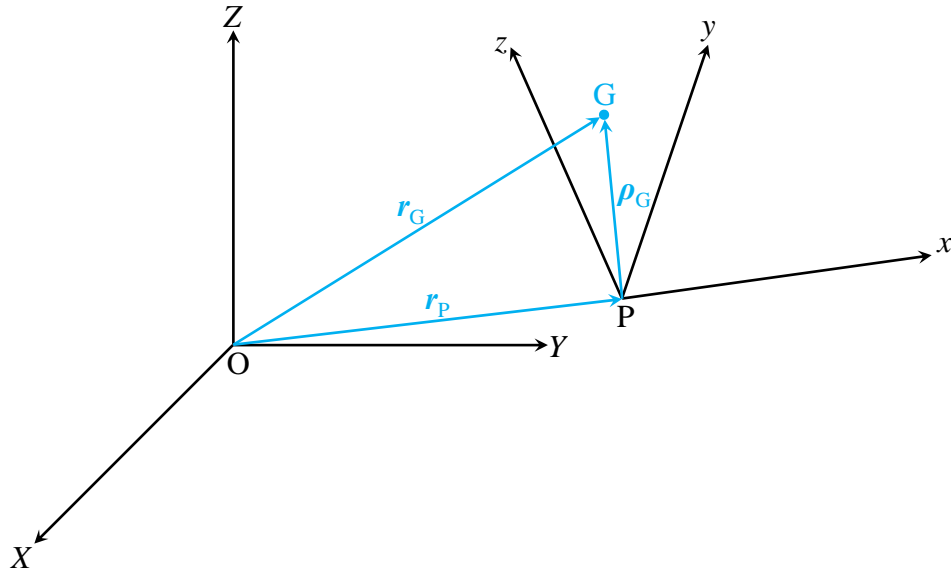
FIGURE 3.2: Description of rigid body general motion.

model established in section 3.1. The detailed expression of this derivation is available in [97].

3.2.1 Translational motion

In the translational motion analysis, in order for the Newton's second law to be valid, an inertial (global) coordinate system X-Y-Z with origin O is introduced. This coordinate system is stationary in the absolute space. Assume that another coordinate system x-y-z with origin P is attached to a rigid body which is moving in the absolute space. These two coordinate systems are shown in Figure 3.2.

The point G denotes a fixed point in the rigid body. The vector $\boldsymbol{\rho}_\mathrm{G}$ is the position vector of the point G with respect to the coordinate system x-y-z. The vectors $\boldsymbol{r}_\mathrm{P}$ and $\boldsymbol{r}_\mathrm{G}$ are the position vectors of the points P and G with respect to the coordinate system X-Y-Z, respectively.

As can be seen in Figure 3.2, the three vectors are related by:

$$\boldsymbol{r}_\mathrm{G} = \boldsymbol{r}_\mathrm{P} + \boldsymbol{\rho}_\mathrm{G}. \tag{3.1}$$

Differentiation of equation (3.1) in the global coordinate system X-Y-Z provides:

$$\dot{\boldsymbol{r}}_\mathrm{G} = \dot{\boldsymbol{r}}_\mathrm{P} + \dot{\boldsymbol{\rho}}_\mathrm{G}. \tag{3.2}$$

Expressing the vector $\boldsymbol{\rho}_{\mathrm{G}}$ in the coordinate system x-y-z and applying the *Transport Theorem* in mechanics [98] lead to:

$$\dot{\boldsymbol{\rho}}_{\mathrm{G}} = \dot{\boldsymbol{\rho}}_{\mathrm{Grel}} + \boldsymbol{\omega} \times \boldsymbol{\rho}_{\mathrm{G}}, \tag{3.3}$$

where $\dot{\boldsymbol{\rho}}_{\mathrm{Grel}}$ represents the relative velocity of the point G with respect to the coordinate system x-y-z, and $\boldsymbol{\omega}$ denotes the angular velocity of the coordinate system x-y-z with respect to the coordinate system X-Y-Z. In this study $\dot{\boldsymbol{\rho}}_{\mathrm{Grel}} = \mathbf{0}$ since the point G is fixed in the coordinate system x-y-z. Note that $\dot{\boldsymbol{r}}_{\mathrm{P}}$, the velocity of the point P with respect to the coordinate system X-Y-Z, should be expressed in the coordinate system x-y-z in order for the addition in equation (3.2) to be valid. Substituting equation (3.3) in equation (3.2) gives:

$$\dot{\boldsymbol{r}}_{\mathrm{G}} = \dot{\boldsymbol{r}}_{\mathrm{P}} + \boldsymbol{\omega} \times \boldsymbol{\rho}_{\mathrm{G}}. \tag{3.4}$$

Now equation (3.4) is applied to the sprung rigid body and unsprung rigid body. The position vectors of the points S and U with respect to the coordinate system X-Y-Z are denoted by $\boldsymbol{r}_{\mathrm{S}}$ and $\boldsymbol{r}_{\mathrm{U}}$, respectively, the position vectors of the points S and U with respect to the coordinate systems x'-y'-z' and x-y-z are denoted by $\boldsymbol{\rho}_{\mathrm{S}}$ and $\boldsymbol{\rho}_{\mathrm{U}}$, respectively, and the angular velocities of the coordinate systems x'-y'-z' and x-y-z with respect to the coordinate system X-Y-Z are denoted by $\boldsymbol{\omega}_{\mathrm{S}}$ and $\boldsymbol{\omega}_{\mathrm{U}}$, respectively. Then, the following relations are obtained:

$$\dot{\boldsymbol{r}}_{\mathrm{S}} = \dot{\boldsymbol{r}}_{\mathrm{P}} + \boldsymbol{\omega}_{\mathrm{S}} \times \boldsymbol{\rho}_{\mathrm{S}} \tag{3.5}$$

$$\dot{\boldsymbol{r}}_{\mathrm{U}} = \dot{\boldsymbol{r}}_{\mathrm{P}} + \boldsymbol{\omega}_{\mathrm{U}} \times \boldsymbol{\rho}_{\mathrm{U}}. \tag{3.6}$$

In equations (3.5) and (3.6), $\dot{\boldsymbol{r}}_{\mathrm{P}}$ is expressed in the coordinate systems x-y-z and x'-y'-z' using the unit vectors in these two coordinate systems, respectively. The unit vectors in the x, y and z directions are denoted by $\boldsymbol{i}$, $\boldsymbol{j}$ and $\boldsymbol{k}$, respectively, and the unit vectors in the x', y' and z' directions are denoted by $\boldsymbol{i}'$, $\boldsymbol{j}'$ and $\boldsymbol{k}'$, respectively. Then, $\dot{\boldsymbol{r}}_{\mathrm{P}}$ can be expressed as:

$$\dot{\boldsymbol{r}}_{\mathrm{P}} = v_x \boldsymbol{i} + v_y \boldsymbol{j} = v_x \boldsymbol{i}' + v_y(\boldsymbol{j}' \cos \phi - \boldsymbol{k}' \sin \phi), \tag{3.7}$$

where v_x and v_y denote the longitudinal and lateral velocities of the point P in the x and y directions (shown in Figure 1.4), respectively. The unit vector transformations used in equation (3.7) are elaborated in [98], and are not repeated in this thesis. Since the sprung mass roll angle ϕ is normally small (so $\cos \phi \approx 1$ and $\sin \phi \approx 0$) [97], equation (3.7) simplifies to:

$$\dot{\boldsymbol{r}}_{\mathrm{P}} = v_x \boldsymbol{i} + v_y \boldsymbol{j} = v_x \boldsymbol{i}' + v_y \boldsymbol{j}'. \tag{3.8}$$

It is seen from Figure 3.1 that the sprung rigid body possesses a roll angular velocity p about the x' axis, and a yaw angular velocity r about the z axis. In the following, p and r will be referred to as roll rate and yaw rate, respectively. The total angular velocity of the coordinate system x'-y'-z' (i.e. the sprung rigid body) with respect to the coordinate system X-Y-Z is:

$$\boldsymbol{\omega}_S = p\boldsymbol{i}' + r\boldsymbol{k} = p\boldsymbol{i}' + r(\boldsymbol{j}'\sin\phi + \boldsymbol{k}'\cos\phi). \tag{3.9}$$

For the same reason explained above, equation (3.9) reduces to:

$$\boldsymbol{\omega}_S = p\boldsymbol{i}' + r\boldsymbol{k} = p\boldsymbol{i}' + r\boldsymbol{k}'. \tag{3.10}$$

As the roll motion of the unsprung rigid body is neglected, the unsprung rigid body possesses only a yaw angular velocity r about the z axis. Thus, the total angular velocity of the coordinate system x-y-z (i.e. the unsprung rigid body) with respect to the coordinate system X-Y-Z is:

$$\boldsymbol{\omega}_U = r\boldsymbol{k}. \tag{3.11}$$

The position vectors $\boldsymbol{\rho}_S$ and $\boldsymbol{\rho}_U$ are expressed in the coordinate systems x'-y'-z' and x-y-z, respectively:

$$\boldsymbol{\rho}_S = c\boldsymbol{i}' + h_S\boldsymbol{k}' \tag{3.12}$$

$$\boldsymbol{\rho}_U = -e\boldsymbol{i}. \tag{3.13}$$

Substituting equations (3.8), (3.10) and (3.12) in equation (3.5), and equations (3.8), (3.11) and (3.13) in equation (3.6) lead to:

$$\dot{\boldsymbol{r}}_S = v_x\boldsymbol{i}' + (v_y - h_S p + cr)\boldsymbol{j}' \tag{3.14}$$

$$\dot{\boldsymbol{r}}_U = v_x\boldsymbol{i} + (v_y - er)\boldsymbol{j}. \tag{3.15}$$

Differentiating equations (3.14) and (3.15) in the global coordinate system X-Y-Z yields:

$$\ddot{\boldsymbol{r}}_S = \dot{v}_x\boldsymbol{i}' + v_x\dot{\boldsymbol{i}}' + (\dot{v}_y - h_S\dot{p} + c\dot{r})\boldsymbol{j}' + (v_y - h_S p + cr)\dot{\boldsymbol{j}}' \tag{3.16}$$

$$\ddot{\boldsymbol{r}}_U = \dot{v}_x\boldsymbol{i} + v_x\dot{\boldsymbol{i}} + (\dot{v}_y - e\dot{r})\boldsymbol{j} + (v_y - er)\dot{\boldsymbol{j}}. \tag{3.17}$$

It is known that [97, 98]:

$$\dot{\boldsymbol{i}}' = \boldsymbol{\omega}_{\mathrm{S}} \times \boldsymbol{i}' \tag{3.18}$$

$$\dot{\boldsymbol{j}}' = \boldsymbol{\omega}_{\mathrm{S}} \times \boldsymbol{j}' \tag{3.19}$$

$$\dot{\boldsymbol{k}}' = \boldsymbol{\omega}_{\mathrm{S}} \times \boldsymbol{k}' \tag{3.20}$$

$$\dot{\boldsymbol{i}} = \boldsymbol{\omega}_{\mathrm{U}} \times \boldsymbol{i} \tag{3.21}$$

$$\dot{\boldsymbol{j}} = \boldsymbol{\omega}_{\mathrm{U}} \times \boldsymbol{j} \tag{3.22}$$

$$\dot{\boldsymbol{k}} = \boldsymbol{\omega}_{\mathrm{U}} \times \boldsymbol{k}. \tag{3.23}$$

Substituting equations (3.10) and (3.11) in equations (3.18) to (3.23) provides:

$$\dot{\boldsymbol{i}}' = r\boldsymbol{j}' \tag{3.24}$$

$$\dot{\boldsymbol{j}}' = p\boldsymbol{k}' - r\boldsymbol{i}' \tag{3.25}$$

$$\dot{\boldsymbol{k}}' = -p\boldsymbol{j}' \tag{3.26}$$

$$\dot{\boldsymbol{i}} = r\boldsymbol{j} \tag{3.27}$$

$$\dot{\boldsymbol{j}} = -r\boldsymbol{i} \tag{3.28}$$

$$\dot{\boldsymbol{k}} = \boldsymbol{0}. \tag{3.29}$$

Then, substitution of equations (3.24), (3.25), (3.27) and (3.28) in equations (3.16) and (3.17) gives:

$$\ddot{\boldsymbol{r}}_{\mathrm{S}} = (\dot{v}_x - v_y r + h_{\mathrm{S}} pr - cr^2)\boldsymbol{i}' + (\dot{v}_y + v_x r - h_{\mathrm{S}}\dot{p} + c\dot{r})\boldsymbol{j}'$$
$$+ (v_y p - h_{\mathrm{S}} p^2 + cpr)\boldsymbol{k}' \tag{3.30}$$

$$\ddot{\boldsymbol{r}}_{\mathrm{U}} = (\dot{v}_x - v_y r + er^2)\boldsymbol{i} + (\dot{v}_y + v_x r - e\dot{r})\boldsymbol{j}. \tag{3.31}$$

Equations (3.30) and (3.31) express the total accelerations of the sprung rigid body mass center and the unsprung rigid body mass center, respectively.

Using the unit vector transformations, the total acceleration of the sprung rigid body mass center $\ddot{\boldsymbol{r}}_{\mathrm{S}}$ can be rewritten as:

$$\ddot{\boldsymbol{r}}_{\mathrm{S}} = (\dot{v}_x - v_y r + h_{\mathrm{S}} pr - cr^2)\boldsymbol{i} + (\dot{v}_y + v_x r - h_{\mathrm{S}}\dot{p} + c\dot{r})(\boldsymbol{j}\cos\phi + \boldsymbol{k}\sin\phi)$$
$$+ (v_y p - h_{\mathrm{S}} p^2 + cpr)(-\boldsymbol{j}\sin\phi + \boldsymbol{k}\cos\phi). \tag{3.32}$$

As mentioned above, ϕ is normally small, thus equation (3.32) approximates:

$$\ddot{\boldsymbol{r}}_{\mathrm{S}} = (\dot{v}_x - v_y r + h_{\mathrm{S}} pr - cr^2)\boldsymbol{i} + (\dot{v}_y + v_x r - h_{\mathrm{S}}\dot{p} + c\dot{r})\boldsymbol{j}$$
$$+ (v_y p - h_{\mathrm{S}} p^2 + cpr)\boldsymbol{k}. \tag{3.33}$$

According to equations (3.31) and (3.33), the longitudinal accelerations of the two mass centers, i.e. the acceleration components in the x direction, are:

$$a_{Sx} = \dot{v}_x - v_y r + h_S p r - c r^2 \tag{3.34}$$

$$a_{Ux} = \dot{v}_x - v_y r + e r^2. \tag{3.35}$$

Also, the lateral accelerations of the two mass centers, i.e. the acceleration components in the y direction, are:

$$a_{Sy} = \dot{v}_y + v_x r - h_S \dot{p} + c \dot{r} \tag{3.36}$$

$$a_{Uy} = \dot{v}_y + v_x r - e \dot{r}. \tag{3.37}$$

Applying the Newton's second law, the following governing equation for the longitudinal motion of the entire vehicle is achieved:

$$\begin{aligned}
\sum F_x &= m_S \times a_{Sx} + m_U \times a_{Ux} \\
&= (m_S + m_U)(\dot{v}_x - v_y r) + m_S h_S p r + (m_U e - m_S c) r^2 \\
&= m(\dot{v}_x - v_y r) + m_S h_S p r,
\end{aligned} \tag{3.38}$$

where m_S, m_U and m denote the masses of the sprung rigid body, unsprung rigid body and whole vehicle, respectively, and $\sum F_x$ and $\sum F_y$ represent the total external forces acted on the vehicle in the x and y directions, respectively. Note that $m_S + m_U = m$, and $m_S c = m_U e$ since the origin P is the projection of the mass center of the entire vehicle on the x or x' axis. Likewise, the governing equation for the lateral motion of the entire vehicle is given by:

$$\begin{aligned}
\sum F_y &= m_S \times a_{Sy} + m_U \times a_{Uy} \\
&= (m_S + m_U)(\dot{v}_y + v_x r) - m_S h_S \dot{p} + (m_S c - m_U e) \dot{r} \\
&= m(\dot{v}_y + v_x r) - m_S h_S \dot{p}.
\end{aligned} \tag{3.39}$$

The total external forces in the x and y directions are expressed as:

$$\sum F_x = \sum_{i=1}^{4} (F_{xi} \cos \delta_i - F_{yi} \sin \delta_i) \tag{3.40}$$

$$\sum F_y = \sum_{i=1}^{4} (F_{xi} \sin \delta_i + F_{yi} \cos \delta_i), \tag{3.41}$$

where δ_i represents the steer angle of the ith wheel, and F_{xi} and F_{yi} are the longitudinal and lateral tire forces applied on the ith wheel. Note that for rear wheels $\delta_3 = \delta_4 = 0$, and the cot-average of the front wheel steer angles, δ, is used in place of δ_1 and δ_2

for simplicity ($\cot \delta = (\cot \delta_1 + \cot \delta_2)/2$). The values 1, 2, 3 and 4 of the subscript i represent the front left, front right, rear right and rear left wheel, respectively. The tire forces and wheel steer angles are shown in Figure 1.4.

Substituting equations (3.40) and (3.41) in equations (3.38) and (3.39) respectively, the longitudinal and lateral equations of motion are obtained:

$$\sum_{i=1}^{4} (F_{xi} \cos \delta_i - F_{yi} \sin \delta_i) = m(\dot{v}_x - v_y r) + m_\text{S} h_\text{S} pr \tag{3.42}$$

$$\sum_{i=1}^{4} (F_{xi} \sin \delta_i + F_{yi} \cos \delta_i) = m(\dot{v}_y + v_x r) - m_\text{S} h_\text{S} \dot{p}. \tag{3.43}$$

3.2.2 Rotational motion

The rigid body rotational motion is governed by the Euler's law of motion which, along with the Newton's second law, provides the complete equations of motion for a rigid body. The Euler's law of motion states that:

$$\boldsymbol{M}_\text{G} = \dot{\boldsymbol{H}}_\text{G}, \tag{3.44}$$

where $\boldsymbol{M}_\text{G}$ represents the resultant external moment about the mass center G, and $\boldsymbol{H}_\text{G}$ denotes the angular momentum of the rigid body about its mass center. The general description of the angular momentum of a rigid body expressed in a centroidal (i.e. the origin of the coordinate system is the mass center) body-fixed coordinate system x_G-y_G-z_G reads:

$$\begin{aligned}
\boldsymbol{H}_\text{G} = {} & (I_{\text{G}xx} \omega_{\text{G}x} - I_{\text{G}xy} \omega_{\text{G}y} - I_{\text{G}xz} \omega_{\text{G}z}) \boldsymbol{i}_\text{G} \\
& + (I_{\text{G}yy} \omega_{\text{G}y} - I_{\text{G}xy} \omega_{\text{G}x} - I_{\text{G}yz} \omega_{\text{G}z}) \boldsymbol{j}_\text{G} \\
& + (I_{\text{G}zz} \omega_{\text{G}z} - I_{\text{G}xz} \omega_{\text{G}x} - I_{\text{G}yz} \omega_{\text{G}y}) \boldsymbol{k}_\text{G},
\end{aligned} \tag{3.45}$$

where $\boldsymbol{i}_\text{G}$, $\boldsymbol{j}_\text{G}$ and $\boldsymbol{k}_\text{G}$ represent the unit vectors along the x_G, y_G and z_G axes of the coordinate system x_G-y_G-z_G, respectively, $\omega_{\text{G}x}$, $\omega_{\text{G}y}$ and $\omega_{\text{G}z}$ denote the angular velocity components of the coordinate system x_G-y_G-z_G in the x_G, y_G and z_G directions, respectively, $I_{\text{G}xx}$, $I_{\text{G}yy}$ and $I_{\text{G}zz}$ represent the mass moments of inertia about the x_G, y_G and z_G axes, respectively, and $I_{\text{G}xy}$, $I_{\text{G}yz}$ and $I_{\text{G}xz}$ denote the products of inertia with respect to the $x_\text{G} y_\text{G}$, $y_\text{G} z_\text{G}$ and $x_\text{G} z_\text{G}$ planes, respectively.

To obtain the rotational equation of motion about an arbitrary point B other than the mass center G, we use the more general equation [99]:

$$\boldsymbol{M}_\text{B} = \dot{\boldsymbol{H}}_\text{G} + m_\text{G} \boldsymbol{\rho}_\text{G} \times \boldsymbol{a}_\text{G}, \tag{3.46}$$

where $\boldsymbol{M}_{\mathrm{B}}$ represents the resultant external moment about the point B, m_{G} denotes the mass of the rigid body, $\boldsymbol{\rho}_{\mathrm{G}}$ denotes the position vector of the mass center G with respect to the point B, and $\boldsymbol{a}_{\mathrm{G}}$ stands for the acceleration vector of the mass center G.

With the mechanical model introduced in section 3.1, it is more convenient to compute the external moments about the point P other than the mass centers S and U. Therefore, the more general form of law of motion, equation (3.46), is applied to the sprung rigid body and unsprung rigid body about the point P, respectively.

The angular momentum of the sprung rigid body about its own mass center, S, is firstly looked into. Attaching a centroidal coordinate system x_{S}-y_{S}-z_{S} (parallel to x'-y'-z') to the sprung rigid body, and applying equation (3.45) lead to:

$$\begin{aligned} \boldsymbol{H}_{\mathrm{S}} = {} & (I_{\mathrm{S}xx}\omega_{\mathrm{S}x} - I_{\mathrm{S}xy}\omega_{\mathrm{S}y} - I_{\mathrm{S}xz}\omega_{\mathrm{S}z})\boldsymbol{i}_{\mathrm{S}} \\ & + (I_{\mathrm{S}yy}\omega_{\mathrm{S}y} - I_{\mathrm{S}xy}\omega_{\mathrm{S}x} - I_{\mathrm{S}yz}\omega_{\mathrm{S}z})\boldsymbol{j}_{\mathrm{S}} \\ & + (I_{\mathrm{S}zz}\omega_{\mathrm{S}z} - I_{\mathrm{S}xz}\omega_{\mathrm{S}x} - I_{\mathrm{S}yz}\omega_{\mathrm{S}y})\boldsymbol{k}_{\mathrm{S}}. \end{aligned} \tag{3.47}$$

It is seen from equation (3.10) that the angular velocity components of the sprung rigid body expressed in the coordinate system x'-y'-z' are:

$$\omega_{\mathrm{S}x} = p \tag{3.48}$$

$$\omega_{\mathrm{S}y} = 0 \tag{3.49}$$

$$\omega_{\mathrm{S}z} = r. \tag{3.50}$$

Note that the sprung mass can be safely assumed to be symmetric about the $x_{\mathrm{S}}z_{\mathrm{S}}$ plane, so $I_{\mathrm{S}xy} = I_{\mathrm{S}yz} = 0$. Also, $\boldsymbol{i}_{\mathrm{S}}$, $\boldsymbol{j}_{\mathrm{S}}$ and $\boldsymbol{k}_{\mathrm{S}}$ are parallel to $\boldsymbol{i}'$ $\boldsymbol{j}'$ and $\boldsymbol{k}'$, respectively. Thus, equation (3.47) reduces to:

$$\boldsymbol{H}_{\mathrm{S}} = (I_{\mathrm{S}xx}p - I_{\mathrm{S}xz}r)\boldsymbol{i}' + (I_{\mathrm{S}zz}r - I_{\mathrm{S}xz}p)\boldsymbol{k}'. \tag{3.51}$$

Differentiation of equation (3.51) provides:

$$\begin{aligned} \dot{\boldsymbol{H}}_{\mathrm{S}} = {} & (I_{\mathrm{S}xx}\dot{p} - I_{\mathrm{S}xz}\dot{r})\boldsymbol{i}' + (I_{\mathrm{S}xx}p - I_{\mathrm{S}xz}r)\dot{\boldsymbol{i}}' \\ & + (I_{\mathrm{S}zz}\dot{r} - I_{\mathrm{S}xz}\dot{p})\boldsymbol{k}' + (I_{\mathrm{S}zz}r - I_{\mathrm{S}xz}p)\dot{\boldsymbol{k}}'. \end{aligned} \tag{3.52}$$

Substitution of equations (3.24) and (3.26) in equation (3.52) yields:

$$\begin{aligned} \dot{\boldsymbol{H}}_{\mathrm{S}} = {} & (I_{\mathrm{S}xx}\dot{p} - I_{\mathrm{S}xz}\dot{r})\boldsymbol{i}' + \left[(I_{\mathrm{S}xx} - I_{\mathrm{S}zz})pr - I_{\mathrm{S}xz}r^2 + I_{\mathrm{S}xz}p^2\right]\boldsymbol{j}' \\ & + (I_{\mathrm{S}zz}\dot{r} - I_{\mathrm{S}xz}\dot{p})\boldsymbol{k}'. \end{aligned} \tag{3.53}$$

To utilize equation (3.46), the vectors $\boldsymbol{\rho}_\mathrm{S}$ and $\boldsymbol{a}_\mathrm{S}$ are needed. The vector $\boldsymbol{\rho}_\mathrm{S}$ is expressed by equation (3.12), and the vector $\boldsymbol{a}_\mathrm{S}$ is given by equation (3.30). Thus, the cross product of these two vectors reads:

$$\begin{aligned}
\boldsymbol{\rho}_\mathrm{S} \times \boldsymbol{a}_\mathrm{S} = {}& (c\boldsymbol{i}' + h_\mathrm{S}\boldsymbol{k}') \times \big[(\dot{v}_x - v_y r + h_\mathrm{S}pr - cr^2)\boldsymbol{i}' \\
& + (\dot{v}_y + v_x r - h_\mathrm{S}\dot{p} + c\dot{r})\boldsymbol{j}' + (v_y p - h_\mathrm{S}p^2 + cpr)\boldsymbol{k}'\big] \\
= {}& -h_\mathrm{S}(\dot{v}_y + v_x r - h_\mathrm{S}\dot{p} + c\dot{r})\boldsymbol{i}' \\
& + \big[h_\mathrm{S}(\dot{v}_x - v_y r + h_\mathrm{S}pr - cr^2) - c(v_y p - h_\mathrm{S}p^2 + cpr)\big]\boldsymbol{j}' \\
& + c(\dot{v}_y + v_x r - h_\mathrm{S}\dot{p} + c\dot{r})\boldsymbol{k}'.
\end{aligned} \tag{3.54}$$

Applying equation (3.46) to the sprung rigid body about the point P, and making use of equations (3.53) and (3.54) produce:

$$\begin{aligned}
\boldsymbol{M}_\mathrm{PS} = {}& \dot{\boldsymbol{H}}_\mathrm{S} + m_\mathrm{S}\boldsymbol{\rho}_\mathrm{S} \times \boldsymbol{a}_\mathrm{S} \\
= {}& \big[(I_{\mathrm{S}xx} + m_\mathrm{S}h_\mathrm{S}^2)\dot{p} - (I_{\mathrm{S}xz} + m_\mathrm{S}h_\mathrm{S}c)\dot{r} - m_\mathrm{S}h_\mathrm{S}(\dot{v}_y + v_x r)\big]\boldsymbol{i}' \\
& + \big[(I_{\mathrm{S}xx} + m_\mathrm{S}h_\mathrm{S}^2 - I_{\mathrm{S}zz} - m_\mathrm{S}c^2)pr + (I_{\mathrm{S}xz} + m_\mathrm{S}h_\mathrm{S}c)(p^2 - r^2) \\
& + m_\mathrm{S}h_\mathrm{S}(\dot{v}_x - v_y r) - m_\mathrm{S}cv_y p\big]\boldsymbol{j}' \\
& + \big[(I_{\mathrm{S}zz} + m_\mathrm{S}c^2)\dot{r} - (I_{\mathrm{S}xz} + m_\mathrm{S}h_\mathrm{S}c)\dot{p} + m_\mathrm{S}c(\dot{v}_y + v_x r)\big]\boldsymbol{k}',
\end{aligned} \tag{3.55}$$

where $\boldsymbol{M}_\mathrm{PS}$ is the external moment about the point P which contributes to the rotational motion of the sprung rigid body.

Then, the above procedure is repeated for the unsprung rigid body. Attaching a centroidal coordinate system x_U-y_U-z_U (parallel to x-y-z) to the unsprung rigid body, and applying equation (3.45) lead to:

$$\begin{aligned}
\boldsymbol{H}_\mathrm{U} = {}& (I_{\mathrm{U}xx}\omega_{\mathrm{U}x} - I_{\mathrm{U}xy}\omega_{\mathrm{U}y} - I_{\mathrm{U}xz}\omega_{\mathrm{U}z})\boldsymbol{i}_\mathrm{U} \\
& + (I_{\mathrm{U}yy}\omega_{\mathrm{U}y} - I_{\mathrm{U}xy}\omega_{\mathrm{U}x} - I_{\mathrm{U}yz}\omega_{\mathrm{U}z})\boldsymbol{j}_\mathrm{U} \\
& + (I_{\mathrm{U}zz}\omega_{\mathrm{U}z} - I_{\mathrm{U}xz}\omega_{\mathrm{U}x} - I_{\mathrm{U}yz}\omega_{\mathrm{U}y})\boldsymbol{k}_\mathrm{U}.
\end{aligned} \tag{3.56}$$

According to equation (3.11), the angular velocity components of the unsprung rigid body in the coordinate system x-y-z are:

$$\omega_{\mathrm{U}x} = 0 \tag{3.57}$$

$$\omega_{\mathrm{U}y} = 0 \tag{3.58}$$

$$\omega_{\mathrm{U}z} = r. \tag{3.59}$$

It can be reasonably assumed that the unsprung mass is symmetric about the $x_\mathrm{U}z_\mathrm{U}$ plane, and the height of the unsprung mass in the z_U direction is negligible, thus $I_{\mathrm{U}xy} =$

$I_{\mathrm{U}yz} = I_{\mathrm{U}xz} = 0$ holds. Besides, $\boldsymbol{i}_{\mathrm{U}}$, $\boldsymbol{j}_{\mathrm{U}}$ and $\boldsymbol{k}_{\mathrm{U}}$ are parallel to $\boldsymbol{i}$, $\boldsymbol{j}$ and $\boldsymbol{k}$, respectively. Then, equation (3.56) simplifies to:

$$\boldsymbol{H}_{\mathrm{U}} = I_{\mathrm{U}zz}r\boldsymbol{k}. \tag{3.60}$$

The derivative of equation (3.60) is given by:

$$\dot{\boldsymbol{H}}_{\mathrm{U}} = I_{\mathrm{U}zz}\dot{r}\boldsymbol{k} + I_{\mathrm{U}zz}r\dot{\boldsymbol{k}}. \tag{3.61}$$

Substituting equation (3.29) in equation (3.61) leads to:

$$\dot{\boldsymbol{H}}_{\mathrm{U}} = I_{\mathrm{U}zz}\dot{r}\boldsymbol{k}. \tag{3.62}$$

To apply equation (3.46) to the unsprung rigid body, the vectors $\boldsymbol{\rho}_{\mathrm{U}}$ and $\boldsymbol{a}_{\mathrm{U}}$ are needed. Note that the vector $\boldsymbol{\rho}_{\mathrm{U}}$ is expressed by equation (3.13), and the vector $\boldsymbol{a}_{\mathrm{U}}$ is given by equation (3.31). Thus, the cross product of these two vectors is as follows:

$$\begin{aligned}
\boldsymbol{\rho}_{\mathrm{U}} \times \boldsymbol{a}_{\mathrm{U}} &= (-e\boldsymbol{i}) \times \left[(\dot{v}_x - v_y r + er^2)\boldsymbol{i} + (\dot{v}_y + v_x r - e\dot{r})\boldsymbol{j} \right] \\
&= -e(\dot{v}_y + v_x r - e\dot{r})\boldsymbol{k}.
\end{aligned} \tag{3.63}$$

Applying equation (3.46) to the unsprung rigid body about the point P gives:

$$\begin{aligned}
\boldsymbol{M}_{\mathrm{PU}} &= \dot{\boldsymbol{H}}_{\mathrm{U}} + m_{\mathrm{U}}\boldsymbol{\rho}_{\mathrm{U}} \times \boldsymbol{a}_{\mathrm{U}} \\
&= \left[I_{\mathrm{U}zz}\dot{r} - m_{\mathrm{U}}e(\dot{v}_y + v_x r - e\dot{r}) \right]\boldsymbol{k}.
\end{aligned} \tag{3.64}$$

where $\boldsymbol{M}_{\mathrm{PU}}$ is the external moment about the point P which contributes to the rotational motion of the unsprung rigid body.

Combining equations (3.55) and (3.64) yields:

$$
\begin{aligned}
\boldsymbol{M}_{\mathrm{P}} &= \boldsymbol{M}_{\mathrm{PS}} + \boldsymbol{M}_{\mathrm{PU}} \\
&= \big[(I_{\mathrm{S}xx} + m_{\mathrm{S}}h_{\mathrm{S}}^2)\dot{p} - (I_{\mathrm{S}xz} + m_{\mathrm{S}}h_{\mathrm{S}}c)\dot{r} - m_{\mathrm{S}}h_{\mathrm{S}}(\dot{v}_y + v_x r)\big]\boldsymbol{i}' \\
&\quad + \big[(I_{\mathrm{S}xx} + m_{\mathrm{S}}h_{\mathrm{S}}^2 - I_{\mathrm{S}zz} - m_{\mathrm{S}}c^2)pr + (I_{\mathrm{S}xz} + m_{\mathrm{S}}h_{\mathrm{S}}c)(p^2 - r^2) \\
&\quad + m_{\mathrm{S}}h_{\mathrm{S}}(\dot{v}_x - v_y r) - m_{\mathrm{S}}cv_y p\big]\boldsymbol{j}' \\
&\quad + \big[(I_{\mathrm{S}zz} + m_{\mathrm{S}}c^2)\dot{r} - (I_{\mathrm{S}xz} + m_{\mathrm{S}}h_{\mathrm{S}}c)\dot{p} + m_{\mathrm{S}}c(\dot{v}_y + v_x r)\big]\boldsymbol{k}' \\
&\quad + \big[(I_{\mathrm{U}zz} + m_{\mathrm{U}}e^2)\dot{r} - m_{\mathrm{U}}e(\dot{v}_y + v_x r)\big]\boldsymbol{k} \\
&= \big[(I_{\mathrm{S}xx} + m_{\mathrm{S}}h_{\mathrm{S}}^2)\dot{p} - (I_{\mathrm{S}xz} + m_{\mathrm{S}}h_{\mathrm{S}}c)\dot{r} - m_{\mathrm{S}}h_{\mathrm{S}}(\dot{v}_y + v_x r)\big]\boldsymbol{i} \\
&\quad + \big[(I_{\mathrm{S}xx} + m_{\mathrm{S}}h_{\mathrm{S}}^2 - I_{\mathrm{S}zz} - m_{\mathrm{S}}c^2)pr + (I_{\mathrm{S}xz} + m_{\mathrm{S}}h_{\mathrm{S}}c)(p^2 - r^2) \\
&\quad + m_{\mathrm{S}}h_{\mathrm{S}}(\dot{v}_x - v_y r) - m_{\mathrm{S}}cv_y p\big](\boldsymbol{j}\cos\phi + \boldsymbol{k}\sin\phi) \\
&\quad + \big[(I_{\mathrm{S}zz} + m_{\mathrm{S}}c^2)\dot{r} - (I_{\mathrm{S}xz} + m_{\mathrm{S}}h_{\mathrm{S}}c)\dot{p} + m_{\mathrm{S}}c(\dot{v}_y + v_x r)\big](-\boldsymbol{j}\sin\phi + \boldsymbol{k}\cos\phi) \\
&\quad + \big[(I_{\mathrm{U}zz} + m_{\mathrm{U}}e^2)\dot{r} - m_{\mathrm{U}}e(\dot{v}_y + v_x r)\big]\boldsymbol{k},
\end{aligned}
\tag{3.65}
$$

where $\boldsymbol{M}_{\mathrm{P}}$ denotes the resultant external moment about the point P. As mentioned in section (3.2.1), the sprung mass roll angle ϕ is small (thus $\cos\phi \approx 1$ and $\sin\phi \approx 0$), then equation (3.65) reduces to:

$$
\begin{aligned}
\boldsymbol{M}_{\mathrm{P}} &= \big[I_x\dot{p} - I_{xz}\dot{r} - m_{\mathrm{S}}h_{\mathrm{S}}(\dot{v}_y + v_x r)\big]\boldsymbol{i} + \big[(I_x - I_{\mathrm{S}zz} - m_{\mathrm{S}}c^2)pr + I_{xz}(p^2 - r^2) \\
&\quad + m_{\mathrm{S}}h_{\mathrm{S}}(\dot{v}_x - v_y r) - m_{\mathrm{S}}cv_y p\big]\boldsymbol{j} + (I_z\dot{r} - I_{xz}\dot{p})\boldsymbol{k},
\end{aligned}
\tag{3.66}
$$

where

$$
\begin{aligned}
I_x &= I_{\mathrm{S}xx} + m_{\mathrm{S}}h_{\mathrm{S}}^2 \\
I_{xz} &= I_{\mathrm{S}xz} + m_{\mathrm{S}}h_{\mathrm{S}}c \\
I_z &= I_{\mathrm{S}zz} + m_{\mathrm{S}}c^2 + I_{\mathrm{U}zz} + m_{\mathrm{U}}e^2.
\end{aligned}
$$

Note that I_x represents the roll moment of inertia of the sprung mass about the x axis, I_{xz} denotes the product of inertia of the sprung mass with respect to the xz plane, and I_z is the yaw moment of inertia of the entire vehicle (the sum of the sprung and unsprung masses) about the z axis.

Based on equation (3.66), the following governing equations for the roll and yaw motions can be derived:

$$
M_{\mathrm{P}x} = I_x\dot{p} - I_{xz}\dot{r} - m_{\mathrm{S}}h_{\mathrm{S}}(\dot{v}_y + v_x r)
\tag{3.67}
$$

$$
M_{\mathrm{P}z} = I_z\dot{r} - I_{xz}\dot{p},
\tag{3.68}
$$

where $M_{\mathrm{P}x}$ and $M_{\mathrm{P}z}$ denote the external moment components in the x and z directions, respectively, and are expressed as follows:

$$M_{\mathrm{P}x} = -K_\phi \phi + m_{\mathrm{S}} g h_{\mathrm{S}} \sin\phi - C_\phi p \tag{3.69}$$

$$M_{\mathrm{P}z} = \sum_{i=1}^{4} x_i (F_{xi}\sin\delta_i + F_{yi}\cos\delta_i) - \sum_{i=1}^{4} y_i (F_{xi}\cos\delta_i - F_{yi}\sin\delta_i), \tag{3.70}$$

where K_ϕ and C_ϕ denote the total roll stiffness and total roll damping of the suspension system, respectively, g represents the gravitational acceleration, and x_i and y_i are the coordinates of the ith wheel in the x-y-z coordinate system.

Combining equations (3.67)–(3.70), the following roll and yaw equations of motion are achieved:

$$-K_\phi \phi + m_{\mathrm{S}} g h_{\mathrm{S}} \sin\phi - C_\phi p = I_x \dot{p} - I_{xz}\dot{r} - m_{\mathrm{S}} h_{\mathrm{S}}(\dot{v}_y + v_x r) \tag{3.71}$$

$$\sum_{i=1}^{4} x_i (F_{xi}\sin\delta_i + F_{yi}\cos\delta_i) - \sum_{i=1}^{4} y_i (F_{xi}\cos\delta_i - F_{yi}\sin\delta_i) = I_z \dot{r} - I_{xz}\dot{p}. \tag{3.72}$$

Equations (3.71) and (3.72), along with equations (3.42) and (3.43) derived in section 3.2.1, constitute the complete set of vehicle equations of motion that govern the longitudinal, lateral, roll and yaw motions. In the subsequent chapters, these equations of motion are employed as the mathematical representation of the plant (i.e. the vehicle) in the DYC design process, also, they are adopted in the simulation model to compute the vehicle states of the simulated vehicle.

3.3   WHEEL EQUATION OF MOTION

To adopt the vehicle equations of motion in the simulation model, the values of the longitudinal and lateral tire forces (i.e. F_{xi} and F_{yi}) are required, as can be seen from equations (3.42), (3.43) and (3.72). Thus, the well-known *Magic Formula* tire model is used to generate these tire forces. Since the wheel slip ratio is one of the inputs to the *Magic Formula* model, in this section, the wheel dynamics is modeled to calculate the wheel angular velocity, and in turn the wheel slip ratio (wheel longitudinal slip).

Based on the wheel force system presented in Figure 3.3, the following moment equilibrium equation about the center of the wheel can be established:

$$J\frac{d\omega}{dt} = T - F_x R - F_z a, \tag{3.73}$$

where J denotes the mass moment of inertia of the wheel assembly, ω stands for the wheel angular velocity, T represents the motor torque (assuming no gear reduction is
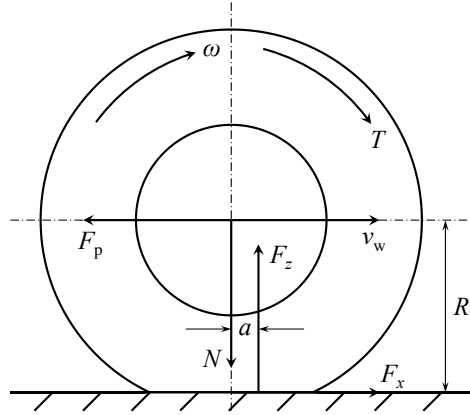
FIGURE 3.3: Wheel schematic.

used), F_x is the longitudinal tire force, R is the tire radius, F_z is the normal reaction force from the ground, a is the tire pneumatic trail, N is the wheel normal load, F_p is the reaction force from the driving axle and v_w is the velocity of the wheel center in its heading direction. As in this thesis a rear-wheel-drive electric vehicle is considered, when applying equation (3.73) to the front wheels the T term is not included.

3.4 TIRE MODEL

The well-known *Magic Formula* equations are employed to model the tire dynamics in this study, in order to generate the tire forces required in the vehicle equations of motion. It has been proven that the tire forces predicted by the *Magic Formula* equations closely match the actual tire forces, thus this tire model has been widely utilized in vehicle dynamic analysis [70, 100–102]. The basic *Magic Formula* equation is written as follows [103]:

$$y(x) = D \sin \left\{ C \arctan \left[Bx - E(Bx - \arctan Bx) \right] \right\} \tag{3.74}$$

with

$$Y(X) = y(x) + S_\mathrm{V} \tag{3.75}$$

$$x = X + S_\mathrm{H} \tag{3.76}$$

where X represents the wheel slip ratio λ or the tire slip angle α, $Y(X)$ denotes the tire force F_x or F_y, S_H and S_V are the horizontal shift and vertical shift, respectively, B, C, D and E are the stiffness factor, shape factor, peak value and curvature factor, respectively.

The meanings and detailed mathematical expressions for B, C, D, E, S_H and S_V are available in [103]. The calculation of these parameters requires the value of the wheel slip ratio λ, tire slip angle α and normal reaction force F_z.

The wheel slip ratio λ used in the *Magic Formula* is defined as [104]:

$$\lambda = \frac{R\omega}{v_{\mathrm{w}x}} - 1. \tag{3.77}$$

where $v_{\mathrm{w}x}$ denotes the velocity of the wheel center in the wheel heading direction. Based on equation (3.4), the following vector equation can be derived:

$$\boldsymbol{v}_i = \boldsymbol{v}_\mathrm{P} + \boldsymbol{\omega}_\mathrm{U} \times \boldsymbol{\rho}_i, \tag{3.78}$$

where $\boldsymbol{v}_i$ denotes the velocity vector of the ith wheel center, $\boldsymbol{v}_\mathrm{P}$ represents the velocity vector of the point P (the origin of the coordinate systems x-y-z and x'-y'-z'), and $\boldsymbol{\rho}_i$ is the position vector of the ith wheel center with respect to the point P. Expanding equation (3.78) gives:

$$\boldsymbol{v}_1 = (v_x - \frac{d_\mathrm{f}}{2}r)\boldsymbol{i} + (v_y + l_\mathrm{f}r)\boldsymbol{j} \tag{3.79}$$

$$\boldsymbol{v}_2 = (v_x + \frac{d_\mathrm{f}}{2}r)\boldsymbol{i} + (v_y + l_\mathrm{f}r)\boldsymbol{j} \tag{3.80}$$

$$\boldsymbol{v}_3 = (v_x + \frac{d_\mathrm{r}}{2}r)\boldsymbol{i} + (v_y - l_\mathrm{r}r)\boldsymbol{j} \tag{3.81}$$

$$\boldsymbol{v}_4 = (v_x - \frac{d_\mathrm{r}}{2}r)\boldsymbol{i} + (v_y - l_\mathrm{r}r)\boldsymbol{j}, \tag{3.82}$$

where d_f and d_r represent the front and rear track widths, respectively, l_f and l_r denote the distances from the point P to the front axle (wheel center) and rear axle (wheel center), respectively. These parameters are shown in Figure 1.4. Using equations (3.79)–(3.82) and considering the front wheel steer angle δ, the velocities of each wheel center in the wheel heading direction are obtained as follows:

$$v_{\mathrm{w}x1} = (v_x - \frac{d_\mathrm{f}}{2}r)\cos\delta + (v_y + l_\mathrm{f}r)\sin\delta \tag{3.83}$$

$$v_{\mathrm{w}x2} = (v_x + \frac{d_\mathrm{f}}{2}r)\cos\delta + (v_y + l_\mathrm{f}r)\sin\delta \tag{3.84}$$

$$v_{\mathrm{w}x3} = v_x + \frac{d_\mathrm{r}}{2}r \tag{3.85}$$

$$v_{\mathrm{w}x4} = v_x - \frac{d_\mathrm{r}}{2}r. \tag{3.86}$$

Apart from the wheel slip ratio, the calculation of the *Magic Formula* parameters also requires the tire slip angle which is defined as the angle between the wheel heading direction and the velocity vector of the wheel center [104]. Employing equations (3.79)–(3.82) and considering the suspension roll steer caused by the roll motion, the tire slip
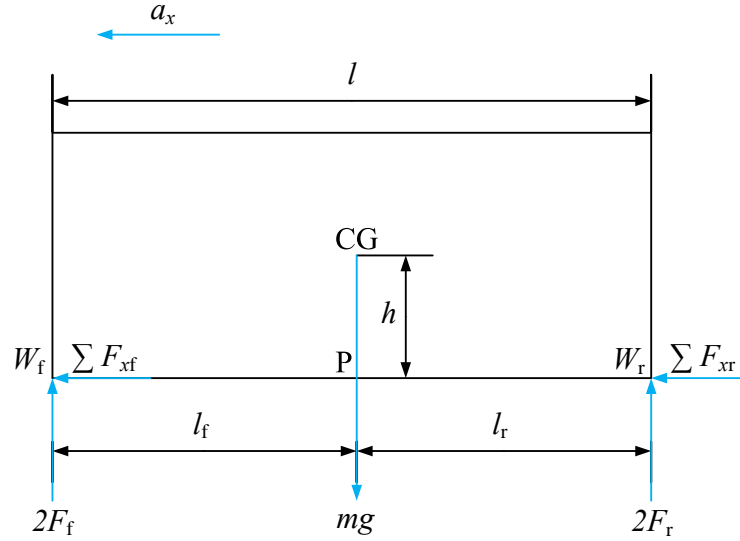
FIGURE 3.4: Schematic of the vehicle longitudinal motion.

angle for each tire is expressed as:

$$\alpha_1 = \arctan \frac{v_y + l_{\text{f}}r}{v_x - \frac{d_{\text{f}}}{2}r} - \delta - C_{\delta\text{f}}\phi \tag{3.87}$$

$$\alpha_2 = \arctan \frac{v_y + l_{\text{f}}r}{v_x + \frac{d_{\text{f}}}{2}r} - \delta - C_{\delta\text{f}}\phi \tag{3.88}$$

$$\alpha_3 = \arctan \frac{v_y - l_{\text{r}}r}{v_x + \frac{d_{\text{r}}}{2}r} - C_{\delta\text{r}}\phi \tag{3.89}$$

$$\alpha_4 = \arctan \frac{v_y - l_{\text{r}}r}{v_x - \frac{d_{\text{r}}}{2}r} - C_{\delta\text{r}}\phi, \tag{3.90}$$

where $C_{\delta\text{f}}$ and $C_{\delta\text{r}}$ represent the front and rear roll steer coefficients, respectively.

In addition to the wheel slip ratio λ and tire slip angle α, the parameters in the *Magic Formula* are also dependent on the normal reaction force F_z (or the normal load N) which are subject to the longitudinal and lateral load transfers. When the vehicle is stationary, the static normal reaction forces applied on the four wheels are:

$$F_{\text{fs}} = \frac{1}{2l}mgl_{\text{r}} \tag{3.91}$$

$$F_{\text{rs}} = \frac{1}{2l}mgl_{\text{f}}, \tag{3.92}$$

where F_{fs} and F_{rs} denote the static normal reaction forces exerted on one front wheel and one rear wheel, respectively.

The normal reaction force is changed due to the longitudinal load transfer. Figure 3.4 shows the schematic of the vehicle longitudinal motion. Since the pitch motion is neglected in the vehicle equivalent mechanical model, we treat the sprung and unsprung masses as a whole and consider that they produce the same motion in the x direction.
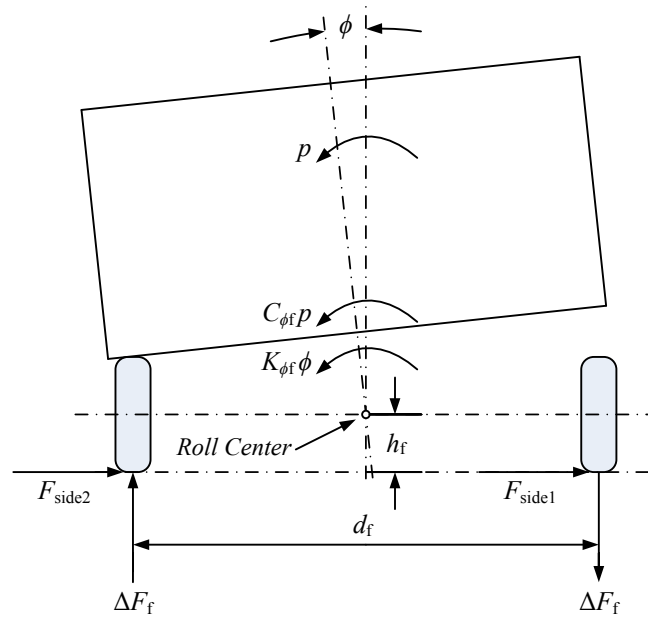
FIGURE 3.5: Front view of the vehicle equivalent mechanical model.

The points W_f and W_r represent the tire-road contact centers of the front and rear wheels, respectively, h denotes the height of the mass center of the entire vehicle (point CG) from the ground, and $\sum F_{xf}$ and $\sum F_{xr}$ represent the total front and rear tire forces in the x direction ($\sum F_{xf} + \sum F_{xr} = \sum F_x$), respectively. Taking moment about the mass center CG and considering the force equilibrium in the z direction lead to the following normal reaction forces for one front wheel and one rear wheel, respectively:

$$F_f = \frac{1}{2l}(mgl_r - h\sum F_x) \tag{3.93}$$

$$F_r = \frac{1}{2l}(mgl_f + h\sum F_x). \tag{3.94}$$

Then, the effect of the lateral load transfer caused by the roll motion is taken into account. The roll motion of the unsprung rigid body is illustrated in Figure 3.5, the front view of the vehicle equivalent mechanical model. As shown in this figure, the roll moment about the front roll center in the plane perpendicular to the x axis has to be in equilibrium, which leads to the following lateral load change between the front wheels:

$$\Delta F_f = \frac{1}{d_f}\left[K_{\phi f}\phi + C_{\phi f}p + h_f(F_{side1} + F_{side2})\right], \tag{3.95}$$

where h_f denotes the front roll center height, $K_{\phi f}$ and $C_{\phi f}$ are the roll stiffness and the roll damping of the front suspension, respectively. Similarly, the lateral load change between the rear wheels is:

$$\Delta F_r = \frac{1}{d_r}\left[K_{\phi r}\phi + C_{\phi r}p + h_r(F_{side3} + F_{side4})\right], \tag{3.96}$$

where h_r denotes the rear roll center height, $K_{\phi\mathrm{r}}$ and $C_{\phi\mathrm{r}}$ are the roll stiffness and the roll damping of the rear suspension, respectively. The side forces F_side1, F_side2, F_side3 and F_side4 in equations (3.95) and (3.96) are expressed as follows:

$$F_\mathrm{side1} = F_{x1} \sin \delta + F_{y1} \cos \delta \tag{3.97}$$

$$F_\mathrm{side2} = F_{x2} \sin \delta + F_{y2} \cos \delta, \tag{3.98}$$

$$F_\mathrm{side3} = F_{y3} \tag{3.99}$$

$$F_\mathrm{side4} = F_{y4}. \tag{3.100}$$

Introducing equations (3.97) to (3.100) to equations (3.95) and (3.96) provides:

$$\Delta F_\mathrm{f} = \frac{1}{d_\mathrm{f}}(K_{\phi\mathrm{f}}\phi + C_{\phi\mathrm{f}}p + h_\mathrm{f} \sum F_{y\mathrm{f}}) \tag{3.101}$$

$$\Delta F_\mathrm{r} = \frac{1}{d_\mathrm{r}}(K_{\phi\mathrm{r}}\phi + C_{\phi\mathrm{r}}p + h_\mathrm{r} \sum F_{y\mathrm{r}}), \tag{3.102}$$

where

$$\sum F_{y\mathrm{f}} = (F_{x1} + F_{x2}) \sin \delta + (F_{y1} + F_{y2}) \cos \delta \tag{3.103}$$

$$\sum F_{y\mathrm{r}} = F_{y3} + F_{y4}. \tag{3.104}$$

Note that this approach of computing ΔF_f and ΔF_r is also available in [105].

Now, combining equations (3.93), (3.94), (3.101), and (3.102), the normal reaction forces for each wheel considering both the longitudinal and lateral load transfers are written as follows:

$$F_{z1} = \frac{1}{2l}(mgl_\mathrm{r} - h \sum F_x) - \frac{1}{d_\mathrm{f}}(K_{\phi\mathrm{f}}\phi + C_{\phi\mathrm{f}}p + h_\mathrm{f} \sum F_{y\mathrm{f}}) \tag{3.105}$$

$$F_{z2} = \frac{1}{2l}(mgl_\mathrm{r} - h \sum F_x) + \frac{1}{d_\mathrm{f}}(K_{\phi\mathrm{f}}\phi + C_{\phi\mathrm{f}}p + h_\mathrm{f} \sum F_{y\mathrm{f}}) \tag{3.106}$$

$$F_{z3} = \frac{1}{2l}(mgl_\mathrm{f} + h \sum F_x) + \frac{1}{d_\mathrm{r}}(K_{\phi\mathrm{r}}\phi + C_{\phi\mathrm{r}}p + h_\mathrm{r} \sum F_{y\mathrm{r}}) \tag{3.107}$$

$$F_{z4} = \frac{1}{2l}(mgl_\mathrm{f} + h \sum F_x) - \frac{1}{d_\mathrm{r}}(K_{\phi\mathrm{r}}\phi + C_{\phi\mathrm{r}}p + h_\mathrm{r} \sum F_{y\mathrm{r}}). \tag{3.108}$$

Note that the wheel numbering follows the same manner as before.

So far, the establishment of the full vehicle model has been completed. This model includes the vehicle equivalent mechanical model, vehicle equations of motion, wheel equation of motion and *Magic Formula* tire model. This full vehicle model is programed in the MATLAB/Simulink environment for the simulation studies. The details of the MATLAB/Simulink model are shown in Appendix. The vehicle equations of motion are employed in the DYC design process in the following chapters.

Chapter 4

Yaw Rate-Based Direct Yaw Moment Control

In this chapter, a mathematical relationship between the yaw rate and the corrective yaw moment produced by the DYC system is derived from the vehicle equations of motion established in Chapter 3. This mathematical relationship reveals that the steady-state yaw rate directly depends on the torque difference between the left and right driving motors, which implies that it can be controlled by tuning this torque difference. Based on this relationship, a yaw rate-based DYC method is proposed to achieve neutral steer. Comparative simulation results show that the proposed DYC method closely tracks the reference yaw rate associated with neutral steer, also it outperforms the competing methods in terms of tracking the desired yaw rate and vehicle path in various driving scenarios.

4.1   BACKGROUND

As introduced in Chapter 1, the yaw rate r is the vehicle angular velocity about the z axis of the vehicle local coordinate x-y-z, as shown in Figure 1.4. The yaw rate plays a crucial roll in vehicle stability and handling control, and is one of the main control variables for DYC systems. Firstly, the steady-state yaw rate (derived from the common bicycle model) is a function of the front wheel steer angle. So, it is interpreted as the vehicle response commanded by the driver. Secondly, this steady-state yaw rate value defines the steer characteristic (i.e. under, over, or neutral steer) of the vehicle. To enhance vehicle handling, in this chapter a yaw rate-based DYC method is proposed to drive the yaw rate towards a desired/target value that would lead to neutral steer.

In Chapter 2, several typical types of control methods have been reviewed, including the equal torque methods [27–33], the Ackerman methods [38–46] and the yaw rate-based DYC methods which employ equation (2.5) with a positive K as the reference yaw rate [48, 50, 54, 55]. In the simulation studies in this chapter, to verify the effectiveness of the proposed DYC, the control performances of the proposed method and the aforesaid three types of methods are compared. Here, the concepts and principles behind these methods are recalled.

The equal torque methods are the most straightforward solutions for controlling two independent motors. They emulate the behavior of an open differential by applying equal torques to the two driving wheels. Thus, these methods provide the electric vehicle with a cornering performance similar to an ICE vehicle equipped with an open differential. Actually, the equal torque methods cannot be categorized as DYC systems, as no active yaw moment can be generated to regulate vehicle motion.

The Ackerman methods use the vehicle speed and the front wheel steer angle the as input parameters and calculate the required inner and outer wheel angular velocities, by means of the well-known Ackerman steering geometry. When the electric vehicle enters a corner, the control system acts immediately on both motors, reducing the angular velocity of the inner wheel while increasing that of the outer wheel [38] to their desired values defined by equations (2.2) and (2.3). In the simulation studies, to examine the performance of the Ackerman methods, the driving wheel angular velocities have been tuned based on their sum and difference, with the sum being proportional to the speed command read from the throttle pedal sensor and the difference computed from equations (2.2) and (2.3) as follows:

$$\Delta\omega = \omega_\mathrm{R} - \omega_\mathrm{L} = \frac{v_\mathrm{r} d_\mathrm{r} \tan\delta}{Rl}. \tag{4.1}$$

Note that neither the equal torque methods nor the Ackerman methods take into account the vehicle dynamics. New DYC designs have been proposed in the literature to incorporate the vehicle dynamics, by maintaining the yaw rate at a desired level determined by a planar vehicle dynamic model. This desired yaw rate is described by equation (2.5) in which the stability factor K is normally maintained at a positive value to provide sufficient stability margin for the vehicle. However, a positive stability factor causes understeer and makes the vehicle "reluctant" to turn, which is not optimum for vehicle handling. In the proposed DYC design, $K = 0$ is selected to achieve the ideal steer characteristic, neutral steer, without impairing the vehicle stability. The advantageous vehicle handling performance with no loss in the stability is fully demonstrated in highly challenging driving scenarios, as presented in the simulation results.

4.2 VEHICLE CONTROL MODEL DERIVATION

In this section, a vehicle control model, i.e. a simplified set of vehicle equations of motion, is derived to provide more insight into the design of a yaw rate-based DYC scheme. Recall that the complete vehicle equations of motion, equations (3.42), (3.43), (3.71) and (3.72), govern the vehicle longitudinal, lateral, roll and yaw motions. These equations are rewritten here:

$$\sum_{i=1}^{4}(F_{xi}\cos\delta_i - F_{yi}\sin\delta_i) = m(\dot{v}_x - v_y r) + m_S h_S pr \tag{4.2}$$

$$\sum_{i=1}^{4}(F_{xi}\sin\delta_i + F_{yi}\cos\delta_i) = m(\dot{v}_y + v_x r) - m_S h_S \dot{p} \tag{4.3}$$

$$-K_\phi\phi + m_S g h_S \sin\phi - C_\phi p = I_x \dot{p} - I_{xz}\dot{r} - m_S h_S(\dot{v}_y + v_x r) \tag{4.4}$$

$$\sum_{i=1}^{4} x_i(F_{xi}\sin\delta_i + F_{yi}\cos\delta_i) - \sum_{i=1}^{4} y_i(F_{xi}\cos\delta_i - F_{yi}\sin\delta_i) = I_z\dot{r} - I_{xz}\dot{p}. \tag{4.5}$$

To reveal the fundamental mathematical relationships that govern the vehicle dynamics with a DYC system on-board, in the following, equations (4.2)–(4.5) are simplified and linearized, and the implications deduced from the resulting equations are investigated.

When the ith tire undergoes a normal load and a lateral tire force, its path of motion makes an angle α_i with respect to the tire plane [106]. This angle is called the tire slip angle, whose definition and mathematical expression have been given in section 3.4. When α_i is small, the lateral tire force can be considered linearly proportional to α_i, which reads:

$$F_{yi} = -C_{\alpha i}\alpha_i \tag{4.6}$$

where C_{α_i} is called the cornering stiffness of the ith tire. When a vehicle rolls, it is known that the wheel camber angle will change which in turn results in a tire camber thrust. To accommodate the effect of the camber angle, a new term is added to the lateral tire force equation [107]:

$$F_{yi} = -C_{\alpha i}\alpha_i - C_{\phi i}\phi \tag{4.7}$$

where $C_{\phi i}$ is the tire camber thrust coefficient of the ith tire.

Assuming that the front wheel steer angle δ and the vehicle side-slip angle β are small, and considering a two DoF planar vehicle model (bicycle model) [20] whose track widths

are neglected, the mathematical expressions of the tire slip angles (equations (3.87)–(3.90)) can be simplified to

$$\alpha_1 = \alpha_2 \approx \frac{v_y + l_{\mathrm{f}}r}{v_x} - \delta - C_{\delta\mathrm{f}}\phi \approx \beta + \frac{l_{\mathrm{f}}r}{v_x} - \delta - C_{\delta\mathrm{f}}\phi \tag{4.8}$$

$$\alpha_3 = \alpha_4 \approx \frac{v_y - l_{\mathrm{r}}r}{v_x} - C_{\delta\mathrm{r}}\phi \approx \beta - \frac{l_{\mathrm{r}}r}{v_x} - C_{\delta\mathrm{r}}\phi. \tag{4.9}$$

Substituting equations (4.8) and (4.9) in equation (4.7), the following lateral tire force expressions for the four wheels are obtained:

$$F_{y1} = -C_{\alpha 1}(\beta + \frac{l_{\mathrm{f}}r}{v_x} - \delta - C_{\delta\mathrm{f}}\phi) - C_{\phi 1}\phi \tag{4.10}$$

$$F_{y2} = -C_{\alpha 2}(\beta + \frac{l_{\mathrm{f}}r}{v_x} - \delta - C_{\delta\mathrm{f}}\phi) - C_{\phi 2}\phi \tag{4.11}$$

$$F_{y3} = -C_{\alpha 3}(\beta - \frac{l_{\mathrm{r}}r}{v_x} - C_{\delta\mathrm{r}}\phi) - C_{\phi 3}\phi \tag{4.12}$$

$$F_{y4} = -C_{\alpha 4}(\beta - \frac{l_{\mathrm{r}}r}{v_x} - C_{\delta\mathrm{r}}\phi) - C_{\phi 4}\phi. \tag{4.13}$$

It is assumed that the longitudinal tire forces are symmetric, i.e. $F_{x1} = F_{x2}$ and $F_{x3} = F_{x4}$, and that the front wheel steer angle δ and the sprung mass roll angle ϕ are both small (thus $\sin\delta \approx 0$, $\cos\delta \approx 1$ and $\sin\phi \approx \phi$). Then, substituting equations (4.10)–(4.13) in the left-hand side terms in equations (4.2)–(4.5) leads to:

$$\sum F_x = F_{x1} + F_{x2} + F_{x3} + F_{x4} \tag{4.14}$$

$$\sum F_y = -C_{\alpha\mathrm{f}}(\beta + \frac{l_{\mathrm{f}}r}{v_x} - \delta - C_{\delta\mathrm{f}}\phi) - C_{\phi\mathrm{f}}\phi - C_{\alpha\mathrm{r}}(\beta - \frac{l_{\mathrm{r}}r}{v_x} - C_{\delta\mathrm{r}}\phi) - C_{\phi\mathrm{r}}\phi \tag{4.15}$$

$$M_{\mathrm{P}x} = -K_\phi\phi + m_{\mathrm{S}}gh_{\mathrm{S}}\phi - C_\phi p \tag{4.16}$$

$$M_{\mathrm{P}z} = -l_{\mathrm{f}}\Big[C_{\alpha\mathrm{f}}(\beta + \frac{l_{\mathrm{f}}r}{v_x} - \delta - C_{\delta\mathrm{f}}\phi) + C_{\phi\mathrm{f}}\phi\Big] + l_{\mathrm{r}}\Big[C_{\alpha\mathrm{r}}(\beta - \frac{l_{\mathrm{r}}r}{v_x} - C_{\delta\mathrm{r}}\phi) + C_{\phi\mathrm{r}}\phi\Big] \tag{4.17}$$

where $C_{\alpha\mathrm{f}} = C_{\alpha 1} + C_{\alpha 2}$ and $C_{\alpha\mathrm{r}} = C_{\alpha 3} + C_{\alpha 4}$ are the sums of the left and right tire cornering stiffnesses for the front tires and rear tires, respectively, and $C_{\phi\mathrm{f}} = C_{\phi 1} + C_{\phi 2}$ and $C_{\phi\mathrm{r}} = C_{\phi 3} + C_{\phi 4}$ are the sums of the left and right tire camber thrust coefficients for the front tires and rear tires, respectively.

To retain the linearity of the equations of motion, in the following analysis, the vehicle longitudinal dynamics is neglected (assuming v_x is constant). Note that the vehicle longitudinal motion is generated due to traction and braking without direct relation to steering, thus this motion is not directly connected to the vehicle lateral and yaw motions which are generated by steering the vehicle [96]. Hence, it is a common practice to neglect the vehicle longitudinal dynamics when the focus is on the vehicle lateral and yaw behaviors [108, 109].

Equation (4.14) is no more considered as the vehicle longitudinal dynamics is neglected, then equations (4.15)–(4.17) are rearranged as follows:

$$\sum F_y = a_\beta\beta + a_r r + a_\phi\phi + a_\delta\delta \tag{4.18}$$

$$M_{\mathrm{P}x} = b_\phi\phi + b_p p \tag{4.19}$$

$$M_{\mathrm{P}z} = c_\beta\beta + c_r r + c_\phi\phi + c_\delta\delta, \tag{4.20}$$

where,

$$a_\beta = -C_{\alpha\mathrm{f}} - C_{\alpha\mathrm{r}} \tag{4.21}$$

$$a_r = -C_{\alpha\mathrm{f}}\frac{l_\mathrm{f}}{v_x} + C_{\alpha\mathrm{r}}\frac{l_\mathrm{r}}{v_x} \tag{4.22}$$

$$a_\phi = C_{\alpha\mathrm{f}}C_{\delta\mathrm{f}} - C_{\phi\mathrm{f}} + C_{\alpha\mathrm{r}}C_{\delta\mathrm{r}} - C_{\phi\mathrm{r}} \tag{4.23}$$

$$a_\delta = C_{\alpha\mathrm{f}} \tag{4.24}$$

$$b_\phi = -K_\phi + m_\mathrm{S}gh_\mathrm{S} \tag{4.25}$$

$$b_p = -C_\phi \tag{4.26}$$

$$c_\beta = -l_\mathrm{f}C_{\alpha\mathrm{f}} + l_\mathrm{r}C_{\alpha\mathrm{r}} \tag{4.27}$$

$$c_r = -C_{\alpha\mathrm{f}}\frac{l_\mathrm{f}^2}{v_x} - C_{\alpha\mathrm{r}}\frac{l_\mathrm{r}^2}{v_x} \tag{4.28}$$

$$c_\phi = l_\mathrm{f}C_{\alpha\mathrm{f}}C_{\delta\mathrm{f}} - l_\mathrm{f}C_{\phi\mathrm{f}} - l_\mathrm{r}C_{\alpha\mathrm{r}}C_{\delta\mathrm{r}} + l_\mathrm{r}C_{\phi\mathrm{r}} \tag{4.29}$$

$$c_\delta = l_\mathrm{f}C_{\alpha\mathrm{f}}. \tag{4.30}$$

Thus, equations (4.3)–(4.5) which govern the vehicle lateral, roll and yaw motions can be rewritten as:

$$a_\beta\beta + a_r r + a_\phi\phi + a_\delta\delta = m(\dot{v}_y + v_x r) - m_\mathrm{S}h_\mathrm{S}\dot{p} \tag{4.31}$$

$$b_\phi\phi + b_p p = I_x\dot{p} - I_{xz}\dot{r} - m_\mathrm{S}h_\mathrm{S}(\dot{v}_y + v_x r) \tag{4.32}$$

$$c_\beta\beta + c_r r + c_\phi\phi + c_\delta\delta = I_z\dot{r} - I_{xz}\dot{p}. \tag{4.33}$$

The simplified vehicle equations of motion (4.31)–(4.33) constitute the vehicle control model, and they will be adopted in the next section to derive the control law for the proposed yaw rate-based DYC system.

So far, the small angle assumption has been employed several times in the above derivations. It is important to justify that the usage of the small angle assumption retains the validity of the above simplified vehicle equations of motion (4.31)–(4.33).

The application of the small angle assumption to α can be justified by an example in [110], a typical racing tire inflated at 31 psi for a given load of 1800 lb. This Goodyear racing tire provides the maximum lateral force at a tire slip angle of about 6.5° after

which the tire enters an unstable frictional range. Notice that $6.5°$ is only about 0.1 rad and the tire normally operates in the range below $6.5°$, which allows a safe application of the small angle assumption to α in the linearization.

As for δ, assuming a steering ratio of 1:12, a small front wheel steer angle of 0.2 rad is corresponding to a steering wheel/column angle of about $138°$. At a medium vehicle speed, say 60 km/h, this steer angle is a typical marginal magnitude beyond which the vehicle tends to lose stability. So in the stable region, the vehicle will mostly operate with a smaller steer angle at that speed, which in turn makes it justified to apply the small angle assumption to the front wheel steer angle δ.

Furthermore, when both α and δ are assumed to be small, the associated vehicle side-slip angle β becomes small as well. Summing up the above points, the vehicle control model (i.e. the simplified vehicle equations of motion (4.31)–(4.33)) obtained by means of small angle assumptions are practically valid and can capture the major characteristics of the vehicle dynamics. As can be seen in the next section, this model is utilized to derive the relationship between the steady-state yaw rate and the left-right motor torque difference, based on which the proposed DYC system is designed.

4.3 YAW RATE-BASED DYC DESIGN

The proposed design, as a direct yaw moment control system, is based on independently generating different torque commands to the two driving motors. Different motor torques are intuitively expected to generate different longitudinal tire forces on the driving wheels to produce a yaw moment. In this section, using the vehicle control model obtained in section 4.2, an equation showing a direct relationship between the steady-state yaw rate and the torque difference between the left and right driving motors is derived. Based on this mathematical relationship, a yaw rate-based DYC system is proposed to achieve the ideal steer characteristic, neutral steer.

With a DYC system on-board, there can be a difference between the longitudinal tire forces of the two rear driving wheels. Denoting this difference by $\Delta F_x = F_{x3} - F_{x4}$, it can be seen that the effect of ΔF_x is equivalent to an additional moment $\Delta M = \Delta F_x \times d/2$ applied on the rear axle plus a force ΔF_x exerted at the center of the rear axle, as illustrated in Figure 4.1. Thus, in presence of the difference between the tire forces, only equation (4.33) needs to be modified as follows:

$$c_\beta \beta + c_r r + c_\phi \phi + c_\delta \delta + \frac{d_{\mathrm{r}}}{2} \cdot \Delta F_x = I_z \dot{r} - I_{xz} \dot{p}. \qquad (4.34)$$
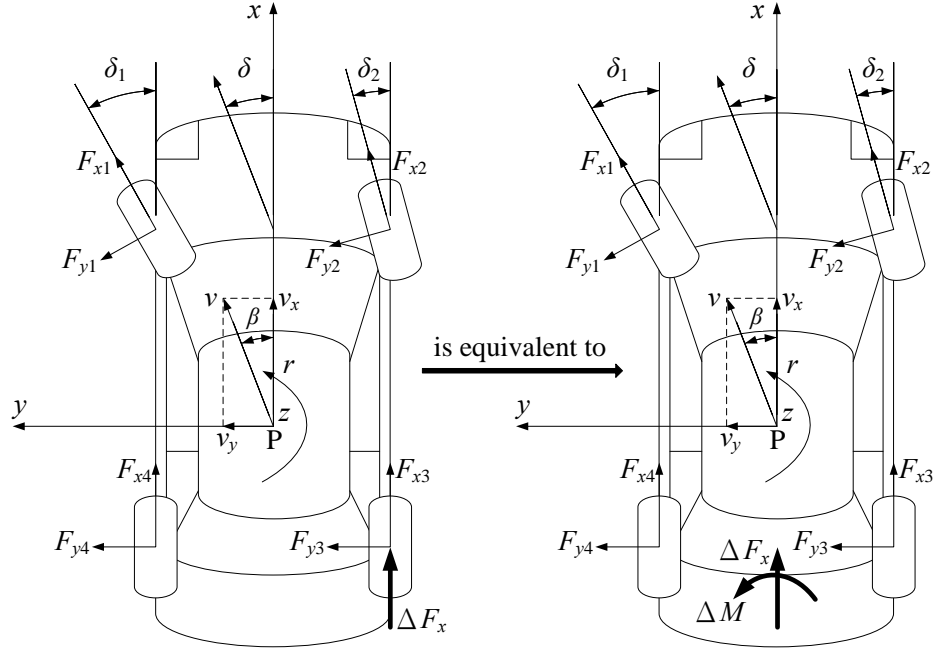
FIGURE 4.1: Force system acting on the vehicle.

Note that the dynamics of the vehicle (its lateral, roll and yaw dynamics) is substantially slower than the dynamics of the electric motors. Therefore, in the context of control command generation (torque commands sent to the motors for generating particular values of torques), the time-derivative terms in the equations of motion are negligible and can be discarded. Hence, for the purpose of controlling the driving motors, the following steady-state forms of the equations of motion can be safely used:

$$a_\beta \beta + a_r r + a_\phi \phi + a_\delta \delta = m v_x r \tag{4.35}$$

$$b_\phi \phi = -m_\mathrm{S} h_\mathrm{S} v_x r \tag{4.36}$$

$$c_\beta \beta + c_r r + c_\phi \phi + c_\delta \delta + \frac{d_\mathrm{r}}{2} \cdot \Delta F_x = 0. \tag{4.37}$$

Rewriting equations (4.35)–(4.37) in matrix form gives:

$$\begin{bmatrix} a_\beta & a_r - m v_x & a_\phi \\ 0 & m_\mathrm{S} h_\mathrm{S} v_x & b_\phi \\ c_\beta & c_r & c_\phi \end{bmatrix} \begin{bmatrix} \beta \\ r \\ \phi \end{bmatrix} = \begin{bmatrix} -a_\delta & 0 \\ 0 & 0 \\ -c_\delta & -\dfrac{d_\mathrm{r}}{2} \end{bmatrix} \begin{bmatrix} \delta \\ \Delta F_x \end{bmatrix}. \tag{4.38}$$

Solving the above system of equations for r, the following yaw rate response is derived in terms of the control inputs δ and ΔF_x:

$$r = \frac{Z_1}{Z_0} \delta + \frac{Z_2}{Z_0} \Delta F_x, \tag{4.39}$$

where,

$$Z_0 = a_\beta b_\phi c_r - a_r b_\phi c_\beta + b_\phi c_\beta m v_x - a_\beta c_\phi m_S h_S v_x + a_\phi c_\beta m_S h_S v_x \tag{4.40}$$

$$Z_1 = b_\phi(a_\delta c_\beta - a_\beta c_\delta) \tag{4.41}$$

$$Z_2 = -\frac{1}{2} a_\beta b_\phi d_r. \tag{4.42}$$

Equation (4.39) shows a direct relationship between the steady-state yaw rate and the longitudinal tire force difference ΔF_x.

As mentioned earlier, compared to the dynamics of the electric motors, the dynamics of the mechanical parts is very slow. Particularly, during each sampling time of the electronic control system, the variation of the wheel angular velocity is negligible. Besides, the tire pneumatic trail is normally quite small. Thus, neglecting the wheel angular acceleration and the tire pneumatic trail simplifies equation (3.73) to:

$$T = F_x R. \tag{4.43}$$

This shows that the longitudinal tire forces (and their difference) can be directly controlled by tuning the torque commands sent to the driving motors.

Substituting equation (4.43) in equation (4.39) leads to:

$$r = \frac{Z_1}{Z_0}\delta + \frac{Z_2}{Z_0 R}\Delta T. \tag{4.44}$$

Equation (4.44) clearly demonstrates a direct relationship between the steady-state yaw rate and the difference between the two motor torques, ΔT. This implies that by controlling the two motor torques, the vehicle steady-state yaw rate can be tuned to attain its desired value.

To calculate the desired yaw rate, the main criterion for neutral steer behavior is considered: the vehicle's instantaneous turning radius should not change with speed, as introduced in section 2.3. Kinematically, the turning radius is known as $L = v/r$, where v is the vehicle velocity at point P, as shown in Figure 1.4. Because the lateral component of v is considerably smaller than its longitudinal component v_x, so the tuning radius can be approximated by $L = v_x/r$.

Replacing v_x with rL in the numerator of the fraction in equation (2.5), and solving for L lead to:

$$L = \frac{l(1 + K v_x^2)}{\delta}. \tag{4.45}$$

For L to be invariant with v_x, the $Kv_x{}^2$ term needs to vanish. Hence, the desired yaw rate of a neutral steer vehicle is:

$$r^* = \frac{v_x}{l}\delta. \tag{4.46}$$

To calculate this desired yaw rate, the front wheel steer angle δ is computed from the reading of a steering wheel angle sensor, and the longitudinal velocity v_x can be estimated using one of the methods proposed in [111].

It has already been shown in (4.44) that, with a DYC system on-board, the steady-state yaw rate is a function of the motor torque difference. According to (4.44), the controller should be designed to achieve the desired yaw rate r^* by creating a corresponding desired motor torque difference ΔT^*, namely:

$$r^* = \frac{Z_1}{Z_0}\delta + \frac{Z_2}{Z_0 R}\Delta T^*. \tag{4.47}$$

Subtracting equation (4.44) from equation (4.47), the following relationship expressed in terms of errors in ΔT and r is derived:

$$\Delta T^* - \Delta T = \frac{Z_0 R}{Z_2}(r^* - r). \tag{4.48}$$

Note that the proposed DYC system is a discrete control system. The output of the controller $\Delta T(k+1)$ at discrete time $k+1$, must be generated to make $r(k)$ approach $r(k)^*$ as soon as possible. Thus, the proposed control policy is to create $\Delta T(k+1) = \Delta T^*$ which leads to:

$$\Delta T(k+1) - \Delta T(k) = \frac{Z_0 R}{Z_2}(r(k)^* - r(k)). \tag{4.49}$$

Dividing both sides by the sampling time t_s provides:

$$\frac{\Delta T(k+1) - \Delta T(k)}{t_s} = \frac{Z_0 R}{Z_2 t_s}(r(k)^* - r(k)). \tag{4.50}$$

Since the sampling time t_s is very small, the left-hand side of equation (4.50) can be considered as the time-derivative of the torque difference ΔT. Therefore, integration of both sides of equation (4.50) in continuous time t yields:

$$\Delta T(t) = \frac{Z_0 R}{Z_2 t_s}\int_0^t e_r(\tau)\mathrm{d}\tau, \tag{4.51}$$

where,

$$e_r(\tau) = r(\tau)^* - r(\tau). \tag{4.52}$$

Equation (4.51) implies that the desired torque difference between the two driving motors can be attained by using a simple Integral (I) controller. As introduced in Chapter 3, a full vehicle model including the nonlinear vehicle equations of motion is programed in
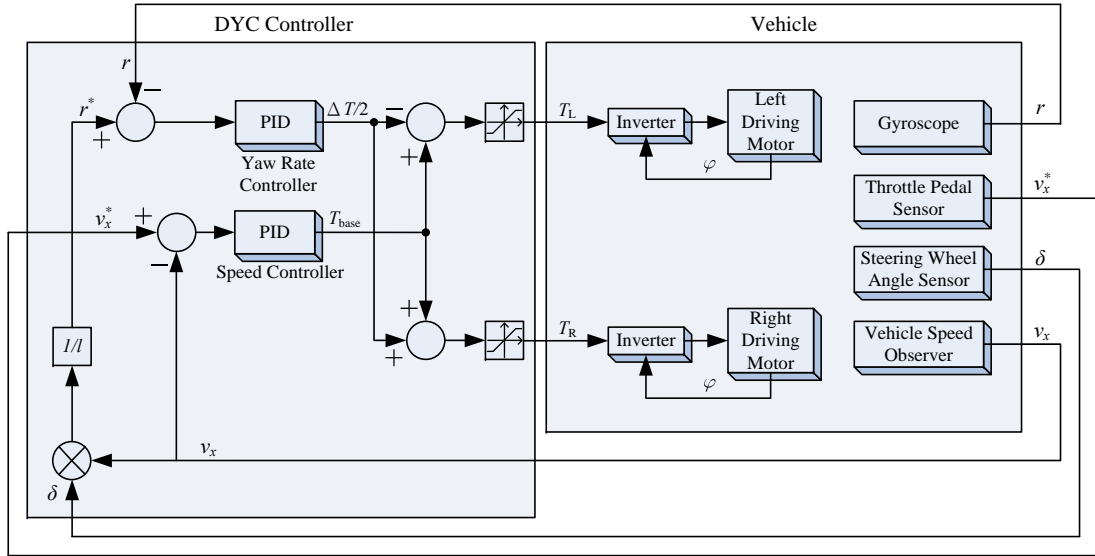
FIGURE 4.2: Schematic of the proposed DYC system.

the MATLAB/Simulink environment for simulation studies. However, a set of linearized and simplified equations of motion is utilized to achieve the above controller design. To accommodate the modeling errors and better regulate the yaw rate, a Proportional-Integral-Derivative (PID) controller is employed instead of just an I controller for the proposed yaw rate-based DYC system.

Figure 4.2 shows the schematic of the proposed DYC system. This DYC consists of two controller units. As explained earlier, the PID form yaw rate controller unit compares the actual yaw rate with the desired yaw rate computed from equation (4.46) and generates half the difference in the torque commands, $\Delta T/2$. The speed controller unit, also suggested in PID form, provides the base torque T_{base} which is the average of the two torque commands on the left and right sides, T_{L} and T_{R}. The base torque is tuned in such a way that the vehicle longitudinal velocity, v_x, follows the desired value v_x^* read from the throttle pedal sensor [108].

The parameters of both controllers can be easily tuned by trial-and-error. The outputs of the two controllers are subtracted and summed up to form the torque commands sent to the left and right inverters. The saturation blocks model the physical limits to the extent of torque the motors can generate. The two inverters convert torque commands to electric signals to drive the motors, using the feedback phase signal φ read from the motor encoders. Two PMBDCMs are selected as the driving motors, which allows both positive and negative torques to be generated. Several sensors are employed to measure the vehicle state r and the driver's commands v_x^* and δ (see Figure 4.2). As mentioned previously, v_x is estimated using a state observer. These signals are fed back to form the errors for the two PID controller units.

FIGURE 4.3: Third generation all-electric racing car developed at RMIT University.

4.4 SIMULATION RESULTS

A set of simulations are conducted in the MATLAB/Simulink environment to verify the effectiveness of the proposed DYC design and compare the steering performances between the competing methods. A full vehicle model established in Chapter 3 is employed for simulation studies. The vehicle parameters used in the simulations are from a real electric racing car built at RMIT University as shown in Figure 4.3. This car is the third generation of electric racing cars designed and developed by the students, equipped with two independent driving motors for rear wheels. The vehicle parameters are listed in Table 4.1. As the university is a member of the Formula SAE Tire Test Consortium (TTC), the real tire testing data obtained from TTC are employed in the *Magic Formula* for the tire force calculations in the simulations [112]. It has been pointed out in section 4.2 that in order to reveal the fundamental lateral and yaw behaviors, the vehicle longitudinal velocity v_x is normally maintained constant in the analysis. Thus, in the simulations v_x is maintained at 16 m/s using T_{base} produced by the speed controller unit.

As mentioned previously, the proposed method is compared with several typical types of control solutions introduced in Chapter 2. These solutions are the equal torque methods, Ackerman methods and yaw rate-based methods that employ equation (2.5) with a positive K as the reference yaw rate (in the following these methods are referred to as the conventional methods for brevity). The simulation studies comprise two groups: case studies with step steering inputs and case studies with sinusoidal steering inputs. In each group, the steering performance of a fully simulated vehicle in response to the

TABLE 4.1: Vehicle parameters of the electric racing car.

Parameter	Symbol	Value
Vehicle total mass	m	318 kg
Sprung mass	m_{S}	283 kg
Front track	d_{f}	1.144 m
Rear track	d_{r}	1.153 m
Wheel base	l	1.55 m
Distance	l_{f}	0.785 m
Distance	l_{r}	0.765 m
Distance	h_{S}	0.048 m
Mass center height	h	0.26 m
Front roll center height	h_{f}	0.218 m
Rear roll center height	h_{r}	0.218 m
Roll moment of inertia	I_x	200 kg m^2
Yaw moment of inertia	I_z	1000 kg m^2
Front suspension roll stiffness	$K_{\phi\mathrm{f}}$	25750 Nm/rad
Rear suspension roll stiffness	$K_{\phi\mathrm{r}}$	25750 Nm/rad
Total roll stiffness	K_ϕ	51500 Nm/rad
Front suspension roll damping	$C_{\phi\mathrm{f}}$	1953 N m s
Rear suspension roll damping	$C_{\phi\mathrm{r}}$	1875 N m s
Total roll damping	C_ϕ	3828 N m s
Tire radius	R	0.218 m
Inertia of wheel assembly	J	2 kg m^2
Motor peak power	$P_{\max}$	30 kw

step/sinusoidal steering inputs with various magnitudes and frequencies (for sinusoidal inputs) is examined.

The performance of each DYC scheme can be evaluated in terms of several criteria. The first important criterion is the capability of tracking the desired yaw rate expressed by equation (4.46) which corresponds to the ideal steer characteristic, neutral steer. Secondly, vehicle paths are taken into consideration. These paths demonstrate how close the vehicle is to the desired track, and they also act as a complement to the first criterion. Lastly, the wheel slip ratio and the corresponding longitudinal tire force of the inner driving wheel are assessed, in order to check if the DYC system causes any instability or excessive tire wear.

4.4.1 Simulations with step inputs

In this group of simulations, step inputs are used as the steering inputs in different rounds to verify the effectiveness of the proposed method. In each round, the same value of step input is applied to all competing control methods, but the value is varied between different rounds. A large range of possible step magnitudes have been examined. To avoid prolixity, here only the results for the step inputs $\delta = 0.1$ rad, $\delta = 0.075$ rad
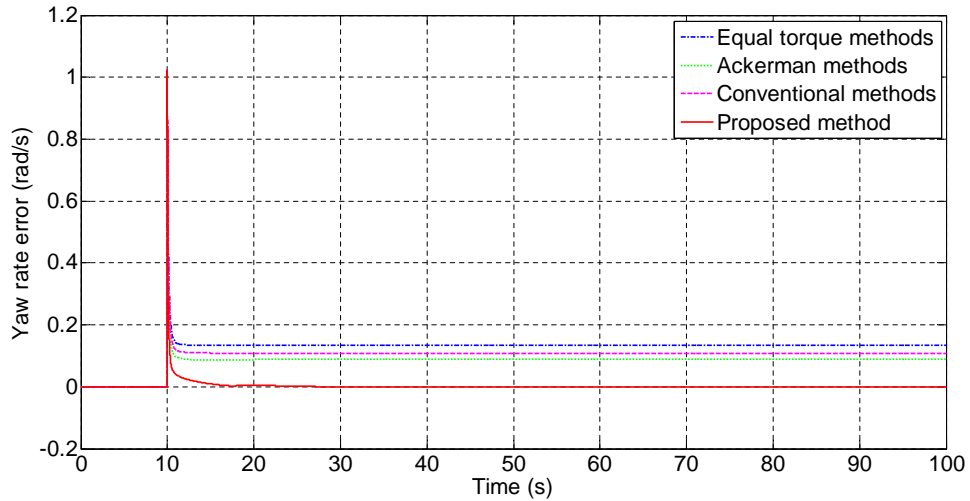
FIGURE 4.4: Yaw rate error responses to the step input $\delta = 0.1$ rad.

and $\delta = 0.05$ rad are presented in three different rounds. In order to clearly show the transients, all step steering commands occur at $t = 10$ s.

4.4.1.1 Step input $\delta = 0.1$ rad

As is seen in Figure 4.4, the yaw rate errors of all competing DYC methods converge to a non-zero value after a period of time, and only the proposed control method has been able to bring the yaw rate error to zero. In other words, in steady state, only with the proposed method on-board does the vehicle achieve neutral steer. As expected, the equal torque methods perform the worst, as they always output the same torque commands to the driving motors and emulate the behavior of an open differential. A pulse is observed at $t = 10$ s for all these four curves. This happens because the slope of the step input at $t = 10$ s is infinity and all methods need time to converge. At $t = 10$ s, all methods have the same yaw rate error of slightly over 1 rad/s, but this error fades out very quickly.

The vehicle paths using the aforesaid four types of DYC algorithms, during the first 12.5 s of simulation, are plotted in Figure 4.5. It is evident that the path traversed with the proposed DYC on-board is the closest to the desired vehicle track, which is consistent with the yaw rate errors shown in Figure 4.4.

Figure 4.6 shows the wheel slip ratio responses of the inner driving wheel using different control methods. The inner driving wheel normally presents the worst wheel slip because it is considerably unloaded by the centrifugal force during cornering. The wheel slip ratios of the equal torque methods and the conventional methods are both positive, while those of the Ackerman methods and the proposed method are negative. Moreover,
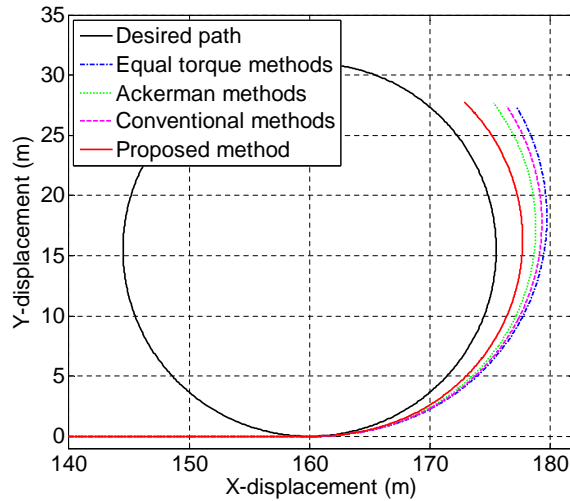
FIGURE 4.5: Vehicle path responses to the step input $\delta = 0.1$ rad during the first 12.5 s of simulation.
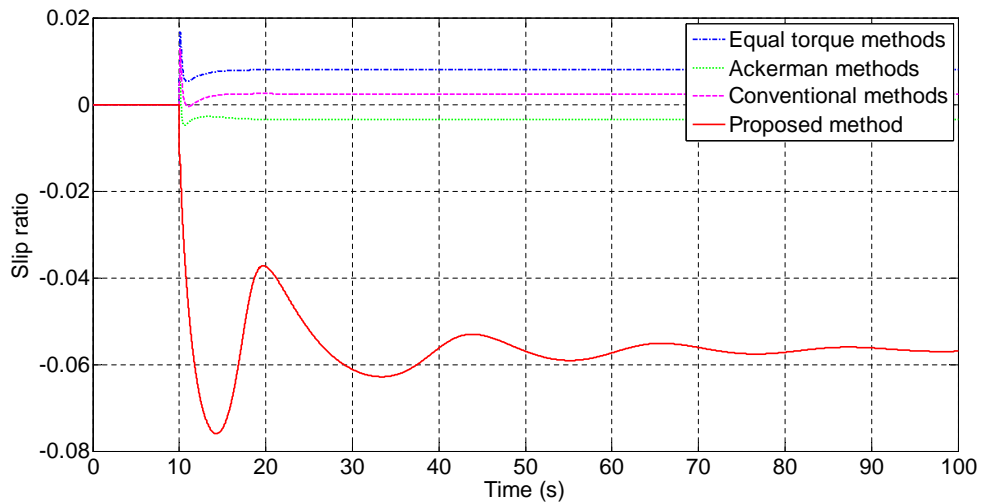
FIGURE 4.6: Wheel slip ratio responses of the inner driving wheel to the step input $\delta = 0.1$ rad.

the wheel slip ratios of all other three types of methods are very small in absolute value, compared to that of the proposed method. These results indicate that the longitudinal tire forces generated by the equal torque methods and the conventional methods are positive (forward) and small, and the force produced by the Ackerman methods is negative (backward) and small. Only with the proposed method on-board can a large (in absolute value) negative (backward) longitudinal tire force be generated to decrease the yaw rate error. This explanation is verified by Figure 4.7 in which the values of the longitudinal tire forces generated on the inner driving wheel by different methods are clearly plotted. In fact, the about 6% (absolute value) wheel slip ratio exhibited by the proposed method is normally an optimal value for most tires, at which, sufficient longitudinal tire forces can be generated, and neither does this slip ratio jeopardize vehicle safety nor causes any excessive tire wear.
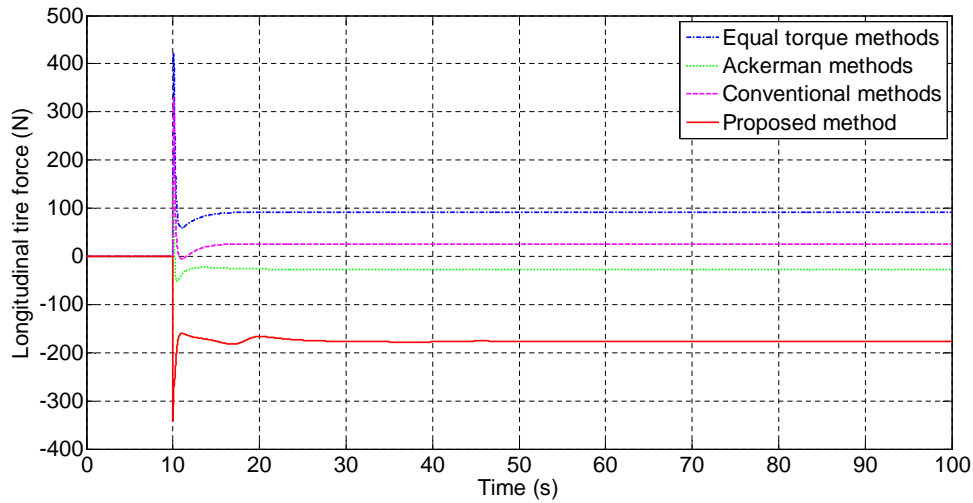
FIGURE 4.7: Longitudinal tire force responses of the inner driving wheel to step input $\delta = 0.1$ rad.
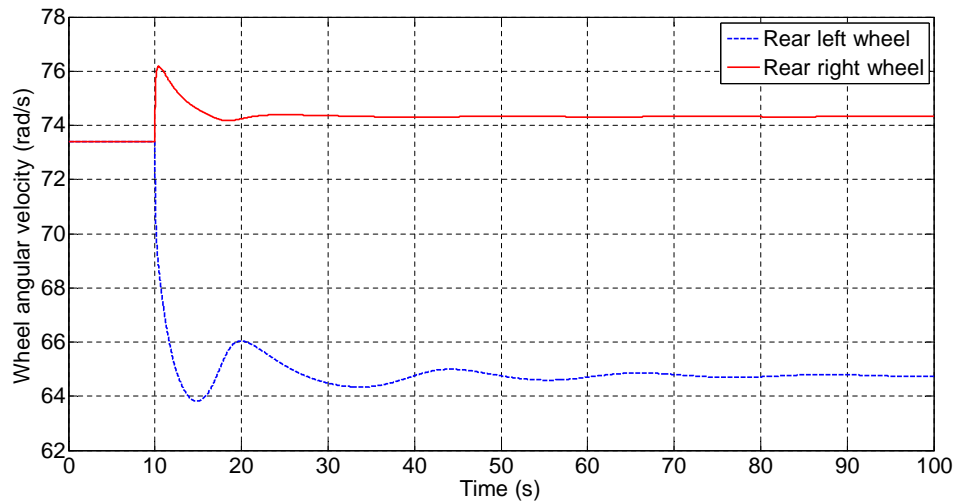
FIGURE 4.8: Wheel angular velocity responses of the two driving wheels to the step input $\delta = 0.1$ rad using the proposed DYC.

As mentioned before, with PMBDCMs, both positive and negative torques can be generated. When motors generate negative torques, they are actually working in the "electrical braking" mode [13]. It is observed in Figure 4.7 that the longitudinal tire force generated by the proposed method is negative, while the wheel angular velocity of the inner driving wheel seen from Figure 4.8 is positive. This means that the direction of the motor torque is opposite to the direction of the wheel angular velocity, namely the motor is operating in the "electrical braking" mode. Since the vehicle longitudinal velocity v_x is maintained by the speed controller unit that generates the base torque, v_x will not be decreased due to this "electrical braking" motion. Furthermore, in the "electrical braking" mode, regenerative braking can be made possible to enhance the efficiency of the driving system.
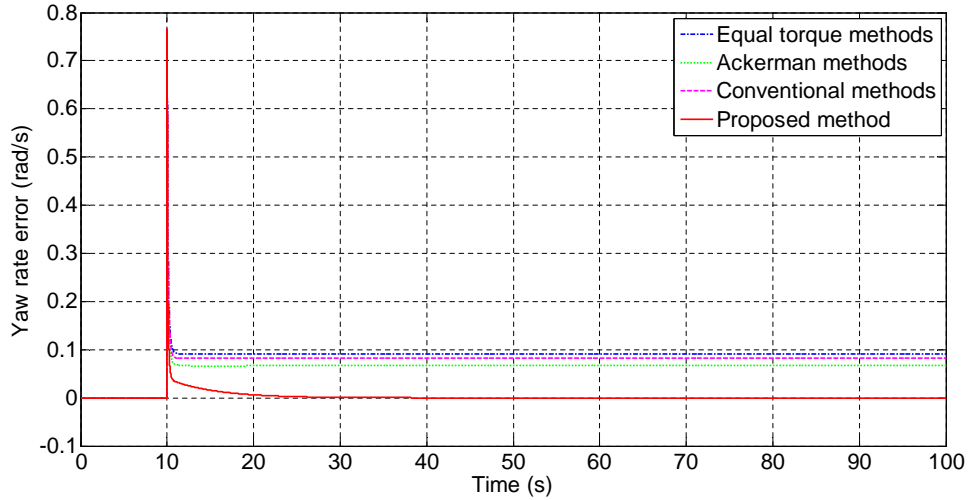
FIGURE 4.9: Yaw rate error responses to the step input $\delta = 0.075$ rad.
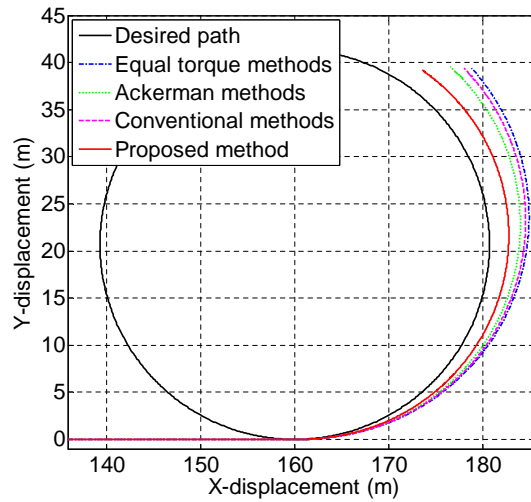
FIGURE 4.10: Vehicle path responses to the step input $\delta = 0.075$ rad during the first 13.5 s of simulation.

4.4.1.2 Step inputs $\delta = 0.075$ rad and $\delta = 0.05$ rad

The performances of the competing DYC methods with $\delta = 0.075$ rad and $\delta = 0.05$ rad are similar to those with $\delta = 0.1$ rad, as can be seen in Figures 4.9–4.12. The proposed method still brings the yaw rate error down to zero, and keeps the vehicle path the closest to the desired track. For brevity, the wheel slip ratio responses and the longitudinal tire force responses of the inner driving wheel for step input $\delta = 0.075$ rad and $\delta = 0.05$ rad are omitted, but it is worth emphasizing that they are similar to Figure 4.6 and Figure 4.7 and the responses agree with the aforesaid explanation.
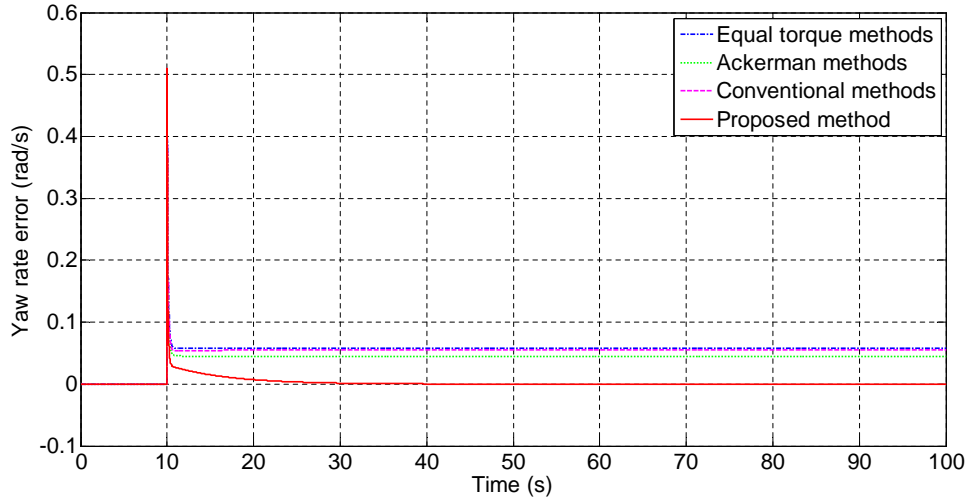
FIGURE 4.11: Yaw rate error responses to the step input $\delta = 0.05$ rad.
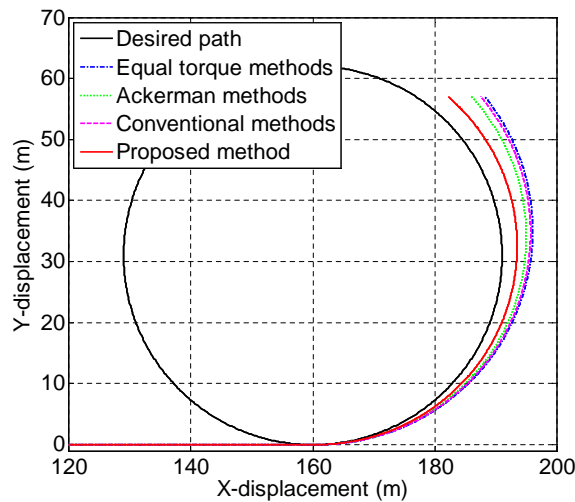
FIGURE 4.12: Vehicle path responses to the step input $\delta = 0.05$ rad during the first 15 s of simulation.

4.4.2 Simulations with sinusoidal inputs

In this group of simulations, sinusoidal signals are employed as the steering inputs to the system. Various combinations of magnitudes and frequencies for the steering commands have been examined. The results of four cases are presented here. To avoid prolixity, only the yaw rate tracking results are presented.

Figure 4.13 displays the yaw rate error responses to the sinusoidal steering input $\delta = 0.1 \sin \pi t$ rad. It is observed that the proposed DYC tracks the desirable yaw rate with errors considerably smaller than the competing methods. The error peak value produced by the proposed method is approximately 0.1 rad/s lower than the equal torque methods and 0.07 rad/s lower than the Ackerman methods. Similar superior performances of the proposed DYC can also be observed from the yaw rate error plots presented in
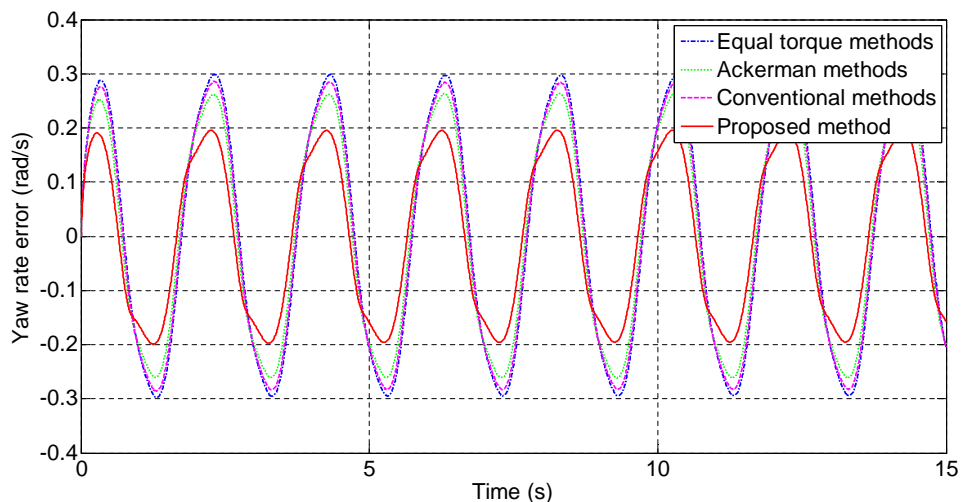
FIGURE 4.13: Yaw rate error responses to the sinusoidal input $\delta = 0.1 \sin \pi t$ rad.

Figure 4.14 (for the steering input $\delta = 0.1 \sin 0.5\pi t$ rad), Figure 4.15 (for the steering input $\delta = 0.05 \sin \pi t$ rad) and Figure 4.16 (for the steering input $\delta = 0.05 \sin 0.5\pi t$ rad). The observations from the above figures demonstrate that the proposed DYC solution is able to keep the vehicle much closer to neutral steer with the challenging sinusoidal steering inputs.

In short, the simulation results demonstrate that in response to sharp steering commands (in the form of large steps and large and fast sinusoids), the proposed method outperforms the competing methods in terms of the steering performance. More precisely, when applying step inputs with various magnitudes, the proposed DYC consistently drives the yaw rate to the desired value, and keeps the vehicle the closest to the desired path. Meanwhile, only small wheel slips (absolute values) occur on the inner driving wheel, which does not impair the stability of the vehicle maneuvers. When employing sinusoidal steering inputs with different combinations of amplitude and frequency, the proposed DYC shows the smallest yaw rate errors, thereby maintaining the car the closest to neutral steer.

4.5 SUMMARY

A neutral steer vehicle follows the driver's command accurately and enables the driver to accelerate in a corner without constantly adjusting the steering wheel. This capability greatly enhances the vehicle handling and is of special significance to high-performance vehicles. The typical types of control solutions (i.e. the equal torque methods, Ackerman methods and conventional methods) do not, by design, maintain a vehicle in neutral steer in various driving conditions. In this chapter, how neutral steer can be made possible
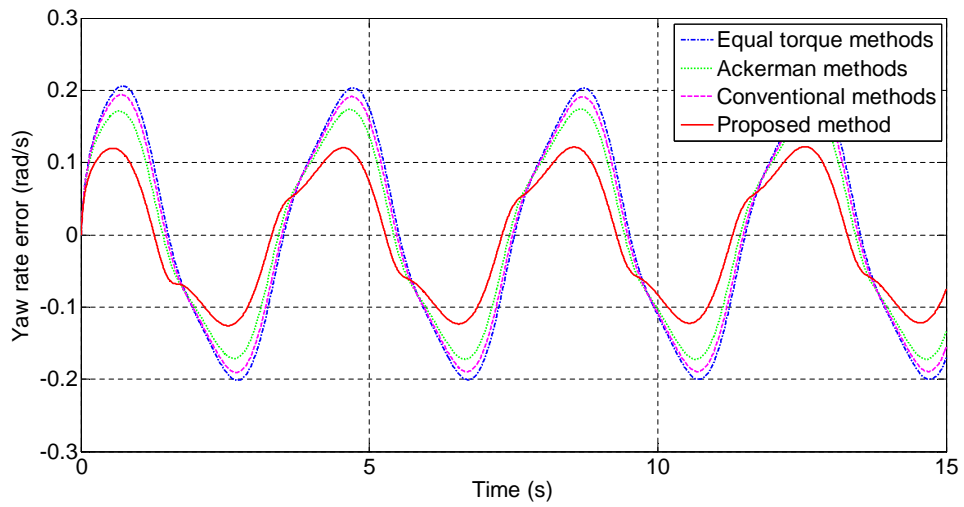
FIGURE 4.14: Yaw rate error responses to the sinusoidal input $\delta = 0.1 \sin 0.5\pi t$ rad.
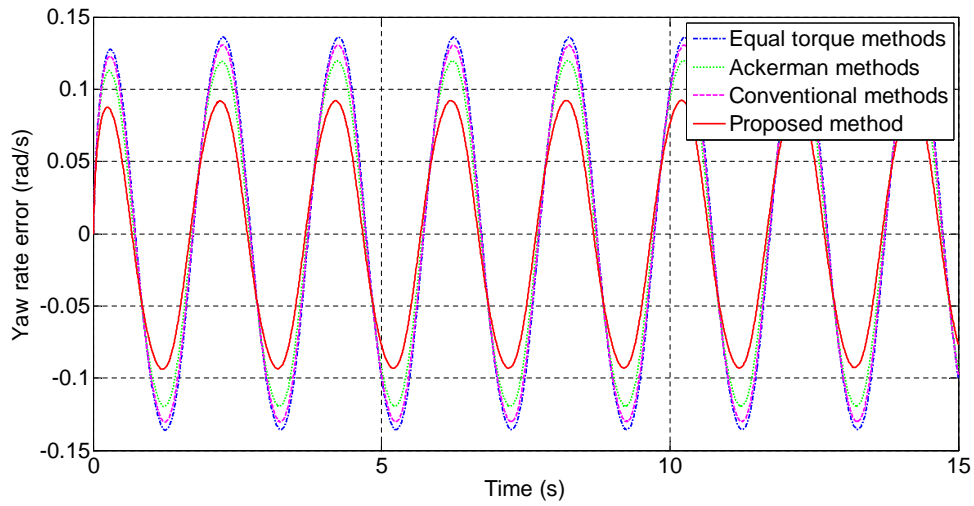
FIGURE 4.15: Yaw rate error responses to the sinusoidal input $\delta = 0.05 \sin \pi t$ rad.
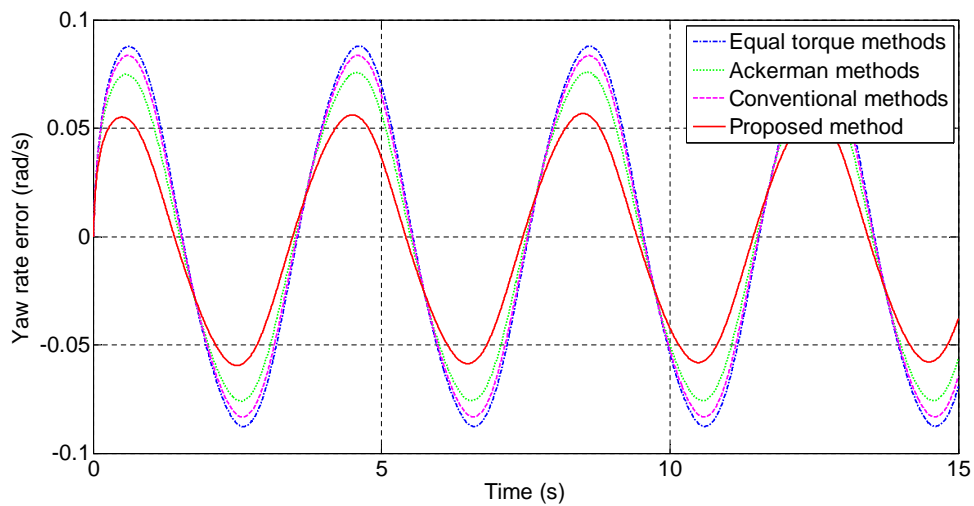
FIGURE 4.16: Yaw rate error responses to the sinusoidal input $\delta = 0.05 \sin 0.5\pi t$ rad.

for vehicles with independent motors using the proposed yaw rate-based DYC system has been mathematically and graphically demonstrated.

Simulation results manifest that with the challenging steering inputs, using the proposed DYC method, the vehicle closely tracks the desired yaw rate that corresponds to neutral steer, namely, a close-to-neutral steer characteristic is achieved. It is also shown in the simulations that in various challenging steering scenarios, the proposed DYC outperforms the competing control solutions in terms of tracking the desired yaw rate and desired vehicle path.

Chapter 5

Vehicle Side-Slip-Based Direct Yaw Moment Control

In this chapter, similar to Chapter 4, a mathematical relationship is derived from a set of simplified vehicle equations of motion. This relationship reveals that the steady-state vehicle side-slip directly depends on the torque difference between the left and right driving motors, therefore, it can be directly controlled by tuning this torque difference to track a reference value. On the basis of this relationship, a vehicle side-slip-based DYC solution is proposed to achieve zero vehicle side-slip. Simulation results manifest that the proposed DYC method keeps the vehicle side-slip close to zero in various challenging steering scenarios. Also, the proposed DYC solution outperforms two typical types of control schemes in terms of the vehicle side-slip responses.

5.1 BACKGROUND

As introduced in Chapter 1, the vehicle side-slip β is the angle between the vehicle heading direction (the positive direction of the x-axis in the vehicle local coordinate x-y-z) and the velocity vector $\boldsymbol{v}$ of the point P, as shown in Figure 1.4. The vehicle side-slip is also a crucial vehicle state which requires to be controlled. Ideally, it needs to be minimized, for two reasons: Firstly, due to the nonlinear tire characteristics, as the vehicle side-slip increases to large values, the tire cornering stiffnesses decrease and the yaw moment generated by the lateral tire forces descends [21]. When the vehicle side-slip is sufficiently large, the generated yaw moment becomes negligible and it can hardly be increased by changing the steer angle. As a result, the vehicle tends to lose its stability. Secondly, the vehicle side-slip is normally non-zero during cornering, and the driver intuitively assumes that the vehicle heading direction is the direction where the

vehicle is going. This wrong assumption can mislead the driver into performing excessive or insufficient steering actions. A small vehicle side-slip angle implies a consistency of the vehicle heading direction with the velocity vector $\boldsymbol{v}$, which provides the driver with superior sense of control during cornering [22].

In the following, a direct relationship between the steady-state vehicle side-slip and the motor torque difference is first derived from the same simplified vehicle equations of motion as in Chapter 4. Based on this relationship, a vehicle side-slip-based DYC method is then devised to maintain the vehicle side-slip magnitude as small as possible. Namely, the proposed DYC aims to maintain the vehicle heading direction consistent with the velocity vector $\boldsymbol{v}$. The merits of having small vehicle side-slip magnitude greatly enhance the vehicle stability and driver's sense of control. Besides, the proposed DYC maintains the wheel slip ratio of the inner driving wheel at low magnitudes so that excessive tire wear is prevented and the vehicle stability is further guaranteed.

The effectiveness of the proposed vehicle side-slip-based DYC is validated through simulation studies. Similar to Chapter 4, two typical types of control solutions, the equal torque methods and Ackerman methods, are employed for comparison purposes in the simulations.

5.2 VEHICLE SIDE-SLIP-BASED DYC DESIGN

5.2.1 Controller design

In Chapter 4, a vehicle control model, i.e., a set of linearized and simplified equations of motion was derived to achieve the yaw rate-based DYC scheme. In this chapter, the same control model is utilized again to derive the control law for the proposed vehicle side-slip-based DYC.

In steady state, the vehicle control model can be expressed by equation (4.38), which is rewritten as follows:

$$\begin{bmatrix} a_\beta & a_r - mv_x & a_\phi \\ 0 & m_S h_S v_x & b_\phi \\ c_\beta & c_r & c_\phi \end{bmatrix} \begin{bmatrix} \beta \\ r \\ \phi \end{bmatrix} = \begin{bmatrix} -a_\delta & 0 \\ 0 & 0 \\ -c_\delta & -\dfrac{d_r}{2} \end{bmatrix} \begin{bmatrix} \delta \\ \Delta F_x \end{bmatrix}. \tag{5.1}$$

In Chapter 4, the above equation was solved for the yaw rate r. Here, solving this equation for β leads to the following steady-state vehicle side-slip response in terms of

the control inputs δ and ΔF_x:

$$\beta = \frac{Z_3}{Z_0}\delta + \frac{Z_4}{Z_0}\Delta F_x, \tag{5.2}$$

where Z_0 remains the same as in Chapter 4 and

$$Z_3 = -a_\delta b_\phi c_r + a_r b_\phi c_\delta - b_\phi c_\delta m v_x + a_\delta c_\phi m_S h_S v_x - a_\phi c_\delta m_S h_S v_x \tag{5.3}$$

$$Z_4 = \frac{d_r}{2}(a_r b_\phi - b_\phi m v_x - a_\phi m_S h_S v_x). \tag{5.4}$$

Equation (5.2) shows that, similar to equation (4.39), the steady-state vehicle side-slip directly depends on the longitudinal tire force difference ΔF_x.

Substituting equation (4.43) in equation (5.2) leads to:

$$\beta = \frac{Z_3}{Z_0}\delta + \frac{Z_4}{Z_0 R}\Delta T. \tag{5.5}$$

Equation (5.5) clearly demonstrates a direct relationship between the steady-state vehicle side-slip and the difference between the two motor torques, ΔT. This implies that, by properly controlling the two motor torques, the steady-state vehicle side-slip can be tuned to attain its desired value.

According to equation (5.5), for a certain steer angle δ, the controller should be designed to achieve a desired vehicle side-slip β^* by creating a corresponding desired motor torque difference ΔT^*, namely:

$$\beta^* = \frac{Z_3}{Z_0}\delta + \frac{Z_4}{Z_0 R}\Delta T^*. \tag{5.6}$$

Equation (5.6) lays the theoretical foundation for the following controller design.

Subtracting equation (5.5) from equation (5.6) produces the following relationship expressed in terms of the errors in ΔT and β:

$$\Delta T^* - \Delta T = \frac{Z_0 R}{Z_4}(\beta^* - \beta). \tag{5.7}$$

Note that the proposed DYC system is a discrete control system. The output of the controller $\Delta T(k+1)$ at discrete time $k+1$, must be generated to make $\beta(k)$ approach $\beta(k)^*$ as soon as possible. Therefore, the proposed control strategy is to generate $\Delta T(k+1) = \Delta T^*$, which yields:

$$\Delta T(k+1) - \Delta T(k) = \frac{Z_0 R}{Z_4}(\beta(k)^* - \beta(k)). \tag{5.8}$$

Dividing both sides by the sampling time t_s leads to:

$$\frac{\Delta T(k+1) - \Delta T(k)}{t_s} = \frac{Z_0 R}{Z_4 t_s}(\beta(k)^* - \beta(k)). \tag{5.9}$$

The sampling time t_s of the control system is fairly short, so, the left-hand side of equation (5.9) can be considered as the time-derivative of the torque difference ΔT. Thus, integration of both sides of equation (5.9) in continuous time t provides:

$$\Delta T(t) = \frac{Z_0 R}{Z_4 t_s} \int_0^t e_\beta(\tau) d\tau, \tag{5.10}$$

where,

$$e_\beta(\tau) = \beta(\tau)^* - \beta(\tau). \tag{5.11}$$

As explained previously in section 5.1, the vehicle side-slip β should be minimized, which means $\beta(\tau)^* \equiv 0$. Thus equation (5.11) reduces to:

$$e_\beta(\tau) = -\beta(\tau). \tag{5.12}$$

Equation (5.10) indicates that the ideal torque difference between the two driving motors can be achieved by simply using an I controller. Similar to Chapter 4, the full vehicle model introduced in Chapter 3 with the nonlinear vehicle equations of motion is employed in the MATLAB/Simulink environment to produce the simulation results. However, a set of linearized and simplified equations of motion is adopted to achieve the above DYC design. To accommodate the modeling errors and better regulate the vehicle side-slip, a PID type controller, instead of a simple I controller, is chosen for the proposed vehicle side-slip-based DYC system.

5.2.2 Controller effect on yaw rate

Notice that the steady-state vehicle control model, equation (4.38), was solved in Chapter 4 to achieve the steady-state yaw rate response, equation (4.44). Again, the same equation is solved in this chapter to obtain the steady-state vehicle side-slip response, equation (5.5).

Equations (4.44) and (5.5) imply that when ΔT is tuned to obtain a certain steady-state vehicle side-slip, the steady-state yaw rate is also influenced, and vice versa. Therefore, when designing a DYC system to regulate the vehicle side-slip, the control parameters have to be carefully tuned in such a way that not only is a satisfactory vehicle side-slip performance achieved, but also the yaw rate performance is not compromised. This tuning involves appropriate trade-off between the vehicle side-slip and yaw rate responses.

This issue will be revisited in Chapter 6 where a sliding mode controller is proposed to tune the above-mentioned balance systematically using a user-defined control parameter.

5.2.3 Complete control structure

Figure 5.1 shows the structure of the proposed vehicle side-slip-based DYC design. This DYC system consists of two PID type controller units. The side-slip controller unit generates half the difference in the torque commands, $\Delta T/2$, from the vehicle side-slip error (the difference between the desired vehicle side-slip and its actual value), and the speed controller unit provides the base torque T_{base} which is the average of the two torque commands. The base torque is tuned in such a way that the vehicle longitudinal velocity, v_x, follows the desired value v_x^* read from the throttle pedal sensor [108]. In the simulations, the throttle pedal is held at a fixed position in order to keep v_x constant. The outputs of the two controllers are summed up and subtracted to form the left and right torque commands T_{L} and T_{R}. The two inverters receive these commands and convert them to electric signals, in conjunction with the feedback phase signal φ read from the motor encoders, to drive these two PMBDCMs.

The actual longitudinal velocity v_x and vehicle side-slip β can hardly be measured physically by any sensors at low cost and they need to be estimated by vehicle state observers. In the same way as Chapter 4, v_x can be estimated using one of the methods proposed in [111]. As for β, many vehicle side-slip estimation methods have been proposed in the literature such as [70, 71, 113, 114] which can be readily employed in the proposed DYC design. The actual and desired longitudinal velocities v_x and v_x^*, as well as the actual vehicle side-slip β are fed back to form the errors for the two PID controller units.

5.3 SIMULATION RESULTS

In order to verify the effectiveness of the proposed control scheme, a number of simulations have been conducted. The same MATLAB/Simulink model used in Chapter 4 is employed in this chapter as well for the simulation studies. The vehicle parameters used in the simulations are the same as those used in Chapter 4, as shown in Table 4.1. In all simulations, the initial vehicle longitudinal velocity v_x is chosen as 15 m/s (54 km/h) and is maintained constant by the speed controller unit.

In the following simulation analysis, the proposed DYC method is compared with two typical types of control schemes: the equal torque methods and Ackerman methods. The simulation studies comprise two groups: simulations with step steering inputs and
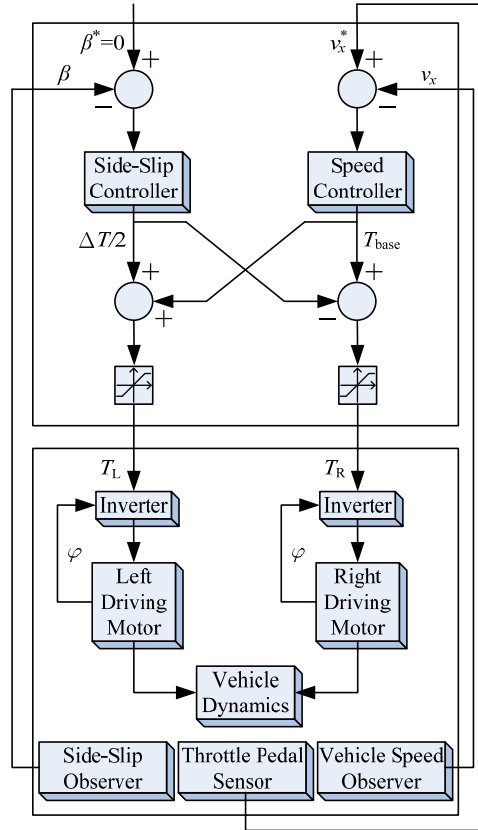
FIGURE 5.1: Schematic of the proposed DYC system.

simulations with sinusoidal steering inputs. In each group, the vehicle side-slip performances produced by the competing systems are examined. The yaw rate responses are also evaluated to investigate the effect of the controller on the yaw dynamics. Besides, the wheel slip ratio responses of the inner-driving wheel (which normally presents the worst wheel slip among the four wheels) are assessed as well in each simulation study.

5.3.1 Simulations with step inputs

In this group of simulation studies, step inputs are employed as the steering inputs to the simulated vehicle. A large range of possible step magnitudes have been examined. For the sake of brevity, here only the simulation results for step inputs $\delta = 0.1$ rad and $\delta = 0.12$ rad are presented. With a longitudinal velocity of 15 m/s, the two selected steering inputs represent rather challenging cornering scenarios. To clearly show the transients, in the simulations all step steering commands occur at $t = 10$ s.

Figure 5.2 shows the vehicle side-slip responses versus time with the three types of control solutions on-board, when the steering input is $\delta = 0.1$ rad. It is observed that all three response curves converge to some steady-state values very quickly after the steering input occurs, but the steady-state value of the proposed DYC is smaller than
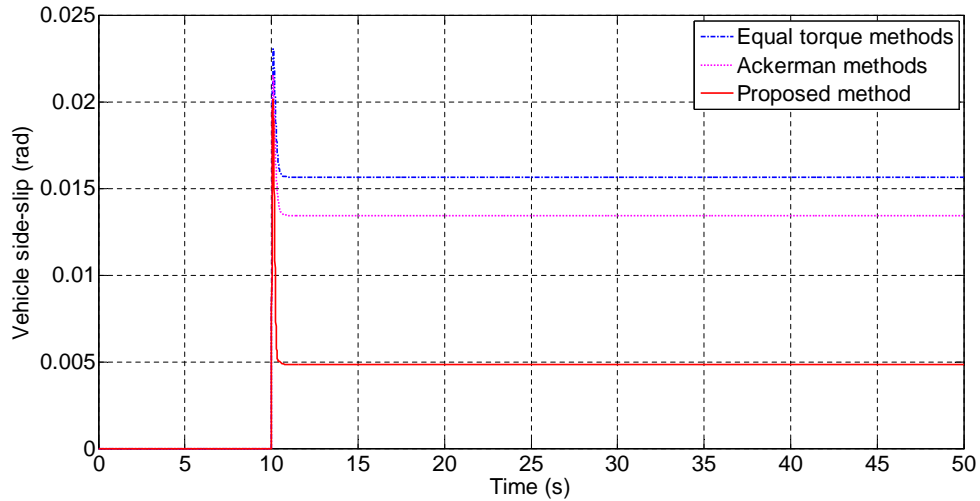
FIGURE 5.2: Vehicle side-slip responses to the step input $\delta = 0.1$ rad.

the other two. Indeed, using the proposed method, a steady-state vehicle side-slip of about 0.005 rad is gained, while with the equal torque methods and Ackerman methods on-board, the vehicle side-slips increase to about 0.0135 rad and 0.016 rad, respectively. The simulated vehicle presents the smallest vehicle side-slip with the proposed DYC on-board. In other words, the vehicle heading direction is closer to the velocity vector $\boldsymbol{v}$ of point P, and the driver can handle the vehicle more stably with superior sense of control.

As explained in section 5.2.2, along with the suppression of the vehicle side-slip, the vehicle's yaw rate is also influenced by the DYC system. This interplay necessitates the trade-off between the vehicle side-slip and yaw rate responses. Thus, the parameters of the proposed controller are adjusted in such a way that not only is a highly satisfactory vehicle side-slip response achieved (not necessarily perfect zero side-slip, as shown in Figure 5.2), but also a good yaw rate response is obtained to improve the vehicle handling. Note that the attainment of both satisfactory vehicle side-slip and yaw rate responses is not always possible, because the adjustment of the control parameters are highly subject to the vehicle specifications and driving conditions such as the motor torque, tire cornering stiffness, yaw moment of inertia and vehicle speed.

It is shown in Figure 5.3 that the yaw rate of the vehicle with the proposed DYC on-board is almost the same as the ideal value, when $\delta = 0.1$ rad. However, the other two curves are much lower than the desired one, which means that the vehicle presents sluggish understeer characteristic. When designing a DYC system for high-performance vehicles, this benefit becomes more important because sports vehicles normally tend to have a neutral steer or even slight oversteer characteristic [16, 115] to enhance the cornering agility.
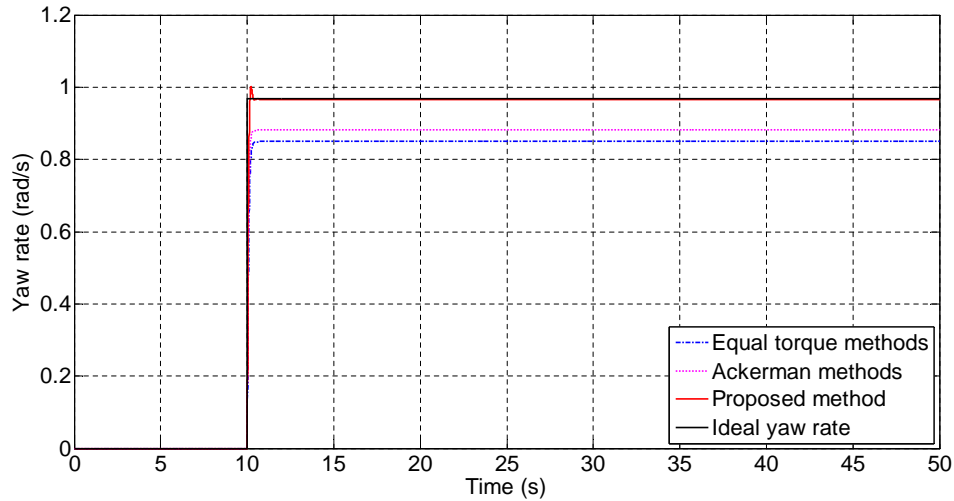
FIGURE 5.3: Yaw rate responses to the step input $\delta = 0.1$ rad.

Figure 5.4 shows the wheel slip ratio responses of the inner-driving (inner-rear) wheel with different control solutions on-board when $\delta = 0.1$ rad. The inner-driving wheel normally presents the worst wheel slip because it is considerably unloaded by the centrifugal force during cornering. In Figure 5.4, it can be seen that the wheel slip ratio value of the equal torque methods is always positive, while the wheel slip ratios of the other two are negative. Besides, the wheel slip ratio of the proposed method is larger than the competing methods in absolute value. These results indicate that the longitudinal tire force applied on the inner-driving wheel is positive (forward) and small with the equal torque methods on-board, and the tire force generated by the Ackerman methods is negative (backward) and small. However, using the proposed method, a large (in absolute value) negative (backward) longitudinal tire force is produced to decrease the vehicle side-slip and increase the yaw rate. This is verified by Figure 5.5 in which the longitudinal tire forces exerted on the inner-driving wheel are clearly plotted. It is crucial to notice that the wheel slip ratio with the proposed DYC on-board is still in a very safe range, even though its absolute value is larger than the other two. Neither does this slip ratio jeopardize vehicle safety nor causes any excessive tire wear.

As mentioned previously, with PMBDCMs on-board, both positive and negative torques can be generated. When motors generate negative torques, they are actually working in the "electrical braking" mode [13]. Similar to the case in Chapter 4, Figure 5.5 shows that the longitudinal tire force on the inner-driving wheel using the proposed DYC is negative, while the wheel angular velocity seen from Figure 5.6 is positive. This implies that the inner-driving motor is operating in the "electrical braking" mode. Because the vehicle longitudinal velocity v_x is maintained by the base torque T_{base} generated by the speed controller unit, so v_x will not be compromised due to this "electrical
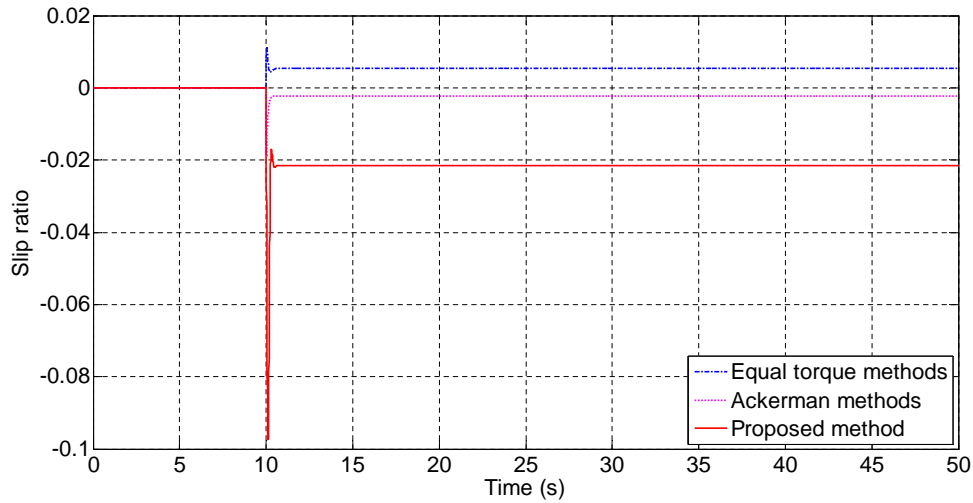
FIGURE 5.4: Wheel slip ratio responses of the inner-driving wheel to the step input $\delta = 0.1$ rad.
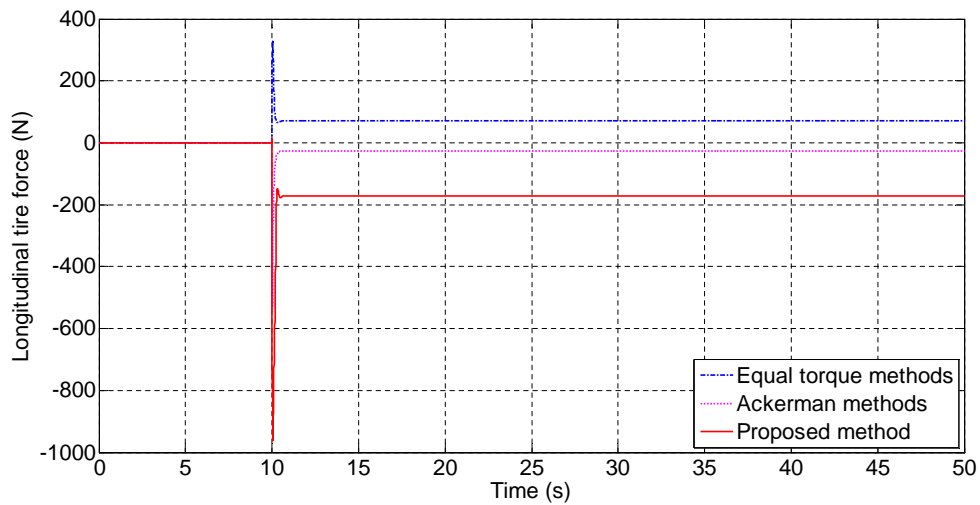
FIGURE 5.5: Longitudinal tire force responses of the inner-driving wheel to the step input $\delta = 0.1$ rad.

braking" motion. Also, in the "electrical braking" mode, regenerative braking can be made possible to enhance the efficiency of the driving system.

Figure 5.7 plots the vehicle side-slip responses of the competing control schemes when the step steering input is pushed up to a more challenging case, $\delta = 0.12$ rad. As shown in this figure, the proposed DYC outperforms the other two types of control methods in terms of providing the smallest vehicle side-slip. In steady state, the equal torque methods produce a vehicle side-slip value almost five times larger than the one given by the proposed method. The Ackerman methods lead the vehicle side-slip to diverge rapidly, and the simulated vehicle loses its stability very quickly.

Accordingly, the yaw rate response curves plotted in Figure 5.8 demonstrate similar trends. The yaw rate of the simulated vehicle with the proposed DYC on-board converges
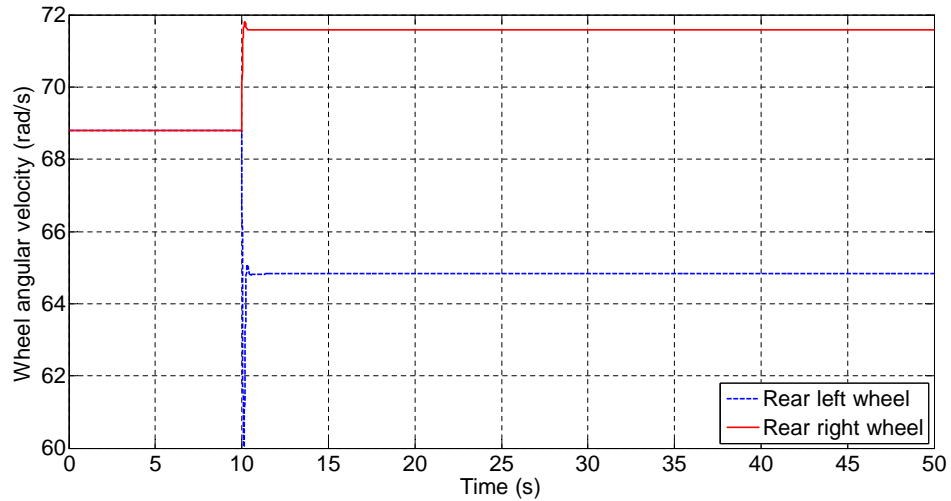
FIGURE 5.6: Wheel angular velocity responses of the two driving wheels to the step input $\delta = 0.1$ rad using the proposed DYC.
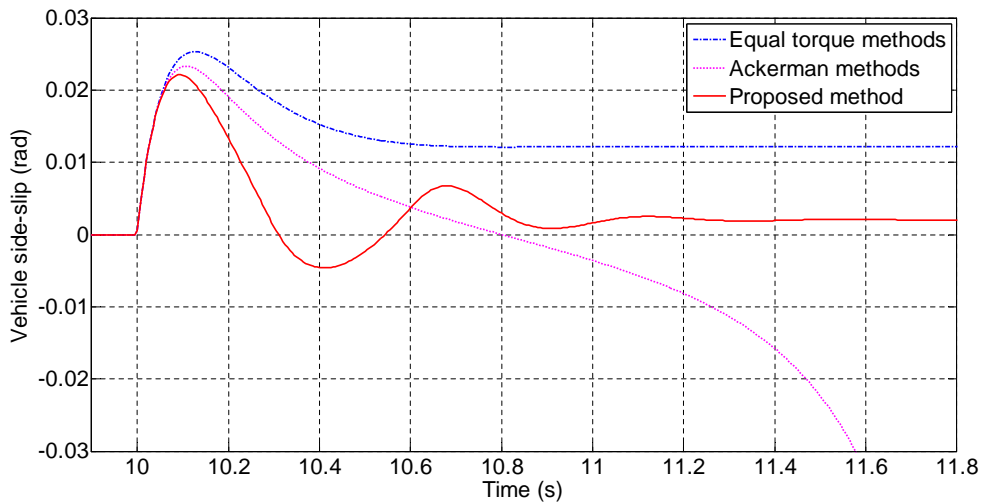
FIGURE 5.7: Vehicle side-slip responses to the step input $\delta = 0.12$ rad.

to a certain value after a short period of oscillation, and it is the closest one to the desired value among the three curves. The curve corresponding to the equal torque methods converges as well but it is further away from the ideal curve. Again, the yaw rate produced by the Ackerman methods diverges, which is consistent with the vehicle side-slip response shown in Figure 5.7.

Figure 5.9 shows the wheel slip ratio responses of the inner-driving wheel. Similarly, the wheel slip ratio diverges very quickly when applying the Ackerman methods, while the other two types of control schemes quickly stabilize the slip ratio. Although oscillation appears at the beginning of cornering with the proposed DYC on-board, the peak values of this oscillation (absolute value) are very small. Thus, this oscillation does not cause any instability or excessive tire wear.
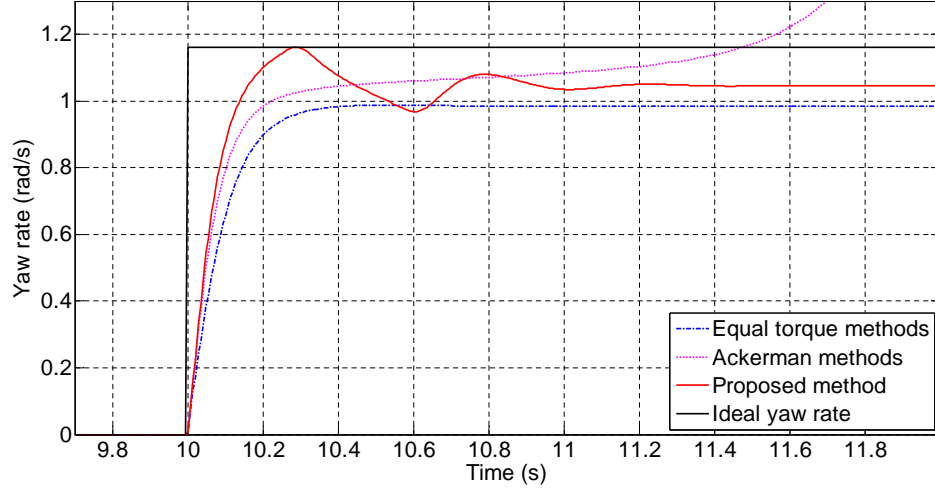
FIGURE 5.8: Yaw rate responses to the step input $\delta = 0.12$ rad.
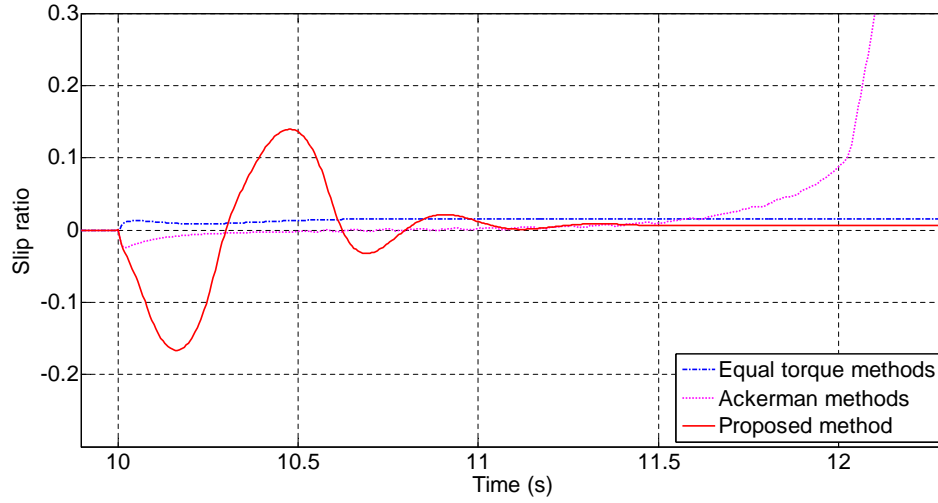
FIGURE 5.9: Wheel slip ratio responses of the inner-driving wheel to the step input $\delta = 0.12$ rad.

Table 5.1 presents the average errors of the vehicle side-slip and yaw rate for the steering input $\delta = 0.1$ rad. The average errors are defined as follows:

$$\bar{e}_\beta = \frac{1}{t_{\text{sim}}} \int_0^{t_{\text{sim}}} |e_\beta(t)|\, dt \tag{5.13}$$

$$\bar{e}_r = \frac{1}{t_{\text{sim}}} \int_0^{t_{\text{sim}}} |e_r(t)|\, dt, \tag{5.14}$$

where t_{sim} denotes the simulation time and,

$$e_\beta(t) = \beta(t)^* - \beta(t) = -\beta(t) \tag{5.15}$$

$$e_r(t) = r(t)^* - r(t). \tag{5.16}$$

As shown in this table, the average errors of the proposed DYC are remarkably lower than the errors of the competing methods. This quantitative comparison testifies the graphical

TABLE 5.1: Average errors of the vehicle side-slip and yaw rate.

	$\delta = 0.1$ rad		$\delta = 0.1 \sin \frac{\pi}{3} t$ rad	
	$\bar{e}_\beta$ (rad)	$\bar{e}_r$ (rad/s)	$\bar{e}_\beta$ (rad)	$\bar{e}_r$ (rad/s)
Equal Torque Methods	0.01255	0.09607	0.01231	0.07812
Ackerman Methods	0.01078	0.06999	0.01153	0.06089
Proposed Method	0.00392	0.00190	0.00662	0.03208
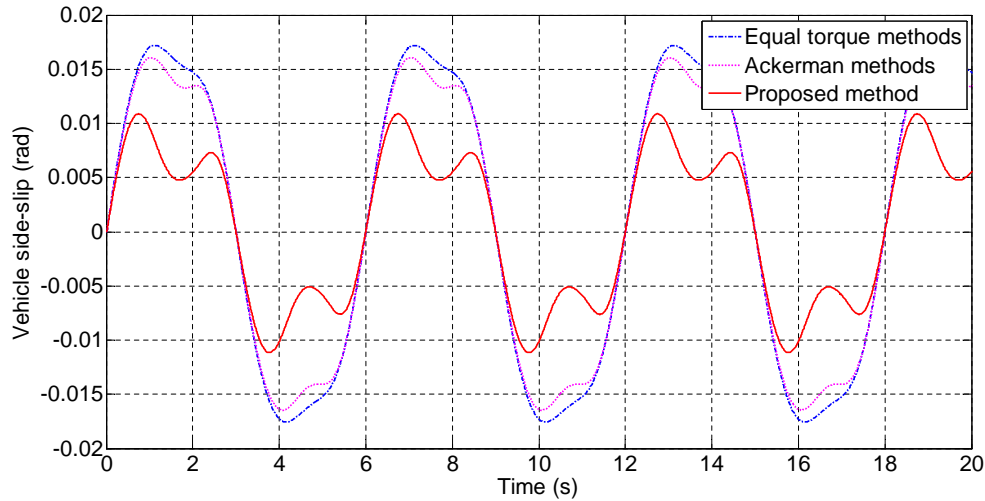
FIGURE 5.10: Vehicle side-slip responses to the sinusoidal input $\delta = 0.1 \sin \frac{\pi}{3} t$ rad.

simulation results shown in this section. The quantitative results for $\delta = 0.12$ rad are not presented since the errors of the Ackerman methods diverge.

5.3.2 Simulations with sinusoidal inputs

In this section, sinusoidal signals are utilized as the steering inputs to the system. First, the vehicle side-slip responses to a very intense sinusoidal steering input $\delta = 0.1 \sin \frac{\pi}{3} t$ rad are presented in Figure 5.10. With a steer ratio of, say 1:12, the steering column is turned from $-69°$ to $+69°$ then back to $-69°$ every 6 seconds at a vehicle speed of $v_x = 15$ m/s, which represents a highly challenging steering scenario. Figure 5.10 shows that the vehicle side-slip magnitude produced by the proposed DYC is consistently lower than the other two. Besides, it is seen in Figure 5.11 that the yaw rate curve of the proposed DYC is very close to the ideal curve while the other two curves are not. Figure 5.12 demonstrates that consistent with the step steering input situation, the wheel slip ratio of the proposed method is larger in magnitude but always within a very small and safe range.

Similarly, when the sinusoidal steering input is pushed up to an even more challenging case $\delta = 0.13 \sin \frac{\pi}{3} t$ rad, the Ackerman methods lead the vehicle states to diverge and
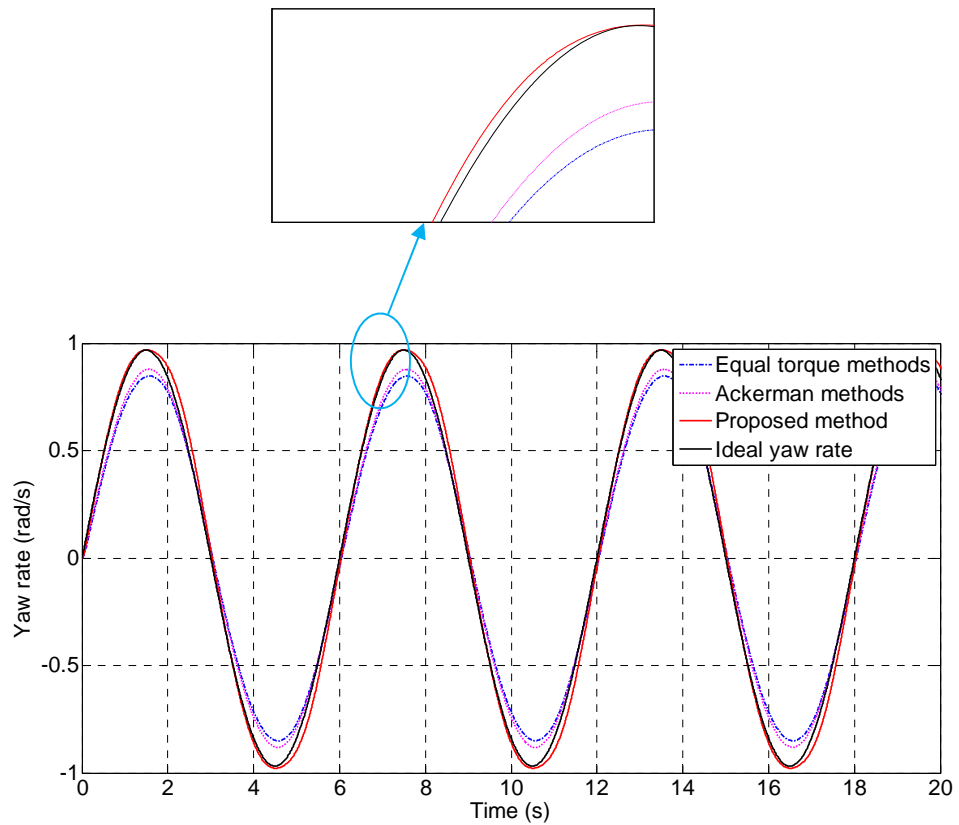
FIGURE 5.11: Yaw rate responses to the sinusoidal input $\delta = 0.1 \sin \frac{\pi}{3} t$ rad.
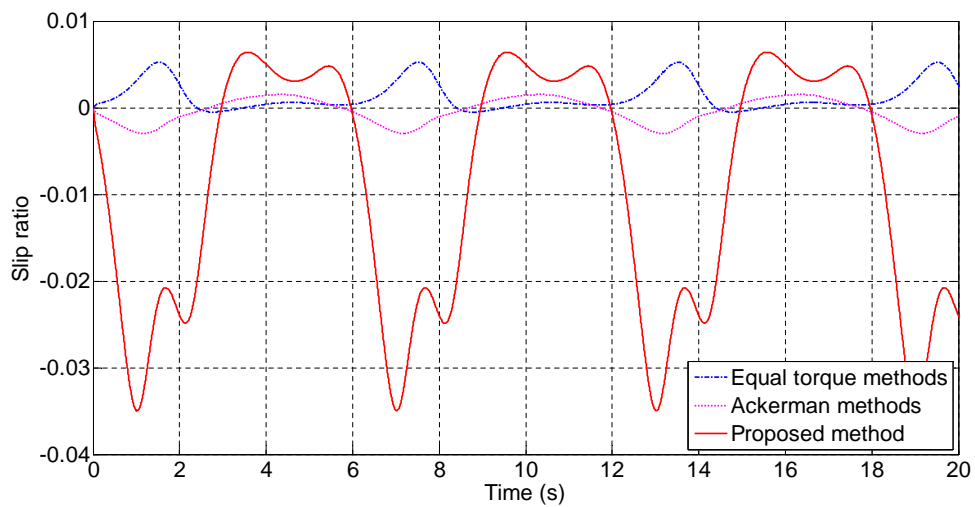
FIGURE 5.12: Wheel slip ratio responses of the inner-driving wheel to the sinusoidal input $\delta = 0.1 \sin \frac{\pi}{3} t$ rad.
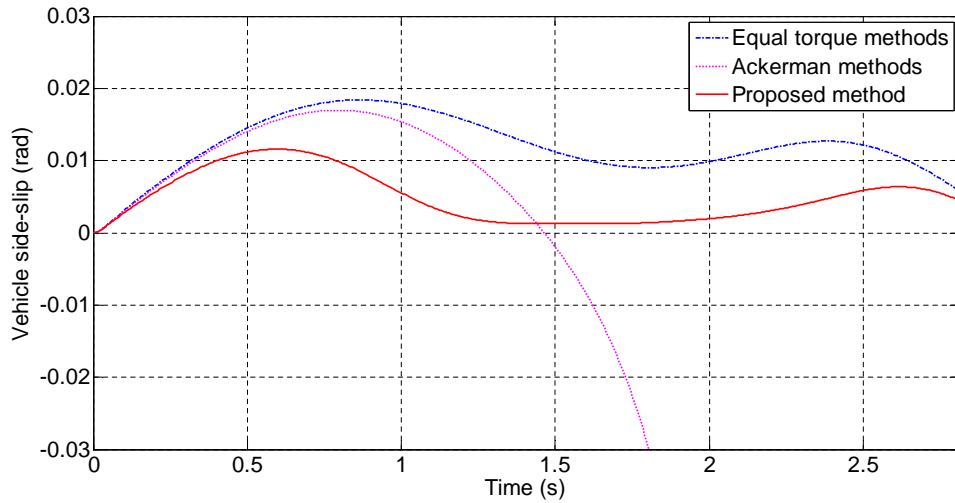
FIGURE 5.13: Vehicle side-slip responses to the sinusoidal input $\delta = 0.13 \sin \frac{\pi}{3} t$ rad.
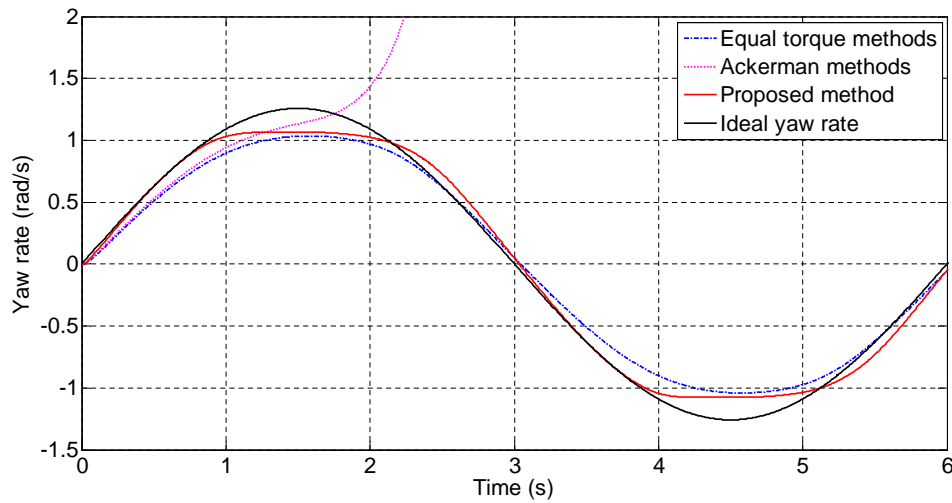
FIGURE 5.14: Yaw rate responses to the sinusoidal input $\delta = 0.13 \sin \frac{\pi}{3} t$ rad.

the vehicle loses its stability very quickly, as seen from Figures 5.13–5.15. But with the proposed DYC scheme on-board, the simulated vehicle is completely stable, and the vehicle side-slip and yaw rate responses still present themselves as the best among the three. The equal torque methods, as expected, present an intermediate performance.

Table 5.1 also presents the average errors of the vehicle side-slip and yaw rate for the steering input $\delta = 0.1 \sin \frac{\pi}{3} t$ rad. In this scenario, the average errors of the proposed DYC are greatly lower than the errors of the competing methods. The results for $\delta = 0.13 \sin \frac{\pi}{3} t$ rad are not presented in the table since the errors of the Ackerman methods diverge.

In short, the simulation results demonstrate that in response to challenging steering inputs (in the form of large steps and large and fast sinusoids), the proposed DYC outperforms the competing methods in terms of the vehicle side-slip and yaw rate responses.
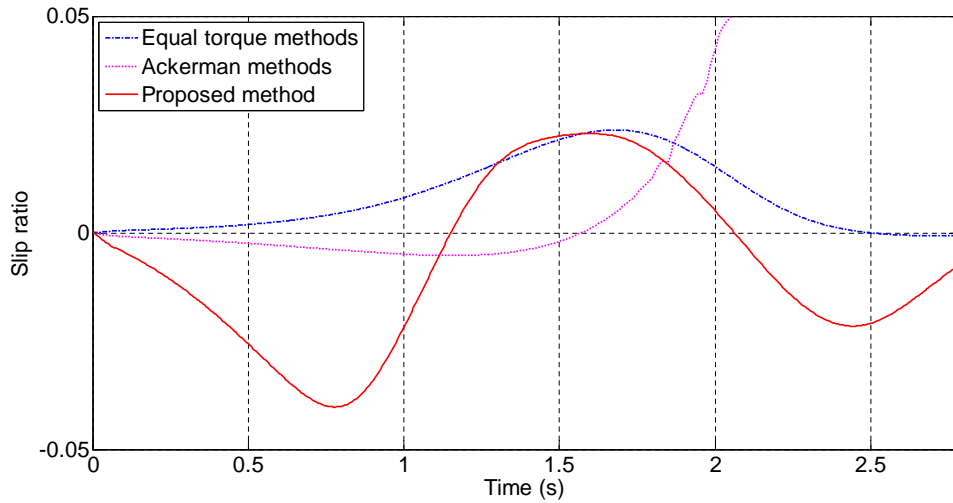
FIGURE 5.15: Wheel slip ratio responses of the inner-driving wheel to the sinusoidal input $\delta = 0.13 \sin \frac{\pi}{3} t$ rad.

More precisely, the proposed DYC solution maintains the vehicle side-slip very close to zero in both steering scenarios. Thus, the vehicle heading direction is kept very close to the vehicle velocity vector $\boldsymbol{v}$. In the simulated conditions, the yaw rate can be maintained close to the ideal level that corresponds to neutral steer, which phenomenon is subject to the vehicle specifications and driving conditions and is not always possible. The improvements in the vehicle side-slip and yaw rate responses increase the wheel slip ratio magnitude of the inner-driving wheel, but it still remains within a small and safe range.

5.4   SUMMARY

In this chapter, a mathematical relationship between the steady-state vehicle side-slip and the motor torque difference is demonstrated. Based on this mathematical derivation, a DYC scheme that minimizes the vehicle side-slip is designed. Simulation results show that in challenging steering scenarios, the proposed method outperforms two typical types of control schemes, the equal torque methods and Ackerman methods, in terms of the vehicle side-slip and yaw rate responses. The stability of the electric vehicle and driver's sense of control are effectively enhanced through the reduction of the vehicle side-slip. Meanwhile, the wheel slip ratio of the inner-driving wheel is maintained at low magnitudes, which further guarantees the vehicle stability and prevents excessive tire wear.

Chapter 6

Simultaneous Control of Yaw Rate and Vehicle Side-Slip

The potential problems of controlling one vehicle state only (either the yaw rate or vehicle side-slip) have been pointed out in section 2.5.1. To eliminate the potential downsides and combine the benefits of controlling the yaw rate and vehicle side-slip individually, numerous recent DYC designs adopt both states simultaneously as the control variables. In these works, the sliding mode control technique is commonly employed to generate the target yaw moment. This chapter proposes a new sliding mode-based DYC method for tracking both the desired yaw rate and vehicle side-slip. This DYC scheme employs a novel switching function, a linear combination of the normalized absolute values of the yaw rate and vehicle side-slip errors, to guarantee the simultaneous convergences of both vehicle states. Also, instead of the linearized and simplified vehicle control model, the complete nonlinear vehicle equations of motion established in Chapter 3 are employed in the control system design, which helps to construct a more effective control law. Comparative simulation results demonstrate that the proposed DYC design outperforms the competing methods in terms of tracking the reference yaw rate, vehicle path and vehicle side-slip in various challenging driving scenarios.

6.1 BACKGROUND

As shown in the preceding chapters, the yaw rate and vehicle side-slip present themselves as the fundamental states that govern the vehicle handling and stability. In Chapters 4 and 5, two DYC system for controlling the yaw rate or vehicle side-slip individually are proposed. However, the improvements in control performance by taking into account both vehicle states have not been discussed yet so far. In this chapter, a new sliding mode

control scheme is proposed to regulate the yaw rate and vehicle side-slip simultaneously, aiming at eliminating the imperfections and limitations of the existing sliding mode-based DYC systems.

A vehicle is a nonlinear system which undergoes various ambient disturbances. Besides, the vehicle models are never perfectly accurate and some model uncertainties are always present. Since the sliding mode control technique provides robustness against disturbances and uncertainties when controlling nonlinear systems [75–77], it is widely used in vehicle stability and handling control and has become the most popular control technique in the latest DYC solutions.

In the recent DYC solutions, the most common sliding mode control design employs a linear combination of the yaw rate and vehicle side-slip errors as the switching function which takes the following form [17, 23, 24, 78–81]:

$$s = r - r^* + \xi(\beta - \beta^*), \tag{6.1}$$

where r^* and β^* are the same desired (reference) yaw rate and vehicle side-slip as in Chapters 4 and 5, and ξ is a positive design parameter.

The above popular switching function presents two limitations. Firstly, in some certain circumstances, this switching function cannot guarantee simultaneous convergences of both errors to zero. In sliding mode control, the objective is to drive the system trajectories towards the sliding surface $s = 0$ and then maintain the trajectories on it. With the above switching function, if the yaw rate error $r - r^*$ and the vehicle side-slip error $\beta - \beta^*$ have the same sign, when the sliding surface $s = 0$ is reached, these two errors are guaranteed to vanish. However, since the signs of the errors may change in various driving conditions, $s = 0$ can also hold when one error is positive and the other is negative with the right ξ. As a result, the sliding mode controller may fail. This limitation is exposed in a simulation case study in Section 6.3 where the two errors present opposite signs and the common sliding mode controller using the above switching function produces inferior control performance to the competing methods. Secondly, the design parameter ξ, intuitively, is expected to represent the emphasis between the two error terms. However, the yaw rate error $r - r^*$ and the vehicle side-slip error $\beta - \beta^*$ have different dimensions. In order for the addition in equation (6.1) to be valid, the parameter ξ cannot be dimensionless. Thus, it cannot represent the emphasis between the two errors. These two limitations may jeopardize the robustness of DYC systems and bring about confusions in the course of DYC design.

Many existing DYC solutions (e.g. [23, 51, 66, 79]) are designed based on the well-known two DoF bicycle model [20] and/or linear tire model [116], which neglect the vehicle roll

motion and tire cornering stiffness nonlinearity, respectively. In high lateral acceleration scenarios, significant vehicle body roll and lateral load transfer lead to the change of tire cornering stiffnesses and in turn, vehicle dynamics. Thus, the bicycle model and linear tire model cannot accurately describe the vehicle responses in high lateral acceleration scenarios [116]. As a result, the control systems based on such models may produce unexpected vehicle responses [109].

In this chapter, the complete nonlinear vehicle equations of motion derived in Chapter 3 are used to devise a novel sliding mode DYC method. The proposed DYC scheme is designed based on a new switching function, a linear combination of the normalized absolute values of the yaw rate and vehicle side-slip errors, to eliminate the above-mentioned limitations with the commonly used switching function, equation (6.1). Extensive comparative simulations show that the proposed DYC solution outperforms the competing methods in terms of tracking the desired (reference) yaw rate, vehicle path and vehicle side-slip in different challenging driving scenarios.

6.2 PROPOSED DYC DESIGN

In this section, a DYC system based on sliding mode control is designed to track the desired yaw rate and vehicle side-slip simultaneously. The same desired (reference) yaw rate and vehicle side-slip used in Chapters 4 and 5 are employed, which are rewritten as follows:

$$r^* = \frac{v_x}{l}\delta \tag{6.2}$$

$$\beta^* = 0. \tag{6.3}$$

As mentioned in Chapter 4, δ is computed from the reading of a steering wheel angle sensor, and v_x can be estimated using one of the methods proposed in [111]. Note that these desired values can be altered according to the driver's preference, which does not change the basic properties of the proposed controller.

The control objective is to track the desired yaw rate and vehicle side-slip simultaneously. To achieve this goal by means of sliding mode control, one critical step is to appropriately design a switching function. In this design, instead of equation (6.1), a linear combination of the normalized absolute values of errors is proposed as the switching function:

$$s = \frac{\rho}{|\Delta r|_{\max}}|r - r^*| + \frac{1 - \rho}{|\Delta\beta|_{\max}}|\beta - \beta^*|, \tag{6.4}$$

where $\rho \in [0, 1]$ is a design parameter, and $|\Delta r|_{\max}$ and $|\Delta\beta|_{\max}$ are the maximum absolute values of the yaw rate error and vehicle side-slip error defined by the designer, respectively.

Due to the absolute values, the proposed switching function (6.4) becomes zero only when r converges to r^* and β converges to β^* simultaneously, regardless of the signs of the yaw rate and vehicle side-slip errors. Besides, the two error terms are normalized, so the design parameter ρ is dimensionless and it represents the emphasis on the yaw rate error (while $1 - \rho$ represents the emphasis on the vehicle side-slip error).

Since the target vehicle side-slip is zero, equation (6.4) reduces to:

$$s = \frac{\rho}{|\Delta r|_{\max}}|r - r^*| + \frac{1 - \rho}{|\beta|_{\max}}|\beta|, \tag{6.5}$$

and the derivative of the switching function (6.5) is given by:

$$\dot{s} = \frac{\rho}{|\Delta r|_{\max}}(\dot{r} - \dot{r}^*)\operatorname{sgn}(r - r^*) + \frac{1 - \rho}{|\beta|_{\max}}\dot{\beta}\operatorname{sgn}(\beta). \tag{6.6}$$

Following the fundamental principle in sliding mode control, to drive the system trajectories to the sliding surface $s = 0$, the following sliding condition should be satisfied [77]:

$$\frac{1}{2}\frac{d}{dt}s^2 = s\dot{s} \leqslant -\eta|s|, \tag{6.7}$$

where η is a strictly positive constant. Since outside the sliding surface, $s > 0$, the above condition simplifies to:

$$\dot{s} \leqslant -\eta. \tag{6.8}$$

In order to investigate $\dot{s}$, according to equation (6.6), the expression of the yaw acceleration $\dot{r}$ is required. Rearrangement of equation (3.72) yields the following expression for $\dot{r}$:

$$\dot{r} = \frac{1}{I_z}\Big(I_{xz}\dot{p} + \sum_{i=1}^{4} x_i(F_{xi}\sin\delta_i + F_{yi}\cos\delta_i) - \sum_{i=1}^{2} y_i(F_{xi}\cos\delta_i - F_{yi}\sin\delta_i) + \Delta M\Big), \tag{6.9}$$

with $\Delta M = \dfrac{d_{\mathrm{r}}}{2}(F_{x3} - F_{x4})$. Note that this ΔM is the yaw moment generated by the difference between the rear longitudinal tire forces.

To satisfy the sliding condition (6.8), the following corrective yaw moment command is proposed as the control input to the vehicle system:

$$\Delta M = \Delta M_{\mathrm{eq}} - k\operatorname{sgn}(r - r^*), \tag{6.10}$$

where k is a design parameter, and ΔM_{eq} is the term called "equivalent control" in the sliding mode control theory. In this application, ΔM_{eq} is given by:

$$\Delta M_{\text{eq}} = I_z \left(\dot{r}^* - \frac{|\Delta r|_{\max}}{|\beta|_{\max}} \frac{1-\rho}{\rho} \dot{\beta} \, \text{sgn} \left((r - r^*)\beta \right) \right)$$
$$- \sum_{i=1}^{4} x_i (F_{xi} \sin \delta_i + F_{yi} \cos \delta_i) + \sum_{i=1}^{2} y_i (F_{xi} \cos \delta_i - F_{yi} \sin \delta_i). \quad (6.11)$$

This ΔM_{eq} would maintain $\dot{s} = 0$ if all states in expression (6.11) were exactly known.

Substituting the above control input ΔM in equation (6.9), and substituting the resulting $\dot{r}$ in equation (6.6), the following expression for $\dot{s}$ can be derived:

$$\dot{s} = \frac{\rho}{I_z |\Delta r|_{\max}} \left(f \, \text{sgn}(r - r^*) - k \right), \quad (6.12)$$

with $f = I_{xz} \dot{p}$. Substituting equation (6.12) in the sliding condition (6.8) necessitates the design parameter k to satisfy:

$$k \geqslant f \, \text{sgn}(r - r^*) + \frac{\eta I_z |\Delta r|_{\max}}{\rho}. \quad (6.13)$$

Since I_{xz} is constant and the roll acceleration $\dot{p}$ is practically constrained, it can be assumed that the term f is bounded, i.e. $|f| \leqslant I_{xz} \dot{p}_{\max}$. In practice, a user-defined constant bound $F \geqslant I_{xz} \dot{p}_{\max}$ is applied. Therefore, to guarantee that the above condition (hence the sliding condition) is met, k can be chosen as:

$$k = F + \frac{\eta I_z |\Delta r|_{\max}}{\rho}. \quad (6.14)$$

The computation of the proposed control input ΔM requires the knowledge of some vehicle states including the yaw rate, vehicle side-slip and tire forces. The yaw rate can be measured by an on-board gyroscope with reasonable accuracy, and the vehicle side-slip can be estimated using one of the techniques proposed in [69–74]. Besides, the estimation of tire forces is addressed in [69, 70, 100, 101].

It is important to note that the measurement or estimation errors can be compensated for by appropriately increasing the chosen value of F. How this is the case for the force estimation error is shown in the following. Denoting the estimated longitudinal and lateral tire forces of the ith wheel by $\hat{F}_{xi}$ and $\hat{F}_{yi}$, respectively, the equivalent control ΔM_{eq} is computed as follows:

$$\Delta M_{\text{eq}} = I_z \left(\dot{r}^* - \frac{|\Delta r|_{\max}}{|\beta|_{\max}} \frac{1-\rho}{\rho} \dot{\beta} \, \text{sgn} \left((r - r^*)\beta \right) \right)$$
$$- \sum_{i=1}^{4} x_i (\hat{F}_{xi} \sin \delta_i + \hat{F}_{yi} \cos \delta_i) + \sum_{i=1}^{2} y_i (\hat{F}_{xi} \cos \delta_i - \hat{F}_{yi} \sin \delta_i), \quad (6.15)$$

which leads to the following expression for the term f in equation (6.12):

$$f = I_{xz}\dot{p} + \sum_{i=1}^{4} x_i\big((F_{xi} - \hat{F}_{xi})\sin\delta_i + (F_{yi} - \hat{F}_{yi})\cos\delta_i\big)$$
$$- \sum_{i=1}^{2} y_i\big((F_{xi} - \hat{F}_{xi})\cos\delta_i - (F_{yi} - \hat{F}_{yi})\sin\delta_i\big). \tag{6.16}$$

The chosen value of F in presence of the force estimation errors is then increased by the maximum value of the two error summation terms in (6.16). Namely, the design parameter F needs to be chosen in such a way that:

$$F \geqslant I_{xz}\dot{p}_{\max} + \sqrt{(\Delta F_x)^2 + (\Delta F_y)^2}\left(\sum_{i=1}^{4} |x_i| + \sum_{i=1}^{2} |y_i|\right), \tag{6.17}$$

where ΔF_x and ΔF_y denote the maximum estimation errors of the longitudinal and lateral tire forces, respectively. The above derivations imply that by appropriately increasing the value chosen for F (hence increasing the design parameter k), the effect of the measurement/estimation errors can be suppressed. It should be pointed out that the increase of the design parameter k inevitably enlarges the magnitude of the control input (thus the energy used) and exacerbates chattering, which necessitates an appropriate trade-off in the selection of k.

The proposed control input ΔM is discontinuous due to the presence of the "sgn" terms (see equations (6.10) and (6.11)), which in practice leads to chattering. In order to eliminate chattering, the control discontinuity is smoothed out by replacing $\mathrm{sgn}\big((r - r^*)\beta\big)$ with $\mathrm{sat}\left(\dfrac{(r - r^*)\beta}{\Phi_1}\right)$ and $\mathrm{sgn}(r - r^*)$ with $\mathrm{sat}\left(\dfrac{r - r^*}{\Phi_2}\right)$, where sat is the saturation function and Φ_1 and Φ_2 denote the boundary layer thicknesses [77]. Thus, the proposed control input ΔM is modified as:

$$\Delta M = I_z\left(\dot{r}^* - \frac{|\Delta r|_{\max}}{|\beta|_{\max}}\frac{1-\rho}{\rho}\dot{\beta}\,\mathrm{sat}\left(\frac{(r - r^*)\beta}{\Phi_1}\right)\right) - \sum_{i=1}^{4} x_i(F_{xi}\sin\delta_i + F_{yi}\cos\delta_i)$$
$$+ \sum_{i=1}^{2} y_i(F_{xi}\cos\delta_i - F_{yi}\sin\delta_i) - k\,\mathrm{sat}\left(\frac{r - r^*}{\Phi_2}\right). \tag{6.18}$$

The structure of the proposed DYC system is shown in Figure 6.1. The torque command ΔT generated from the sliding mode controller unit is given by:

$$\Delta T = \frac{\Delta M}{d_{\mathrm{r}}}R, \tag{6.19}$$

where d_{r} denotes the rear track width and R represents the tire radius. Apart from the sliding mode controller unit, a vehicle speed controller unit is also employed to generate a base torque T_{base} in such a way that the vehicle longitudinal velocity v_x follows the desired value v_x^* read from the throttle pedal sensor. Then T_{base} is added to $-\Delta T$ and
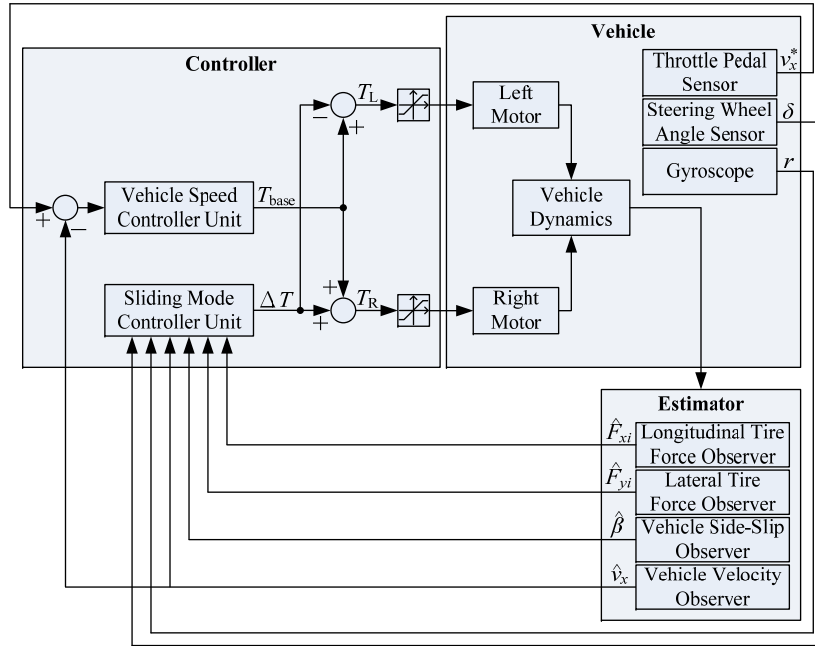
FIGURE 6.1: Schematic of the proposed DYC system.

$+\Delta T$ to form the motor torque commands T_{L} and T_{R}. Note that the vehicle speed controller unit can be shut down ($T_{\mathrm{base}} = 0$) to leave v_x uncontrolled.

6.3   SIMULATION RESULTS

In this section the comparative simulation results of three different methods are presented. They are the proposed DYC system, the DYC system employing equation (6.1) as the switching function, and the passive system which constantly sends identical torque commands to the two motors. In the following, for brevity, the three systems are referred to as the "proposed DYC", "conventional DYC" and "passive system", respectively. The full vehicle model established in Chapter 3 is employed again to simulate the vehicle maneuvers and produce the control performances of the three systems.

As mentioned in Chapter 4, to reveal the fundamental lateral and yaw behaviors, the vehicle longitudinal velocity v_x is normally maintained constant in the analysis [108, 109]. In this section, however, in order to thoroughly investigate the control performances of the above three methods, the simulation results for two cases, constant v_x and uncontrolled v_x, are presented. In the first case, v_x is maintained constant using T_{base} generated by the vehicle speed controller unit. In the second case, this controller unit is shut down ($T_{\mathrm{base}} = 0$) to leave v_x uncontrolled.

Note that with the proposed switching function (6.5), the following relationship holds:

$$s \propto |r - r^*| + \left(\frac{|\Delta r|_{\max}}{|\beta|_{\max}} \frac{1 - \rho}{\rho} \right) |\beta|. \tag{6.20}$$

Thus, once the user-defined parameters $|\Delta r|_{\max}$ and $|\beta|_{\max}$ are selected, for comparison purposes, the parameter ξ in the switching function (6.1) of the conventional DYC is set to:

$$\xi = \frac{|\Delta r|_{\max}}{|\beta|_{\max}} \frac{1 - \rho}{\rho}. \tag{6.21}$$

Therefore, each set of ρ, $|\Delta r|_{\max}$ and $|\beta|_{\max}$ corresponds to only one value of ξ, which provides comparable simulation results of the proposed DYC and the conventional DYC. In this study, $|\Delta r|_{\max} = 0.1$ rad/s and $|\beta|_{\max} = 0.02$ rad are chosen for the maximum yaw rate error and maximum vehicle side-slip. These values are set based on the observations from simulations in extreme driving conditions. As mentioned previously, the parameter ρ represents the emphasis on the yaw rate error (with $1 - \rho$ representing the emphasis on the vehicle side-slip). In the simulations, three different choices for this parameter are explored, ranging from higher emphasis on the yaw rate error to more emphasis on the vehicle side-slip: $\rho = 0.75$, 0.5 or 0.25. With the above choices of $|\Delta r|_{\max}$ and $|\beta|_{\max}$, the corresponding values of ξ are $5/3$, 5 or 15, respectively.

Two types of steering inputs are employed to simulate the common J-turn and lane change maneuvers [17, 23, 24, 80]. Besides, two values of initial longitudinal velocity, 60 km/h (16.7 m/s) and 80 km/h (22.2 m/s), are used to simulate a medium and a high lateral acceleration scenario, respectively[1]. In each simulation study, the performances of the proposed DYC, conventional DYC and passive system are examined and compared in terms of the yaw rate, vehicle path and vehicle side-slip responses.

6.3.1 Simulations with constant v_x

The following two case studies with constant vehicle longitudinal velocity v_x are first presented. The speed controller unit is activated to maintain v_x at 60 km/h and 80 km/h in these two case studies, respectively.

6.3.1.1 J-turn and lane change maneuvers at $v_x = 60$ km/h

This section demonstrates the results of the simulated J-turn and lane change maneuvers undergoing medium lateral acceleration caused by medium longitudinal velocity ($v_x =$

---

[1]Equation (3.43) shows that the vehicle lateral acceleration increases with the longitudinal velocity v_x. In view of this dependence, here $v_x = 60$ km/h and $v_x = 80$ km/h are adopted to simulate the maneuvers with medium and large lateral accelerations, respectively.
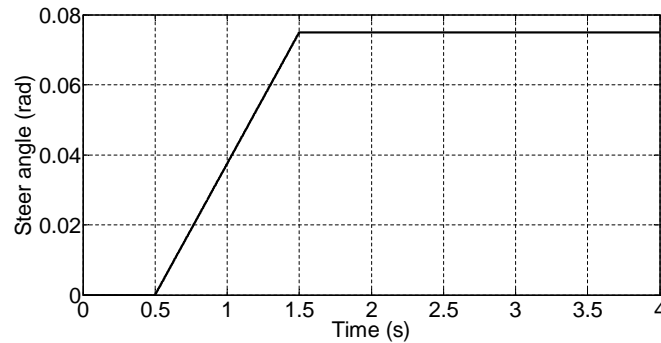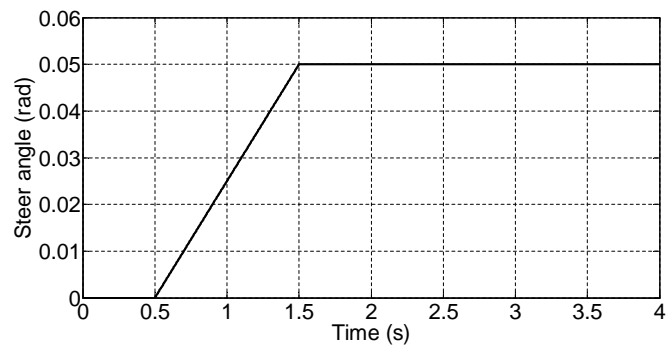
FIGURE 6.2: Front wheel steer angle for the J-turn maneuver at $v_x = 60$ km/h.

60 km/h). The front wheel steer angle used for the J-turn maneuver is plotted in Figure 6.2. Note that for a certain steer angle, perfect steer characteristic (i.e. neutral steer) corresponds to an ideal yaw rate described by equation (6.2). This ideal yaw rate response and the actual yaw rate responses produced by the three systems during this J-turn maneuver are plotted in Figure 6.3. Parts (a)–(c) of this figure show the results of the three methods with different parameter choices, starting from $\rho = 0.75$ in Figure 6.3 (a), then $\rho = 0.5$ in Figure 6.3 (b) and $\rho = 0.25$ in Figure 6.3 (c).

The following observations are made from the results demonstrated in Figure 6.3. Firstly, the yaw rate responses produced by the proposed DYC method closely track the ideal yaw rate, which provides the vehicle with neutral steer performance. This is while the other two methods lead to generally understeer behaviors (yaw rates smaller than ideal). The conventional DYC presents a very small steady-state error in the yaw rate response when $\rho = 0.75$ ($\xi = 5/3$), however the magnitude of this steady-state error increases when a smaller value of ρ (a larger value of ξ) is chosen. The passive system exhibits a yaw rate response that eventually converges to the ideal value, however, with a remarkable lag.

Figure 6.4 shows the vehicle paths produced by the three competing methods. The ideal curve represents the vehicle path traversed by a neutral steer vehicle. The results in this figure verify the observations made from Figure 6.3: the proposed DYC produces neutral steer behaviors and the vehicle paths closely track the ideal one, while the other two methods cause understeer behaviors and as a result, the vehicle paths deviate from the ideal one in outward direction (i.e. with larger turning radii). Note that the conventional DYC can lead the vehicle to track the ideal path tightly with $\rho = 0.75$ ($\xi = 5/3$), however the deviation from the ideal path deteriorates as ρ decreases (ξ increases).

Figure 6.5 demonstrates the vehicle side-slip responses with different control systems on-board. Again, the results show that the proposed DYC outperforms the competing methods and results in smaller vehicle side-slip values. The conventional DYC presents good vehicle side-slip performance when $\rho = 0.75$ ($\xi = 5/3$), however with smaller ρ's

(a)

(b)


(c)
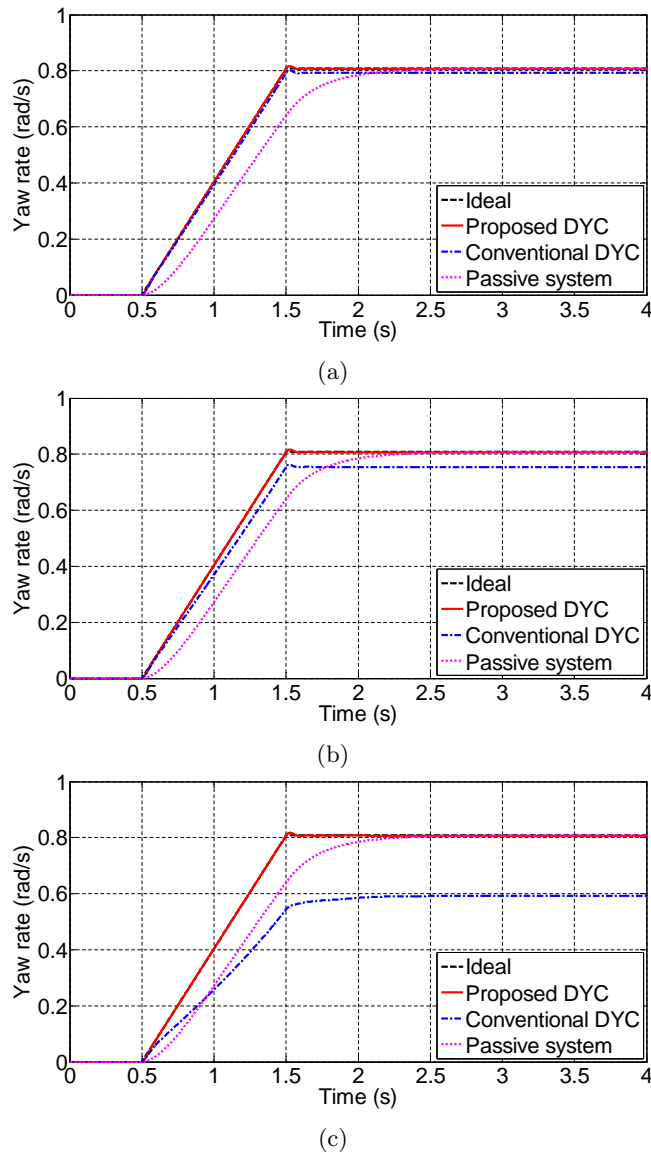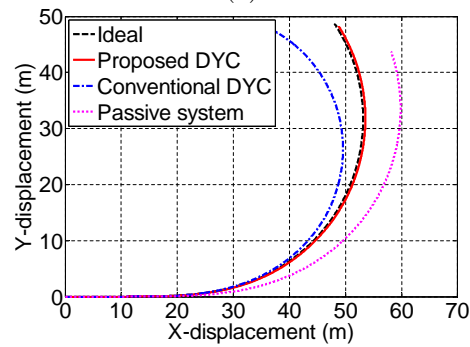
FIGURE 6.3: Yaw rate responses of the J-turn maneuver when $v_x = 60$ km/h and (a) $\rho = 0.75$ (b) $\rho = 0.5$ (c) $\rho = 0.25$.

(larger ξ's), its performance degrades and leads to larger vehicle side-slips. The passive system exhibits a response with a large spike before dropping to a steady-state value that has been already reached by the proposed DYC without any spike. In practice, such a spike can give rise to an undesirable swing of the vehicle heading direction.

It is important to note that in this case study, when the conventional DYC is employed, the yaw rate errors are non-positive at all times (see Figure 6.3) while the vehicle side-slip values remain non-negative (see Figure 6.5). As it was mentioned in section 6.1, the opposite signs of the two errors defy their convergences to zero even though the switching function (6.1) is controlled towards zero.
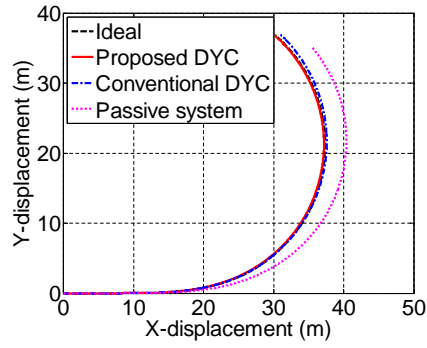
(a)
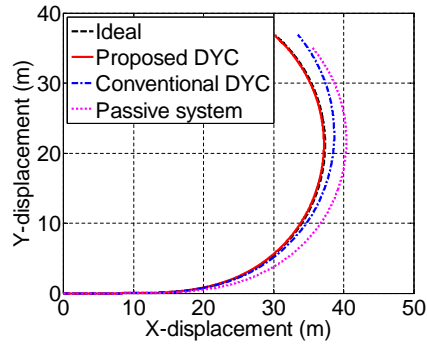
(b)
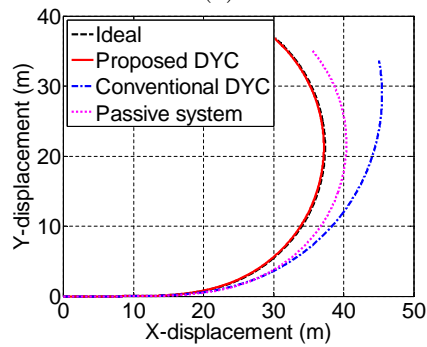
(c)

FIGURE 6.4: Vehicle paths of the J-turn maneuver when $v_x = 60$ km/h and (a) $\rho = 0.75$ (b) $\rho = 0.5$ (c) $\rho = 0.25$.
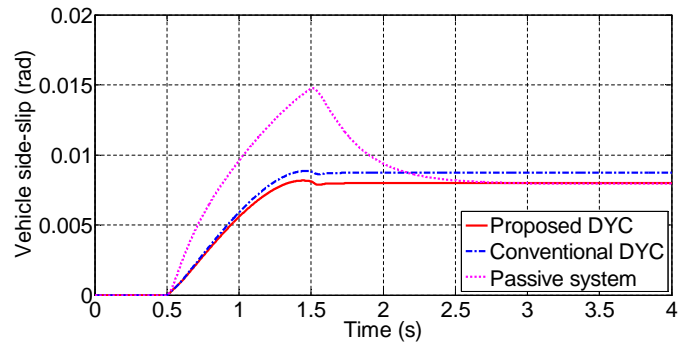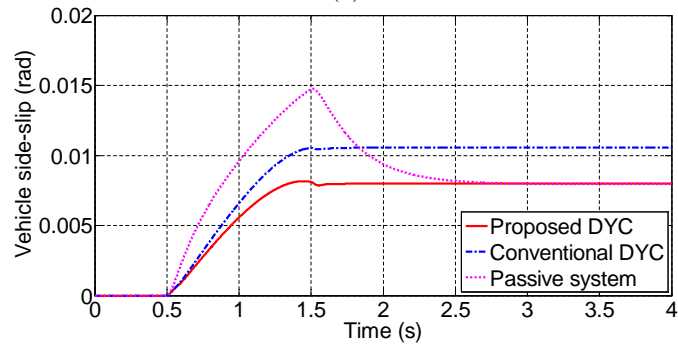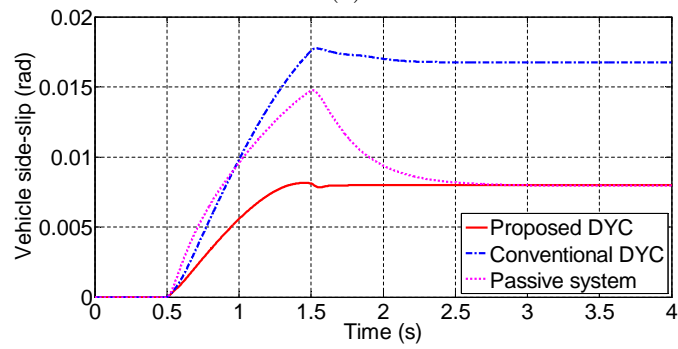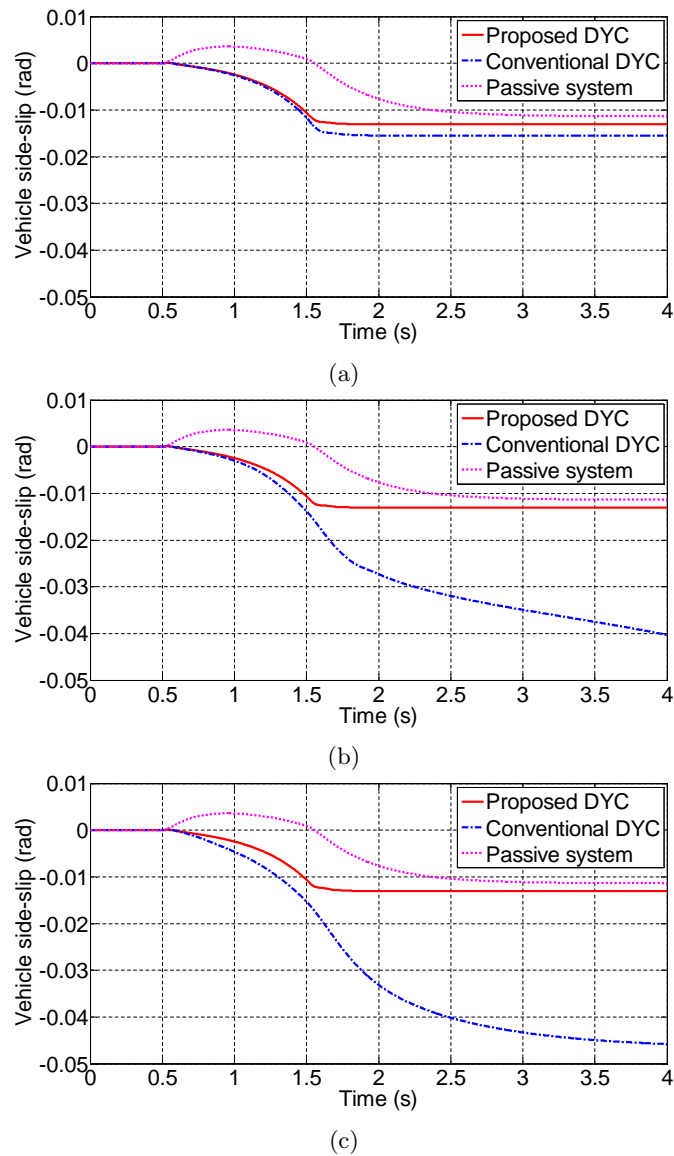
FIGURE 6.5: Vehicle side-slip responses of the J-turn maneuver when $v_x = 60$ km/h and (a) $\rho = 0.75$ (b) $\rho = 0.5$ (c) $\rho = 0.25$.
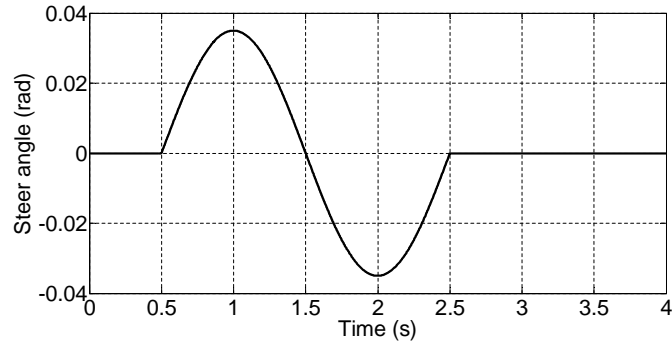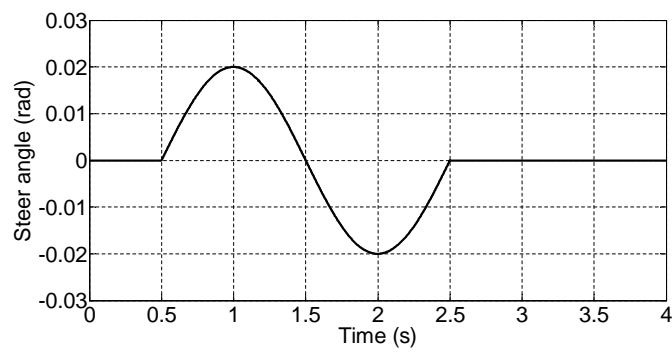
FIGURE 6.6: Front wheel steer angle for the lane change maneuver at $v_x = 60$ km/h.

In a different case study, a lane change maneuver is simulated with medium lateral acceleration ($v_x = 60$ km/h). The front wheel steer angle for this maneuver and the simulation results are presented in Figures 6.6–6.9. Note that the ideal curve in Figure 6.7 represents the desired yaw rate described by equation (6.2), and the ideal curve in Figure 6.8 denotes the vehicle path transversed by a neutral steer vehicle.

Similar to the J-turn maneuver case, the proposed DYC endows the vehicle with neutral steer behavior by tracking the desired yaw rate tightly. Again, with the conventional DYC on-board, the vehicle presents close-to-neutral steer performance (yaw rate very close to ideal) with $\rho = 0.75$ ($\xi = 5/3$), but the intensity of understeer increases as ρ decreases (ξ increases). The passive system still provides an obvious lag in the yaw rate response, thus also leads the vehicle to understeer.

The yaw rate results are verified by the vehicle paths shown in Figure 6.8. It is seen that the simulated vehicle can track the ideal path closely with all selected values of ρ only when the proposed DYC is employed.

As for the vehicle side-slip, the proposed DYC consistently provides the vehicle with the smallest vehicle side-slip magnitude. The passive system yields larger vehicle side-slip than the proposed DYC and presents a lead in the response, while the conventional DYC presents increasing vehicle side-slip as ρ drops (ξ increases).
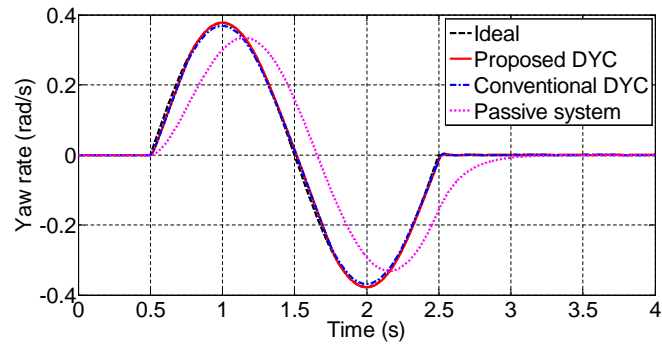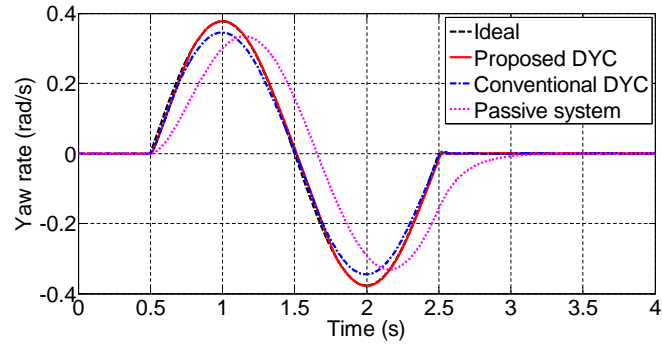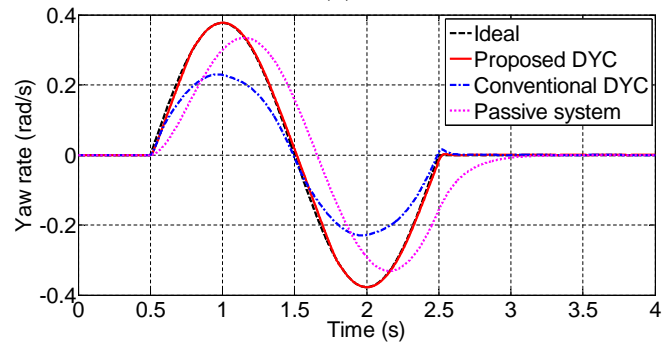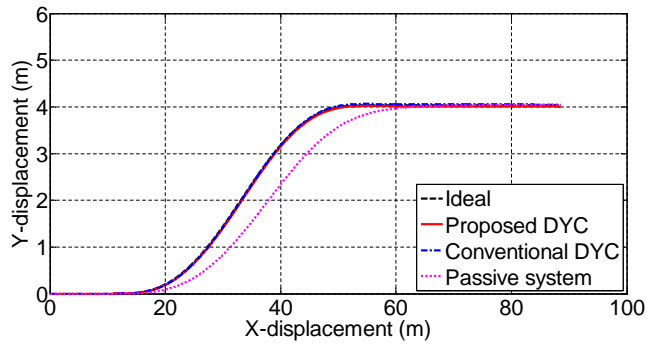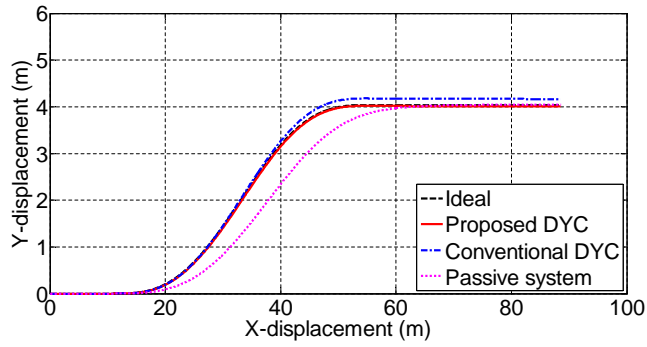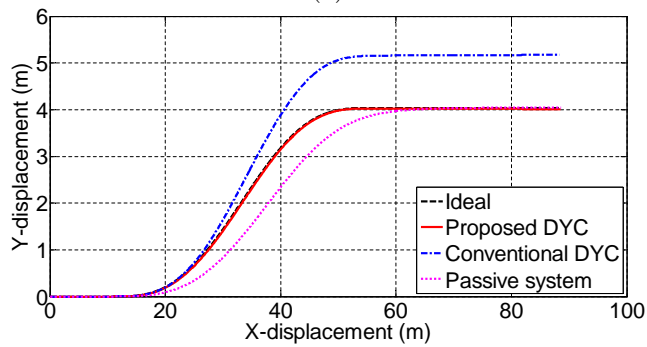
FIGURE 6.7: Yaw rate responses of the lane change maneuver when $v_x = 60$ km/h and (a) $\rho = 0.75$ (b) $\rho = 0.5$ (c) $\rho = 0.25$.
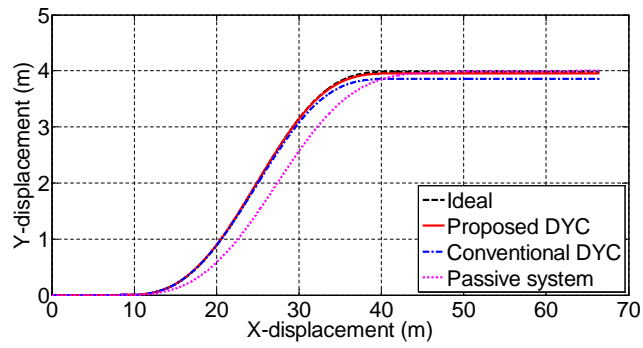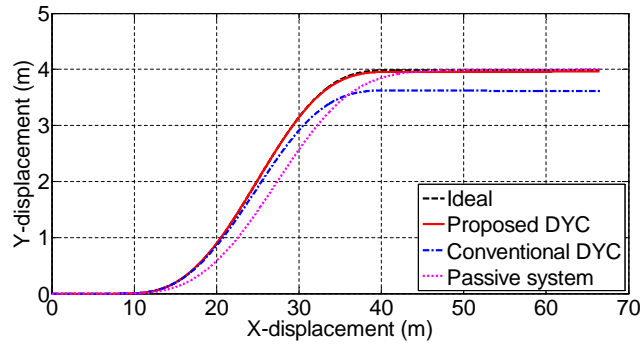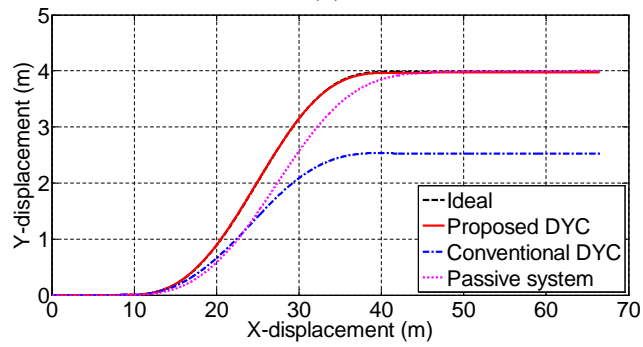
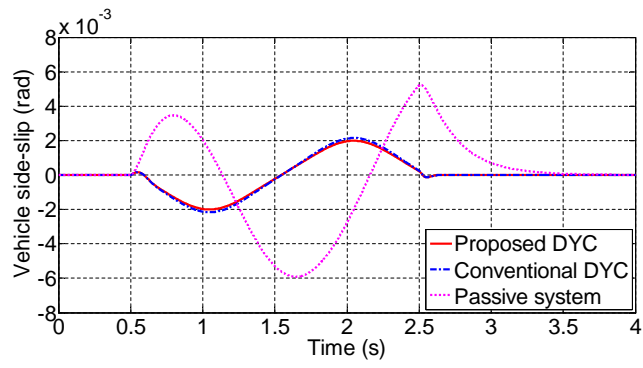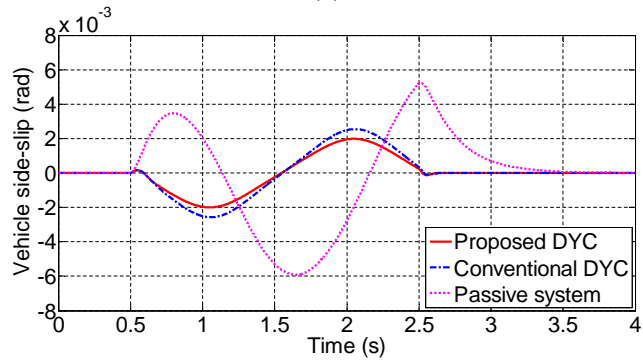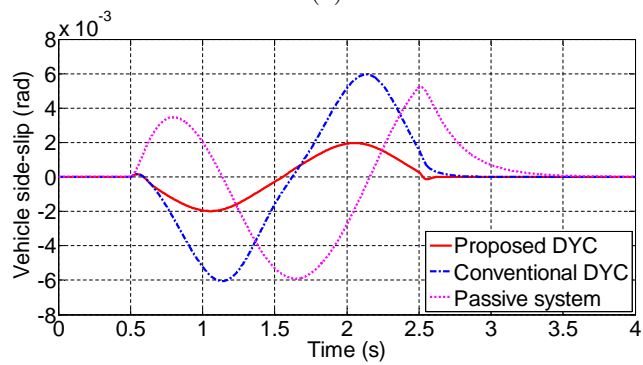FIGURE 6.8: Vehicle paths of the lane change maneuver when $v_x = 60$ km/h and (a) $\rho = 0.75$ (b) $\rho = 0.5$ (c) $\rho = 0.25$.
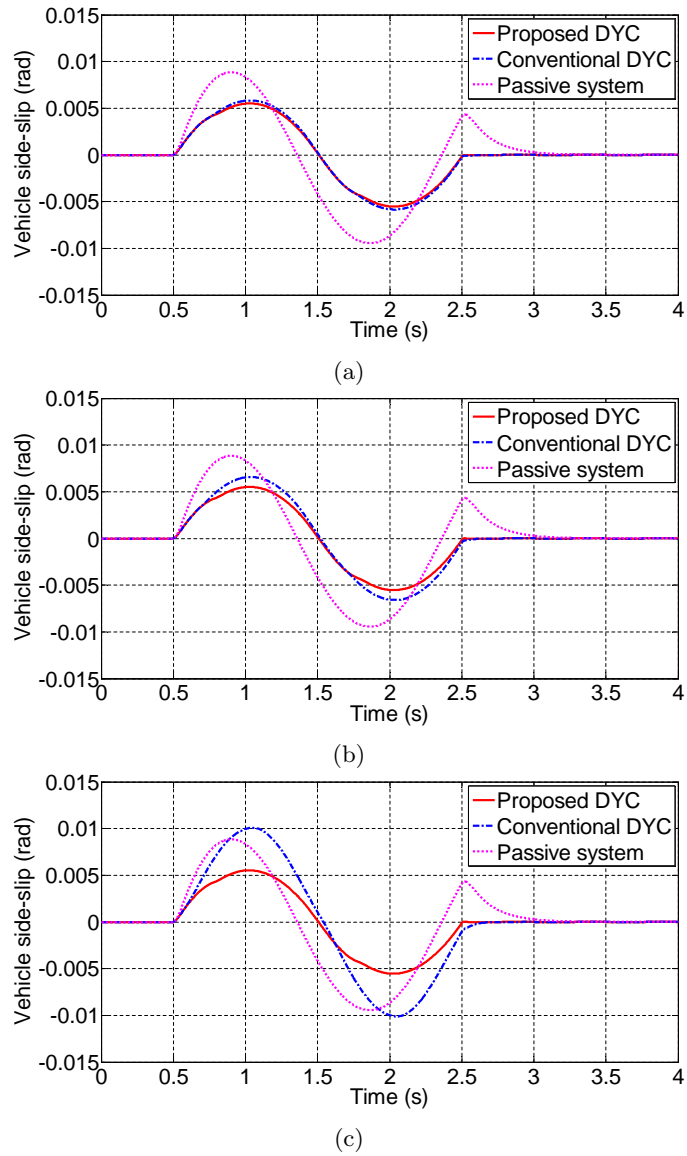
FIGURE 6.9: Vehicle side-slip responses of the lane change maneuver when $v_x = 60$ km/h and (a) $\rho = 0.75$ (b) $\rho = 0.5$ (c) $\rho = 0.25$.

6.3.1.2 J-turn and lane change maneuvers at $v_x = 80$ km/h

This section presents the results of the simulated J-turn and lane change maneuvers in presence of high lateral acceleration caused by high longitudinal velocity ($v_x = 80$ km/h). Figure 6.10 shows the steering input used to simulate the J-turn maneuver. The yaw rate responses, vehicle paths and vehicle side-slip responses during this J-turn maneuver are presented in Figures 6.11, 6.12 and 6.13, respectively. It is observed that in this high speed maneuver, the proposed DYC still leads the vehicle to track the desired yaw rate closely, and in turn makes the vehicle traverse in a path very close to the ideal one. Meanwhile, the passive system causes an obvious lag in the yaw rate response, deviating the vehicle path outward. The conventional DYC produces oversteer performance (yaw rate larger than ideal) and bends the vehicle path inward, which behavior deteriorates with smaller ρ values (larger ξ values).

In terms of the vehicle side-slip, it can be seen in Figure 6.13 that with the conventional DYC on-board, the vehicle side-slip remains small when ρ is large (ξ is small), however it diverges and the vehicle tends to spin as ρ decreases (ξ increase). In addition, the passive system exhibits a very slow oscillation: the vehicle side-slip climbs up slowly and then drops sluggishly. This slow convergence and the change of sign in vehicle side-slip do harm to the driver's sense of control. The proposed DYC produces fast convergence and small vehicle side-slip magnitude for all ρ values.

The steering command and vehicle responses for the lane change maneuver with high lateral acceleration ($v_x = 80$ km/h) are shown in Figures 6.14–6.17. The observations are similar to the case study of J-turn maneuver at high speed: with the proposed DYC on-board, the vehicle closely follows the ideal path, with its yaw rate tracking the ideal value tightly and its vehicle side-slip magnitude being generally less than the other methods. The conventional DYC results in intensifying oversteer behavior as well as increasing vehicle side-slip, with decreasing ρ (increasing ξ). The passive system causes a lag in the yaw rate response which gives rise to understeer performance. In the vehicle side-slip response, the passive system presents a remarkable phase difference from the other two, with a spike at the end of the steering command ($t = 2.5$ s).

FIGURE 6.10: Front wheel steer angle for the J-turn maneuver at $v_x = 80$ km/h.
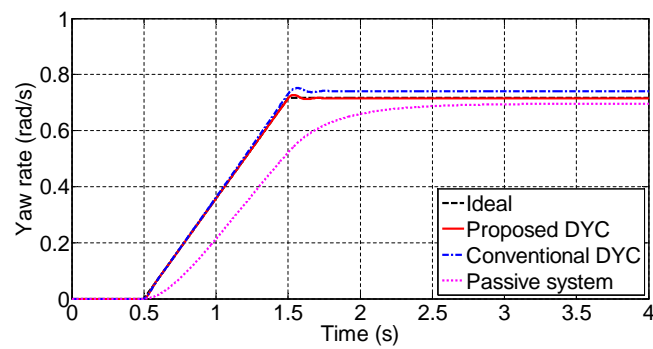
(a)
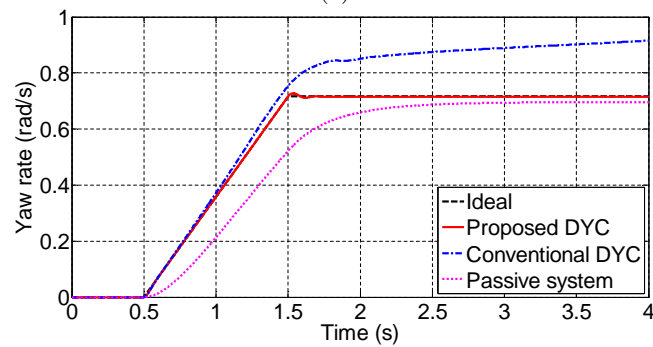
(b)
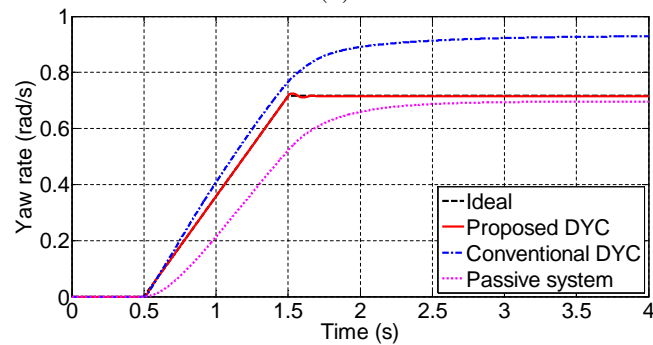
(c)

FIGURE 6.11: Yaw rate responses of the J-turn maneuver when $v_x = 80$ km/h and (a) $\rho = 0.75$ (b) $\rho = 0.5$ (c) $\rho = 0.25$.
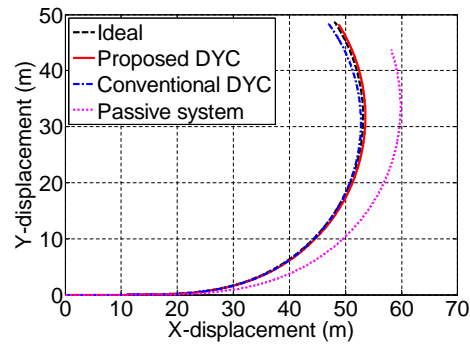
(a)
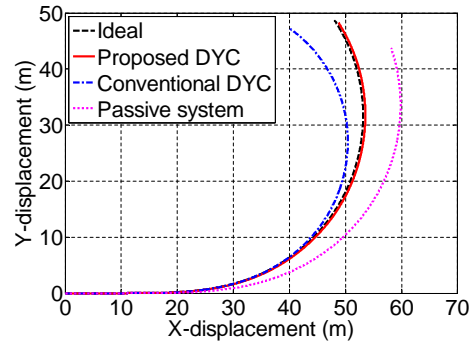
(b)

(c)

FIGURE 6.12: Vehicle paths of the J-turn maneuver when $v_x = 80$ km/h and (a) $\rho = 0.75$ (b) $\rho = 0.5$ (c) $\rho = 0.25$.

FIGURE 6.13: Vehicle side-slip responses of the J-turn maneuver when $v_x = 80$ km/h and (a) $\rho = 0.75$ (b) $\rho = 0.5$ (c) $\rho = 0.25$.

FIGURE 6.14: Front wheel steer angle for the lane change maneuver at $v_x = 80$ km/h.
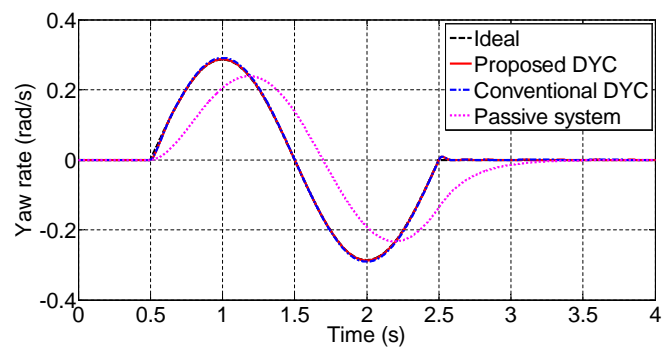
(a)
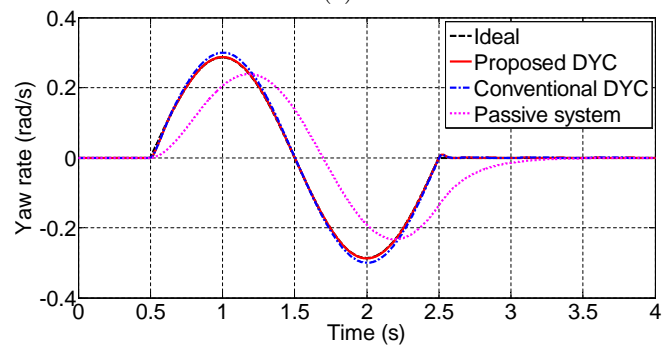
(b)
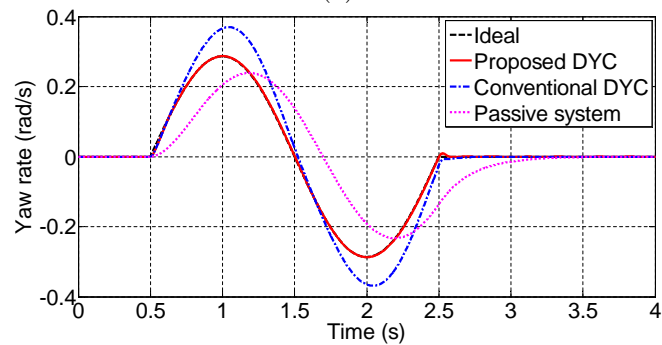
(c)

FIGURE 6.15: Yaw rate responses of the lane change maneuver when $v_x = 80$ km/h and (a) $\rho = 0.75$ (b) $\rho = 0.5$ (c) $\rho = 0.25$.

(a)

(b)

(c)

FIGURE 6.16: Vehicle paths of the lane change maneuver when $v_x = 80$ km/h and (a) $\rho = 0.75$ (b) $\rho = 0.5$ (c) $\rho = 0.25$.

(a)

(b)

(c)

FIGURE 6.17: Vehicle side-slip responses of the lane change maneuver when $v_x = 80$ km/h and (a) $\rho = 0.75$ (b) $\rho = 0.5$ (c) $\rho = 0.25$.

6.3.2 Simulations with uncontrolled v_x

In the preceding section, the simulation results with constant vehicle longitudinal velocities, $v_x = 60$ and $v_x = 80$, were demonstrated. The longitudinal velocities were maintained constant using T_{base} generated by the vehicle speed controller unit. As mentioned in Chapter 4, the analysis with constant longitudinal velocity can reveal the fundamental vehicle lateral and yaw behaviors. However, when v_x is not fixed, which is commonly the case in practice, the proposed DYC should also work effectively and provide satisfactory control performance. Thus in this section, the vehicle speed controller unit is shut down ($T_{\text{base}} = 0$) to leave the longitudinal velocity v_x uncontrolled. Intuitively, v_x will gradually decrease as the vehicle maneuvers. In the following two case studies, the initial longitudinal velocities are set to 60 km/h and 80 km/h, respectively.

6.3.2.1 J-turn and lane change maneuvers starting at $v_x = 60$ km/h

This section presents the results of the simulated J-turn and lane change maneuvers starting from $v_x = 60$ km/h. The front wheel steer angles employed for these two maneuvers are the same as those in the constant v_x case studies, as shown in Figures 6.2 and 6.6.

Since the vehicle speed controller unit is shut down, the vehicle longitudinal velocity v_x will change during the maneuvers. Figure 6.18 shows how v_x changes during the J-turn maneuver, with different values of ρ (ξ). All v_x curves gradually descend from 16.7 m/s (60 km/h) as the J-turn maneuver starts, and end up with slightly over 16 m/s. The three competing methods do not produce much discrepancy between each other in the v_x responses, as seen in Figure 6.18.

Figures 6.19–6.21 demonstrate the yaw rate, vehicle path and vehicle side-slip responses produced by the three methods during the J-turn maneuver, with different parameter choices. It is observed that the yaw rate responses are fairly similar to the constant v_x case shown in Figure 6.3, and they generally follow the same pattern as in the constant v_x scenario. The only difference presented in this case is that, with each value of ρ (ξ), all three response curves slightly drop as time elapses, which is caused by the gradually descending v_x. The vehicle paths also follow the same manner as in the constant v_x case. As for the vehicle side-slip responses, it is seen in Figure 6.21 that the response curves are at large similar to the ones in the constant v_x scenario shown in Figure 6.5. But, all three curves slightly increase as time goes by. This is because v_x gradually descends and v_y slightly increases as time elapses, and consequently the vehicle side-slip ($\beta = \arctan \dfrac{v_y}{v_x}$) increases.
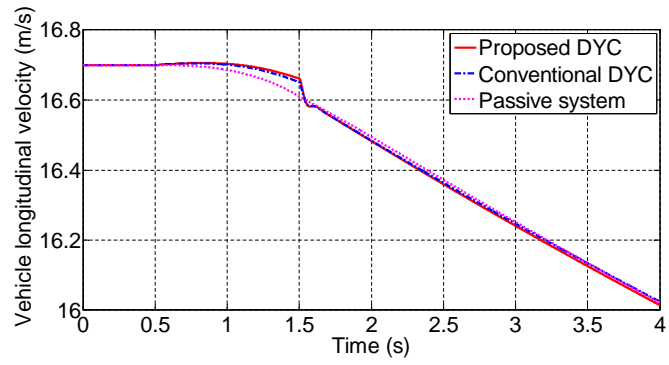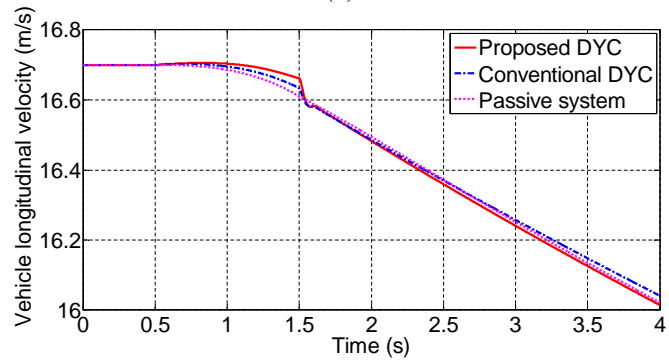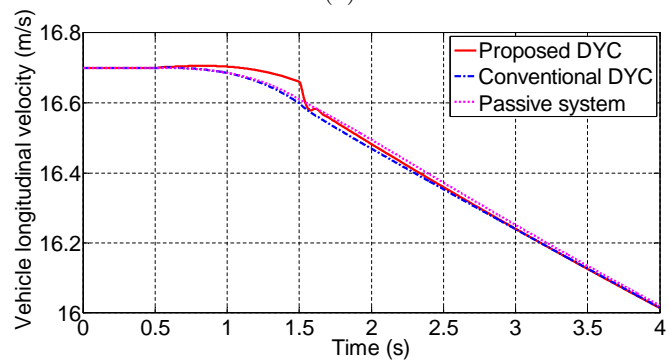
FIGURE 6.18: Vehicle longitudinal velocity responses of the J-turn maneuver starting at $v_x = 60$ km/h with (a) $\rho = 0.75$ (b) $\rho = 0.5$ (c) $\rho = 0.25$.
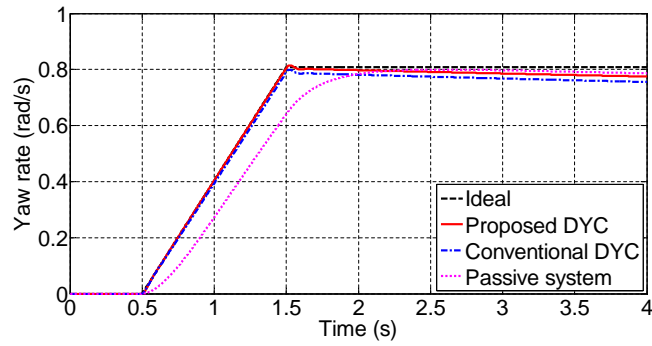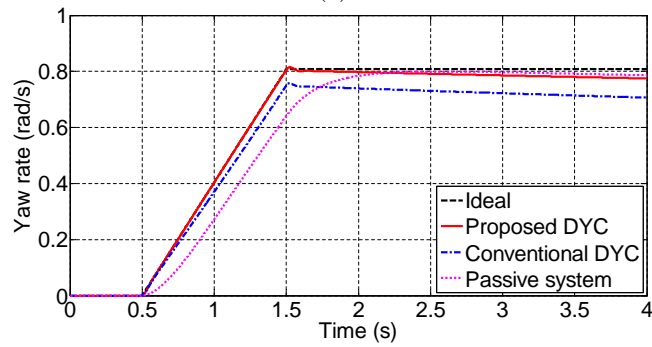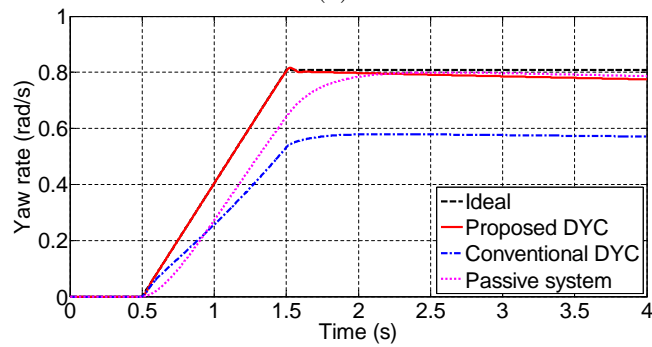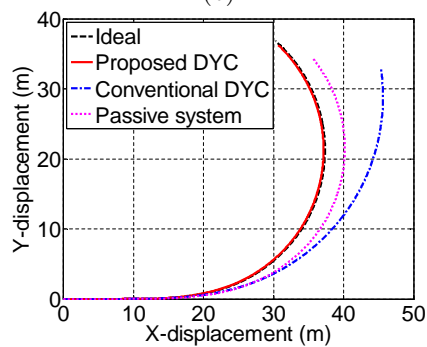
FIGURE 6.19: Yaw rate responses of the J-turn maneuver starting at $v_x = 60$ km/h with (a) $\rho = 0.75$ (b) $\rho = 0.5$ (c) $\rho = 0.25$.
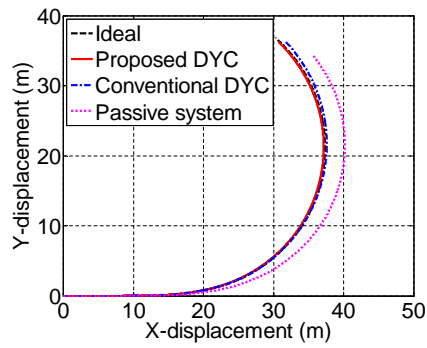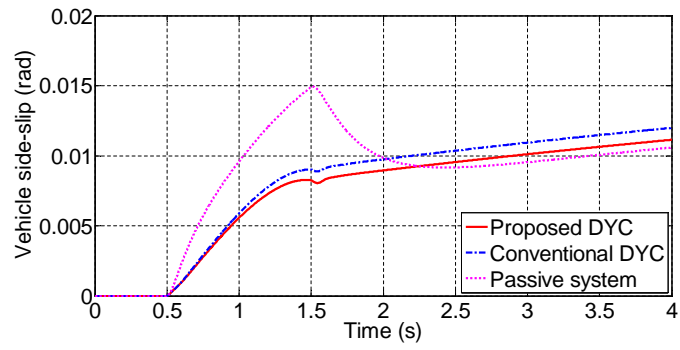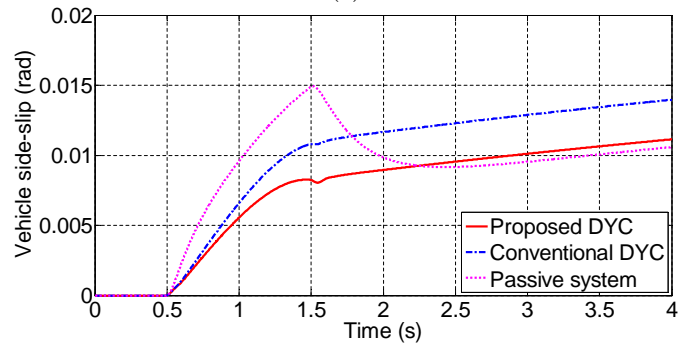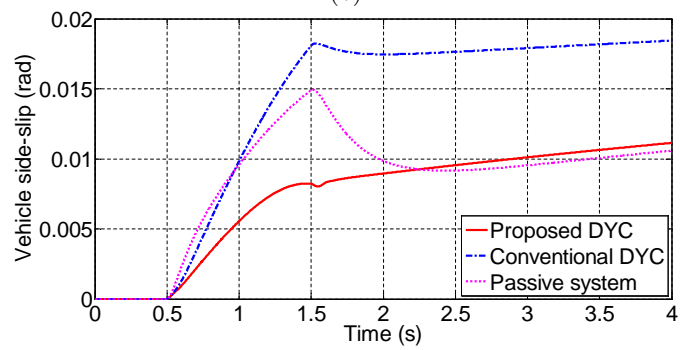
(a)
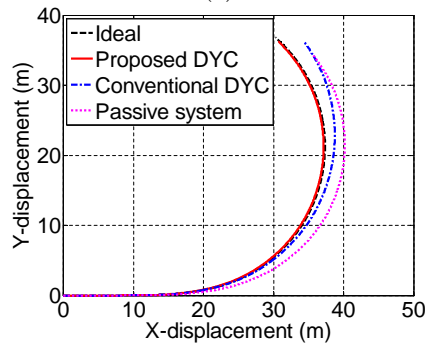
(b)

(c)

FIGURE 6.20: Vehicle paths of the J-turn maneuver starting at $v_x = 60$ km/h with (a) $\rho = 0.75$ (b) $\rho = 0.5$ (c) $\rho = 0.25$.
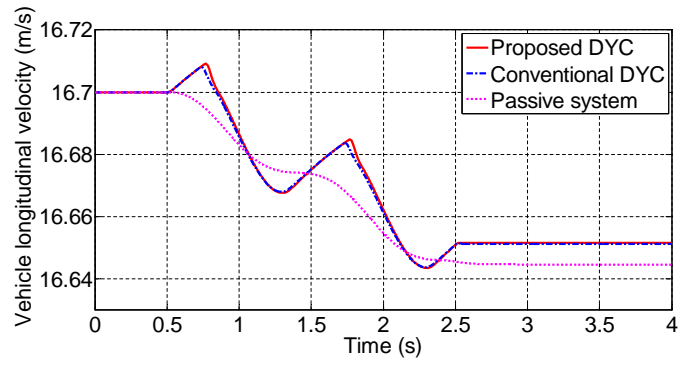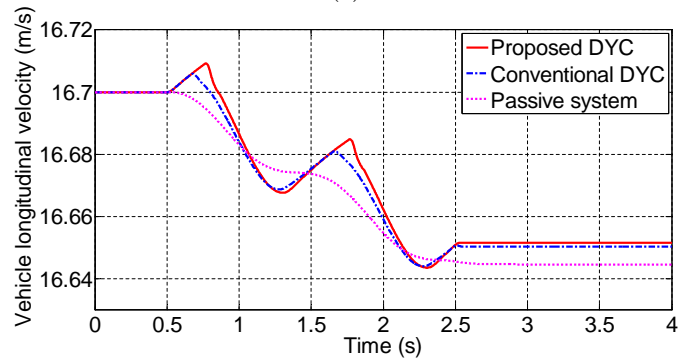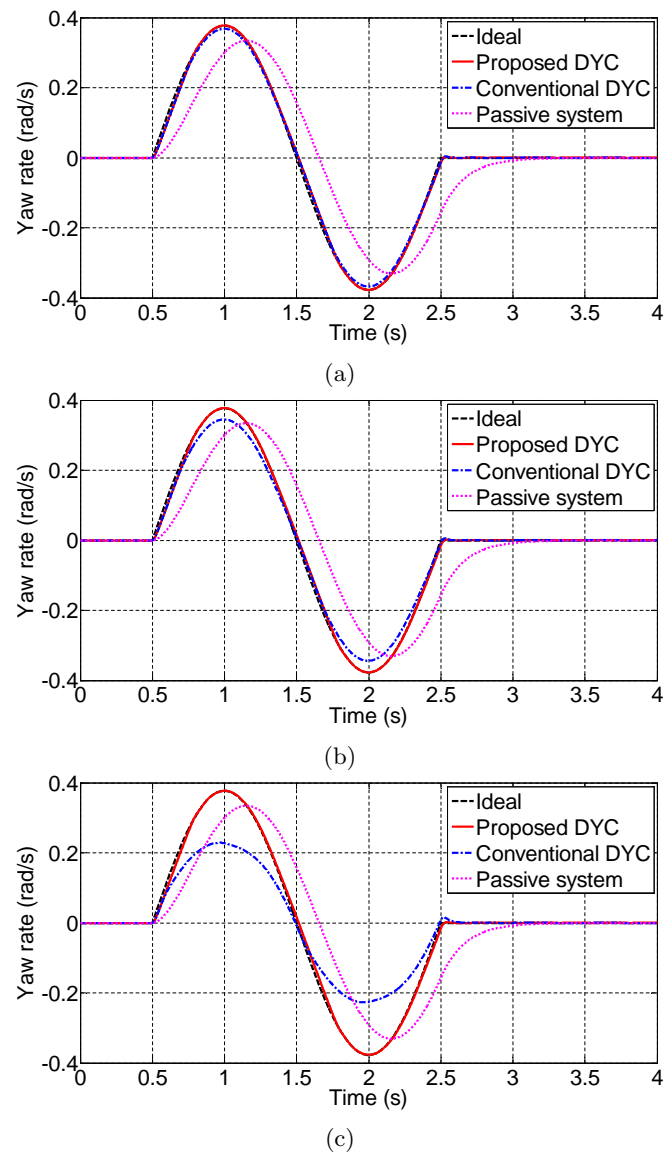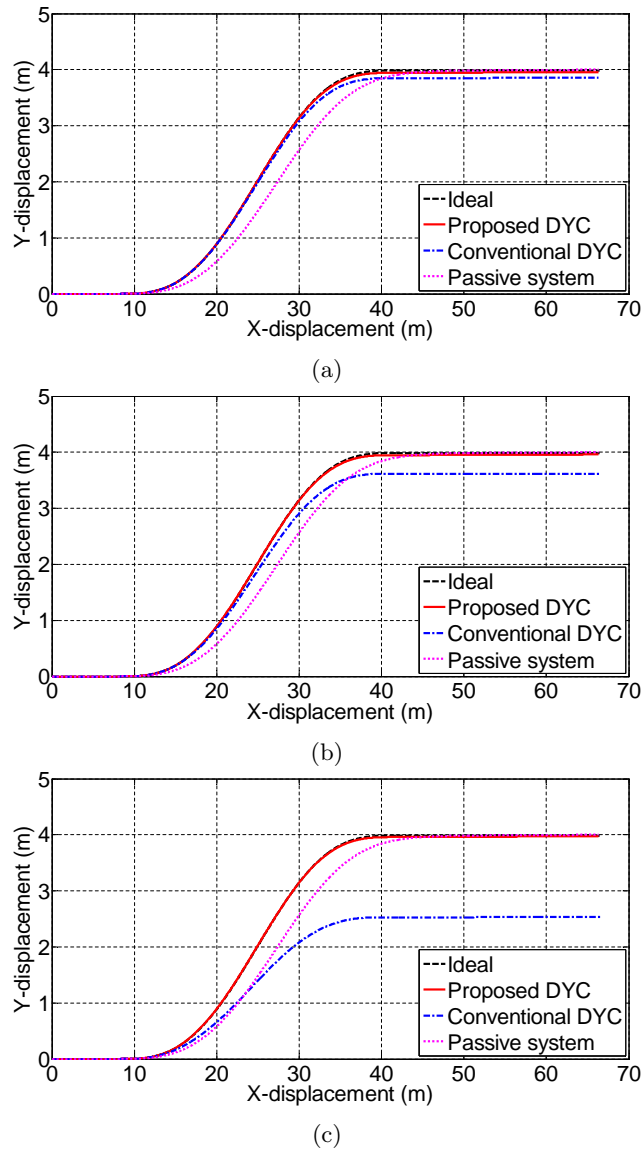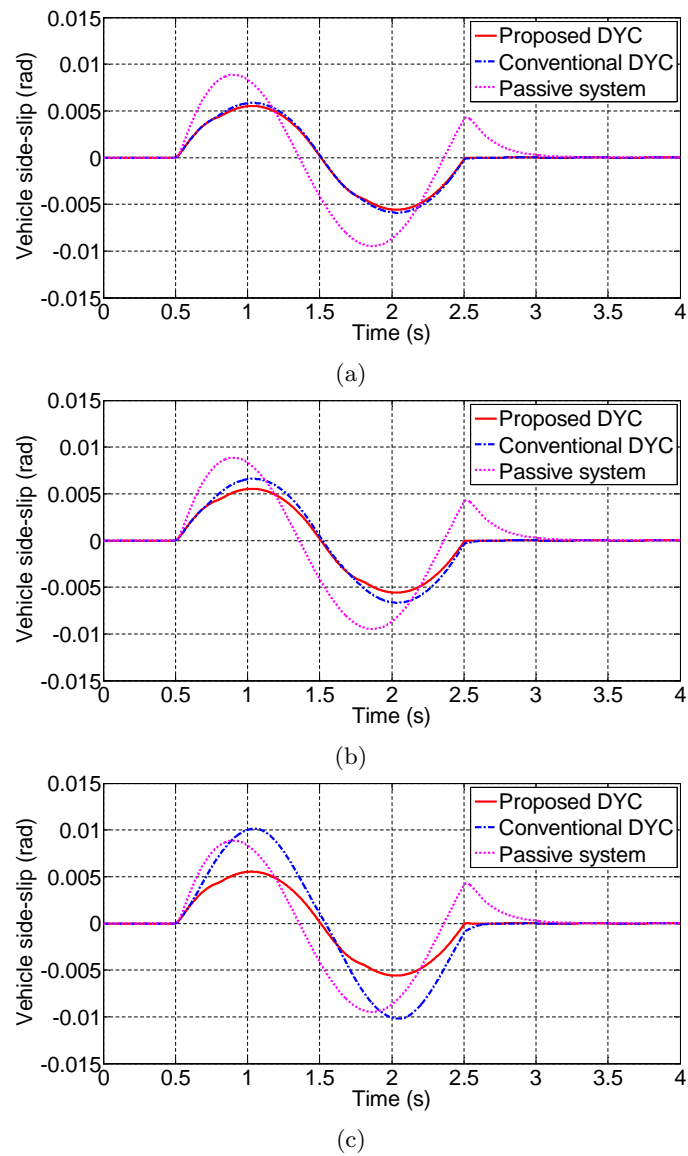
FIGURE 6.21: Vehicle side-slip responses of the J-turn maneuver starting at $v_x = $ 60 km/h with (a) $\rho = 0.75$ (b) $\rho = 0.5$ (c) $\rho = 0.25$.

Figure 6.22 shows how v_x changes during the lane change maneuver, starting from $v_x = 60$ km/h with different values of ρ (ξ). During this maneuver, with each value of ρ (ξ), the three response curves present slight decreases with some oscillations. The proposed DYC generally produces the largest oscillation, but this does not impair the vehicle performance as the magnitude of this oscillation is very small. With the conventional DYC on-board, the v_x oscillation gradually abates as ρ drops (ξ increases). The passive system, on the other hand, produces the smoothest v_x response.

Figures 6.23–6.25 demonstrate the yaw rate, vehicle path and vehicle side-slip responses during the lane change maneuver, employing different parameter choices. It can be seen that these three types of vehicle responses are almost the same as the responses in the constant v_x case presented in Figures 6.7–6.9. This similarity is easily comprehensible: even though v_x in general drops with all three methods on-board, yet the magnitudes of the v_x variations are quite small.
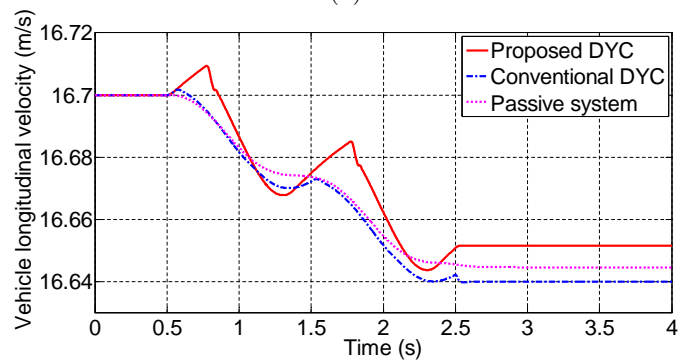
FIGURE 6.22: Vehicle longitudinal velocity responses of the lane change maneuver starting at $v_x = 60$ km/h with (a) $\rho = 0.75$ (b) $\rho = 0.5$ (c) $\rho = 0.25$.

FIGURE 6.23: Yaw rate responses of the lane change maneuver starting at $v_x = 60$ km/h with (a) $\rho = 0.75$ (b) $\rho = 0.5$ (c) $\rho = 0.25$.

FIGURE 6.24: Vehicle paths of the lane change maneuver starting at $v_x = 60$ km/h with (a) $\rho = 0.75$ (b) $\rho = 0.5$ (c) $\rho = 0.25$.

FIGURE 6.25: Vehicle side-slip responses of the lane change maneuver starting at $v_x = 60$ km/h with (a) $\rho = 0.75$ (b) $\rho = 0.5$ (c) $\rho = 0.25$.

6.3.2.2   J-turn and lane change maneuvers starting at $v_x = 80$ km/h

This section presents the results of the simulated J-turn and lane change maneuvers starting from a higher vehicle longitudinal velocity, $v_x = 80$ km/h. The front wheel steer angles used for these two maneuvers are the same as those in the constant v_x case studies, as shown in Figures 6.10 and 6.14.

Figure 6.26 demonstrates how v_x changes during the J-turn maneuver, with different values of ρ (ξ). As shown in this figure, when $\rho = 0.75$ ($\xi = 5/3$) and $\rho = 0.5$ ($\xi = 5$), all v_x curves generally start descending from 22.2 m/s (80 km/h) as the J-turn maneuver begins. This is similar to the v_x responses shown in Figure 6.18. However, in Figure 6.26 (c) it is observed that with $\rho = 0.25$ ($\xi = 15$), the conventional DYC leads v_x to increase after this J-turn maneuver begins, and the curve reaches a peak of about 24 m/s at around $t = 4$ s.

Figure 6.27 plots the yaw rate responses generated by the three competing control solutions during this maneuver. The overall tendency of the response curves follows the same pattern shown in Figure 6.11. With the proposed DYC on-board, the simulated vehicle best tracks the ideal yaw rate response. The conventional DYC produces good performance with $\rho = 0.75$ ($\xi = 5/3$), however as ρ drops (ξ increases) the conventional DYC provides intensifying oversteer. The passive system still presents a remarkable lag in the yaw rate response. Similarly, the vehicle paths of this J-turn maneuver, as shown in Figure 6.28, are almost the same as those in the constant v_x case previously presented in Figure 6.12.

As for the vehicle side-slip responses in Figure 6.29, the curves produced by the proposed DYC and the passive system, in general, follow the same fashion as the responses in the constant v_x scenario (shown in Figure 6.13). However with the conventional DYC on-board, it was observed in Figure 6.13 that the vehicle side-slip diverges when $\rho = 0.5$ ($\xi = 5$), while in Figure 6.29 the corresponding curve is still stable and its magnitude decreases after experiencing a peak. When ρ decreases to 0.25 (ξ increases to 15), the conventional DYC makes the vehicle side-slip diverge in both constant and uncontrolled v_x cases, but the diverging rate in Figure 6.13 is mush slower than that in Figure 6.29.
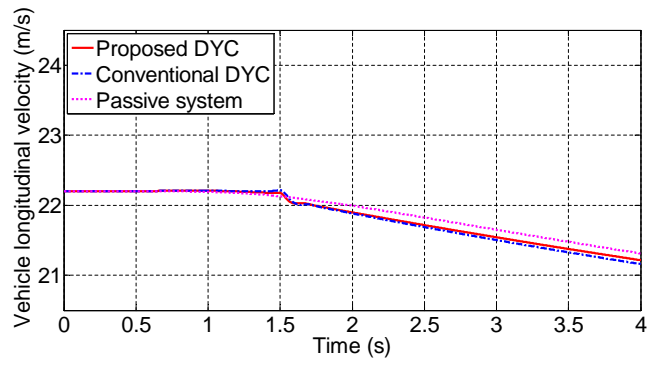
(a)
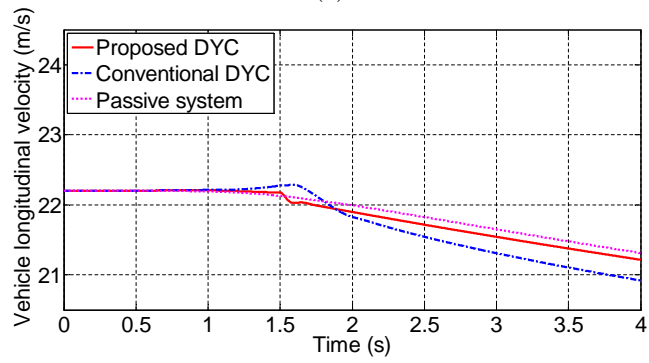
(b)
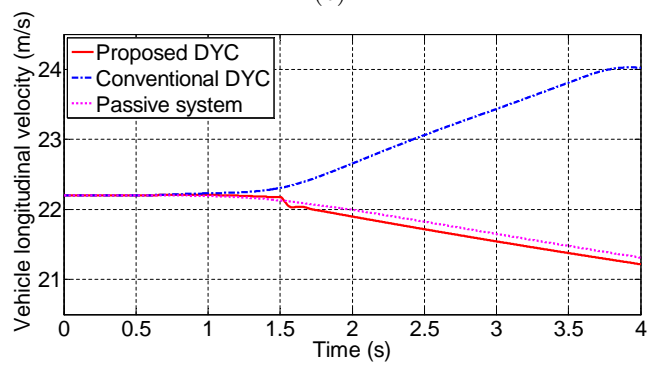
(c)

FIGURE 6.26: Vehicle longitudinal velocity responses of the J-turn maneuver starting at $v_x = 80$ km/h with (a) $\rho = 0.75$ (b) $\rho = 0.5$ (c) $\rho = 0.25$.
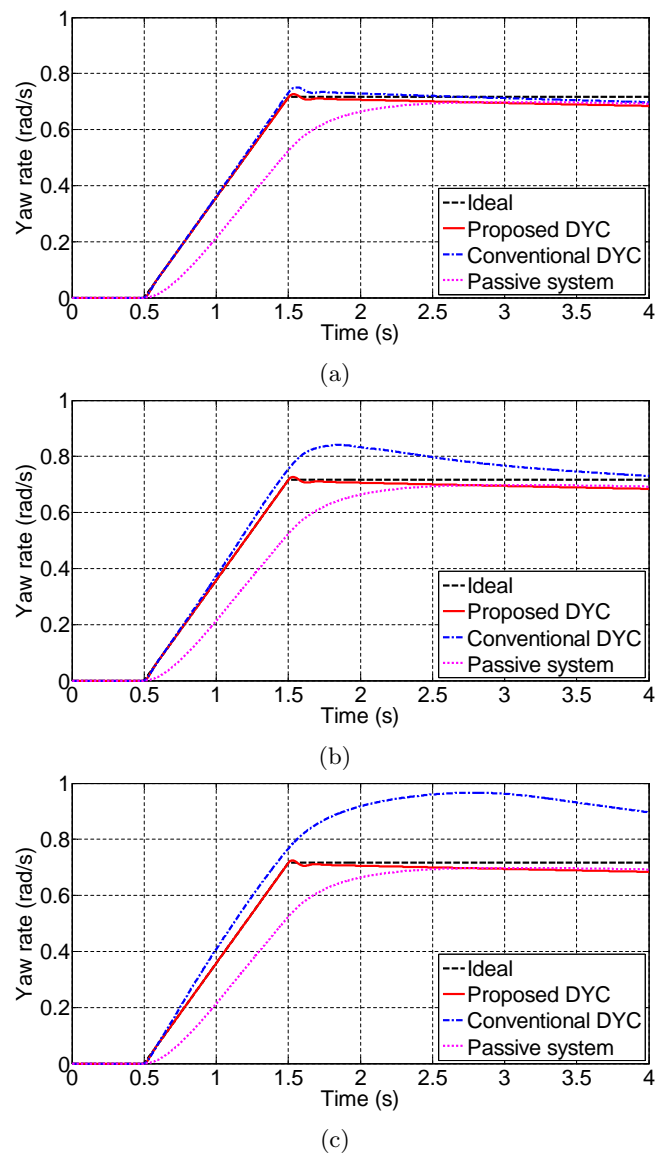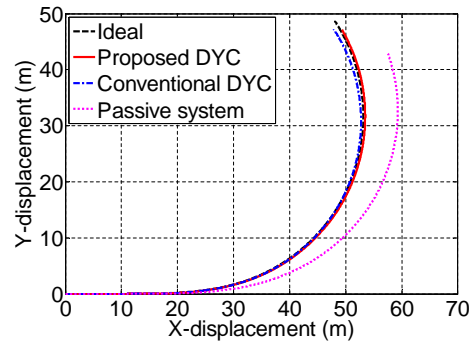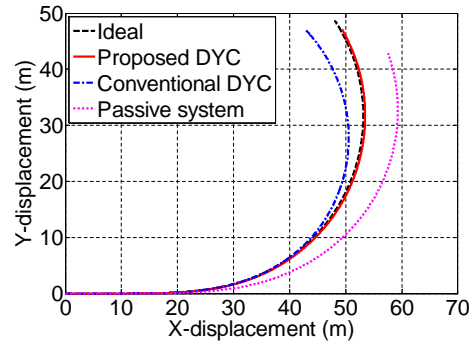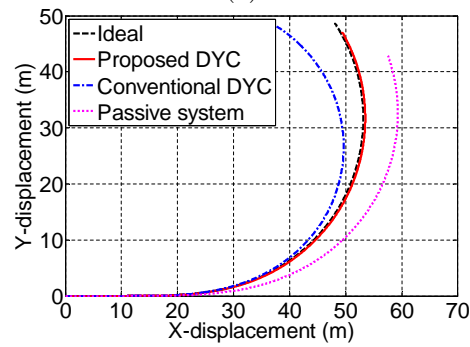
FIGURE 6.27: Yaw rate responses of the J-turn maneuver starting at $v_x = 80$ km/h with (a) $\rho = 0.75$ (b) $\rho = 0.5$ (c) $\rho = 0.25$.
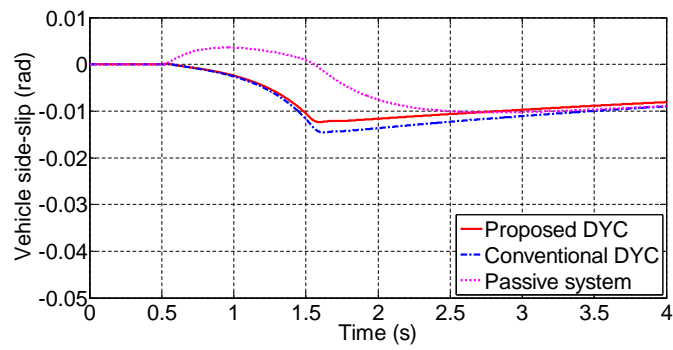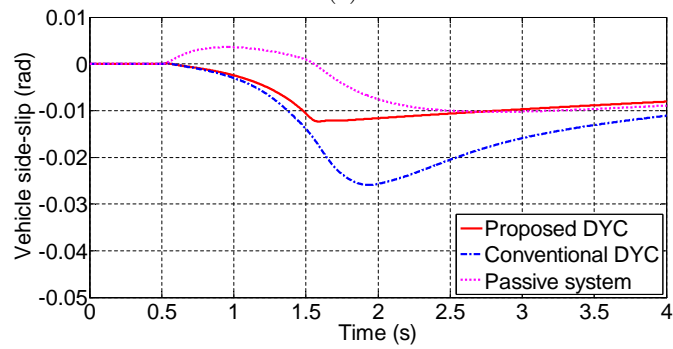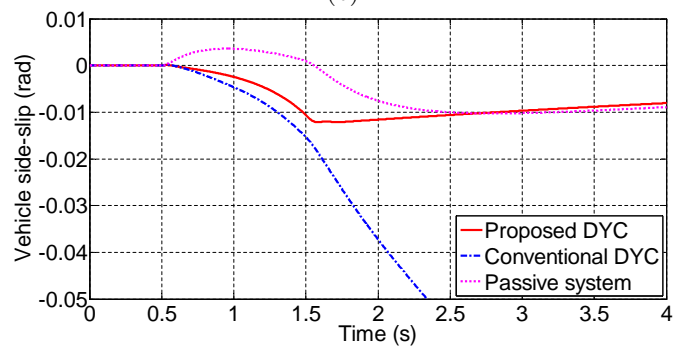
(a)

(b)

(c)

FIGURE 6.28: Vehicle paths of the J-turn maneuver starting at $v_x = 80$ km/h with (a) $\rho = 0.75$ (b) $\rho = 0.5$ (c) $\rho = 0.25$.
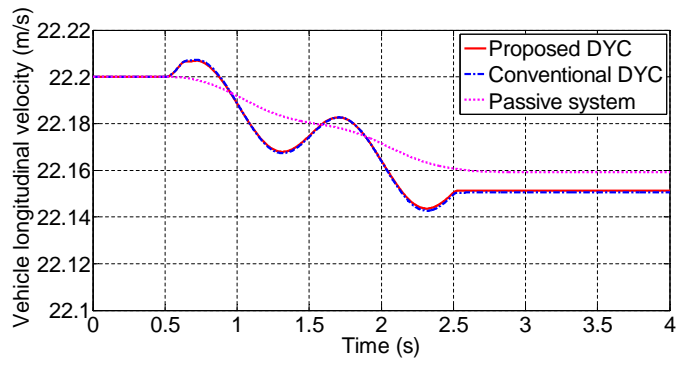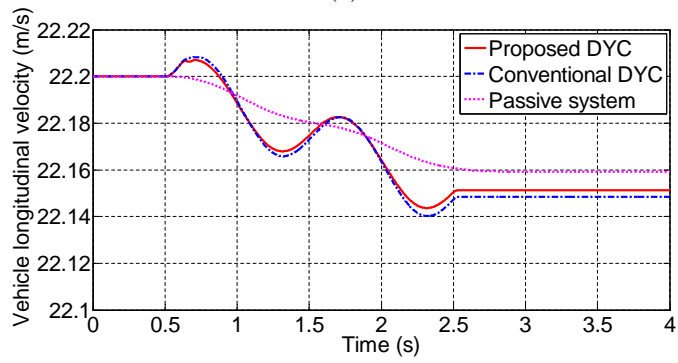
FIGURE 6.29: Vehicle side-slip responses of the J-turn maneuver starting at $v_x = 80$ km/h with (a) $\rho = 0.75$ (b) $\rho = 0.5$ (c) $\rho = 0.25$.

Figure 6.30 demonstrates the v_x responses during the lane change maneuver starting from $v_x = 80$ km/h, with different choices of ρ (ξ). As shown in this figure, the v_x response curves generally descend after the lane change maneuver commences. The responses produced by the conventional DYC and the proposed DYC present oscillations, and the conventional DYC leads the magnitude of oscillation to increase as ρ decreases (ξ increases). Note that the magnitudes of all these oscillations are generally fairly small.

Figures 6.31–6.33 demonstrate the yaw rate, vehicle path and vehicle side-slip responses during this lane change maneuver. These responses follow almost the same patterns as in the constant v_x case shown in Figures 6.15–6.17. When the proposed DYC is employed, the vehicle closely tracks the ideal yaw rate and tightly follows the desired path, and the vehicle side-slip magnitude is also generally less than the other two. The conventional DYC results in intensifying oversteer behavior and increasing vehicle side-slip magnitude, as ρ descends (ξ rises). The passive system causes lags in the yaw rate and vehicle path responses, which leads the vehicle to understeer. Besides, like the constant v_x case, the vehicle side-slip response of the passive system presents a remarkable phase difference from the other two, and it shows a spike in the response at the end of the steering command ($t = 2.5$ s).
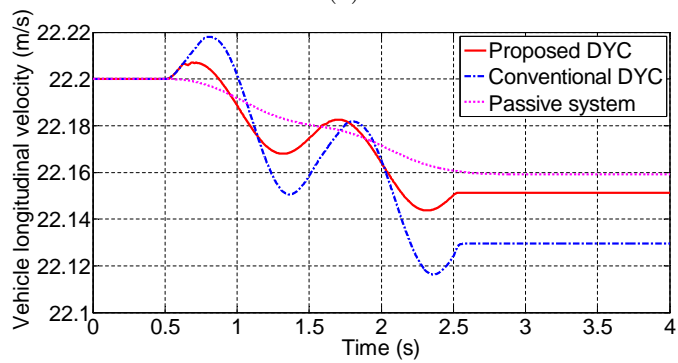
FIGURE 6.30: Vehicle longitudinal velocity responses of the lane change maneuver starting at $v_x = 80$ km/h with (a) $\rho = 0.75$ (b) $\rho = 0.5$ (c) $\rho = 0.25$.
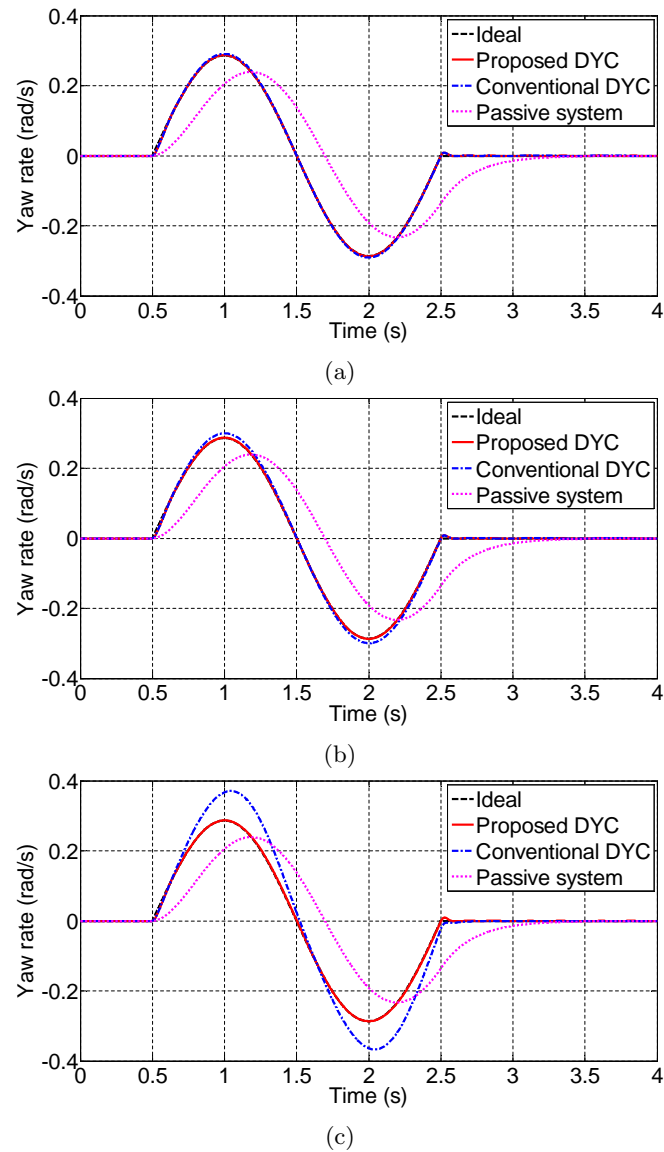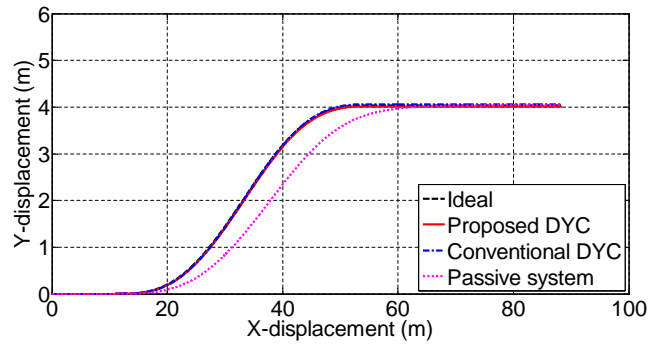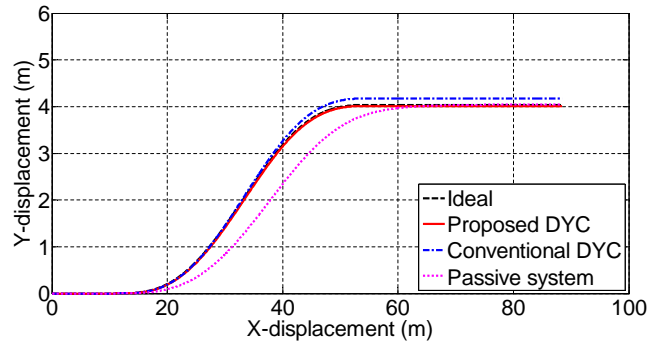
FIGURE 6.31: Yaw rate responses of the lane change maneuver starting at $v_x = $ 80 km/h with (a) $\rho = 0.75$ (b) $\rho = 0.5$ (c) $\rho = 0.25$.

FIGURE 6.32: Vehicle paths of the lane change maneuver starting at $v_x = 80$ km/h with (a) $\rho = 0.75$ (b) $\rho = 0.5$ (c) $\rho = 0.25$.

(a)

(b)

(c)

FIGURE 6.33: Vehicle side-slip responses of the lane change maneuver starting at $v_x = 80$ km/h with (a) $\rho = 0.75$ (b) $\rho = 0.5$ (c) $\rho = 0.25$.
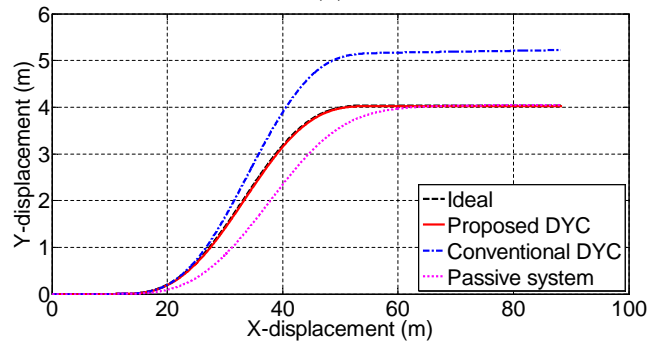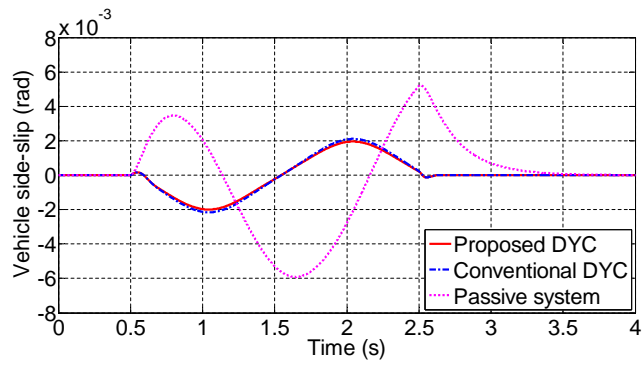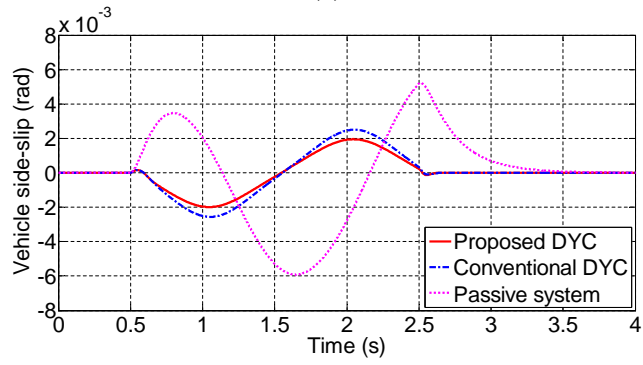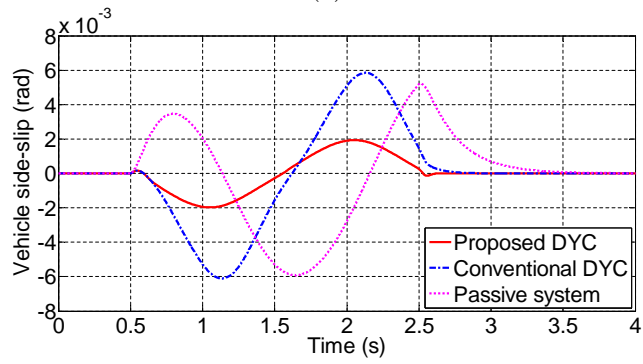
6.4   SUMMARY

In this chapter, a novel sliding mode DYC design for simultaneous control of the yaw rate and vehicle side-slip is presented. The proposed sliding mode controller employs a linear combination of the normalized absolute values of the yaw rate and vehicle side-slip errors as the switching function. The complete nonlinear vehicle equations of motion derived in Chapter 3 are employed to formulate the sliding mode control command.

Extensive comparative simulations are conducted to verify the effectiveness of the proposed DYC scheme. In the simulation studies, the vehicle undergoes the J-turn and lane change maneuvers with constant or uncontrolled vehicle longitudinal velocities. The simulation results demonstrate that the proposed DYC solution clearly outperforms the compared methods in terms of achieving close-to-neutral steer characteristic, tracking the ideal vehicle path, and obtaining smaller magnitude of vehicle side-slip.

Chapter 7

Conclusions and Recommendations

7.1 CONCLUSIONS

Direct yaw moment control systems produce a corrective yaw moment to achieve enhanced vehicle handling and stability, by means of individual control of longitudinal tire forces (braking and/or traction forces). Conventionally, DYC systems were commonly realized in the form of braking-based VSC systems or active differentials, either of which presents certain types of downsides. Since the advent of electric vehicles (or hybrid vehicles) equipped with independent driving motors, the latest type of DYC using electric motors to generate the corrective yaw moment has become a research focus. This new DYC type presents several apparent advantages over the conventional DYC schemes, and its effectiveness in enhancing the vehicle handling and stability has been verified by the published works.

Most existing DYC schemes adopt the yaw rate and/or vehicle side-slip as the main control variable(s), as these two vehicle states are known to be the fundamental states that govern the vehicle handling and stability. The scope of this study has been focused on the analysis and design of the latest DYC type for electric vehicles (or hybrid vehicles) with independent driving motors, employing the yaw rate and/or vehicle side-slip as the control variable(s).

This thesis has looked into a wide range of existing vehicle dynamics control designs, ranging from the basic and straightforward solutions to the state-of-the-art DYC schemes. In a detailed literature review, the theories used in the control techniques were explained and the characteristics of each control scheme were highlighted. Then, a full vehicle

model including the vehicle equivalent mechanical model, vehicle equations of motion, wheel equation of motion and *Magic Formula* tire model was established. On the basis of the literature review and full vehicle model, three types of DYC systems have been proposed with detailed design processes and simulation verifications. These systems are the yaw rate-based DYC, vehicle side-slip-based DYC and simultaneous control of the yaw rate and vehicle side-slip.

To clarify the basic question on how the corrective yaw moment generated by a DYC system changes the vehicle dynamics, a mathematical relationship was derived from the vehicle equations of motion to show how the steady-state yaw rate response depends on the torque difference between the two driving motors (i.e. the corrective yaw moment). This relationship implies that the steady-state yaw rate can be directly controlled by tuning the torque difference to achieve a reference value. Based on this relationship, a yaw rate-based DYC system was designed to track the desired neutral steer yaw rate response. Comparative simulation results show that the vehicle closely traces the desired yaw rate with the proposed DYC on-board, and the vehicle handling is significantly improved.

Similarly, another mathematical relationship was derived to reveal the effect of a DYC system on the other crucial vehicle state, vehicle side-slip. This relationship demonstrates that the steady-state vehicle side-slip is a function of the torque difference between the left and right driving motors. On the basis of this relationship, a vehicle side-slip-based DYC solution was proposed to achieve zero vehicle side-slip. Simulation results manifest that the vehicle side-slip is minimized by the proposed DYC system. As a result, the vehicle stability and driver's sense of control are greatly enhanced.

After dealing with the yaw rate and vehicle side-slip individually, an integrated sliding mode control scheme which employs the yaw rate and vehicle side-slip simultaneously as the control variables was devised. This design introduces a novel switching function that guarantees the simultaneous convergences of both the yaw rate and vehicle side-slip errors to zero, and eliminates the limitations presented in the common sliding mode DYC solutions. Extensive simulations demonstrate that the proposed sliding mode DYC approach is effective in suppressing both the yaw rate and vehicle side-slip errors in various driving scenarios, and it outperforms the common sliding mode DYC schemes in terms of tracking the desired yaw rate, vehicle path and vehicle side-slip. The simultaneous regulation of the yaw rate and vehicle side-slip by the proposed DYC method effectively enhances both the vehicle handling and stability.

7.2 RECOMMENDATIONS

Throughout this thesis, all research questions raised in Chapter 1 have been answered and the research objectives have been achieved. However, in the light of the work carried out in this study, some possible areas are thought worthy of further investigation.

It is recommended that experimentation be performed to validate and improve the proposed schemes further. For each control method, firstly, Hardware-In-the-Loop (HIL) simulations should be conducted to check and regulate the control law in the Electronic Control Unit (ECU). Then, field tests should be performed using the same vehicle maneuvers as in the simulations to evaluate the control scheme thoroughly. Based on the HIL simulation and field testing results, possible adjustments and improvements can be made to the control design.

The scope of this study has been narrowed down to the DYC systems for electric vehicles (or hybrid vehicles) with two rear independent driving motors. The control schemes proposed in this thesis can also be applied to 4WD electric vehicles. With four independent driving motors on-board, the problem of appropriate distribution of the motor torques to generate a certain corrective yaw moment needs to be tackled. The proposed DYC methods for 2-Wheel-Drive (2WD) vehicles, also known as the upper level control, can be employed to compute the target corrective yaw moment for 4WD vehicles. Then this yaw moment should be realized by allocating an appropriate torque to each driving motor based on the torque distribution strategy. So far, a large number of upper level control methods have been proposed, however there are not sufficient torque distribution strategies available in the literature. It is suggested that further research be conducted to design an effective torque distribution strategy, in order to extend the proposed upper level control schemes to 4WD electric vehicles.

In the recent literature, some control solutions integrate DYC system with other types of vehicle dynamics control systems such as AFS, 4WS and ARCS. It is known that a certain vehicle dynamics control system is most effective in a specific region. The integrated control systems take advantage of each type of vehicle dynamics control system, and ensure satisfactory control performance in a wide range of driving condition. The proposed DYC methods in this thesis are able to work in tandem with other vehicle dynamics control systems, and the design of an appropriate integrating strategy should be studied in the future.

Furthermore, a challenge confronted in this study is that different vehicle equations of motion and tire models are available in the literature, and they need to be carefully selected, combined and possibly modified to establish a suitable full vehicle model. The experience learned from this challenge is that the subsystems in the full vehicle model

must be mathematically and physically compatible, i.e. they do not contradict each other. It is also suggested that computer simulations of different full vehicle models be performed, and the simulation results be compared with the field test data to check the validity of these vehicle models. By this means, an optimal full vehicle model can possibly be found out.

Last but not least, there are not sufficient review articles available in the literature introducing DYC designs for electric and hybrid vehicles with independent motors. It is recommended that comprehensive review papers be written to sum up the state-of-the-art DYC designs, in order to facilitate further research in this field.

Appendix

MAIN M-FILE

clear;

%vehicle parameters

```
m = 318;            %total mass
m_s = 283;          %sprung mass
d_f = 1.14400;      %front track
d_r = 1.15266;      %rear track
I_z = 1000;         %total yaw moment of inertia, previously 250
I_x = 200;          %total roll moment of inertia, previously 18.43
l = 1.55;           %R10 l=1.65
l_f = 0.78475;      %R10 a1=0.96, petrol a1=0.850
l_r = 0.76525;      %R10 a2=0.69, petrol a2=0.696
h = 0.26;           %height of COG of the whole car
h_s = 0.04719;      %distance between the sprung mass COG to the unsprung mass COG,
                    previously 0.27175
h_rcf = 0.218;      %height of the front roll center, previously 0.01754
h_rcr = 0.218;      %height of the rear roll center, previously 0.01876
R = 0.218;          %tire radius, R10 R=0.254
J = 2;              %inertia of the driving wheel assembly, kg*m^2
K = 51500.88;       %roll stiffness, R10 k=40177.52, petrol kr=72694.02
K_f = 25750.44;     %front spring stiffness, previously 23432.83
K_r = 25750.44;     %rear spring stiffness, previously 28068.06
C = 3828.71;        %roll damping, previously 6668.91
C_f = 1953.43;      %front shock absorber damping, previously 3415.09
```

C_r = 1875.27;   %rear shock absorber damping, previously 3253.82

F_sf = 770.085;   %front tire static tire load

F_sr = 789.705;   %rear tire static tire load

V_ini = 22.2;   %16.7; %initial speed of the vehicle

%magic formula parameters

F_z0 = 661.15304;   %657.33511;

P_dx1 = 2.5722;   %2.4149;

P_dx2 = -0.21555;   %-0.15154;

P_cx1 = 1.338;   %1.7;

P_ex1 = 0.64992;   %0;

P_ex2 = 0.40397;   %0;

P_ex3 = -0.36698;   %0;

P_ex4 = 0.27059;   %0;

P_kx1 = 68.6146;   %52.8311;

P_kx2 = 0.000005;   %0.000012;

P_kx3 = 0.064062;   %-0.009406;

P_dy1 = 2.507853;   %2.489121;

P_dy2 = -0.154951;   %-0.120498;

P_cy1 = 1.466801;   %1.568288;

P_ey1 = -0.000022;   %-0.01619;

P_ey2 = 0.000004;   %-0.057131;

P_ey3 = -2425.236;   %-1.75437;

P_ky1 = -144.83247;   %-209.32818;

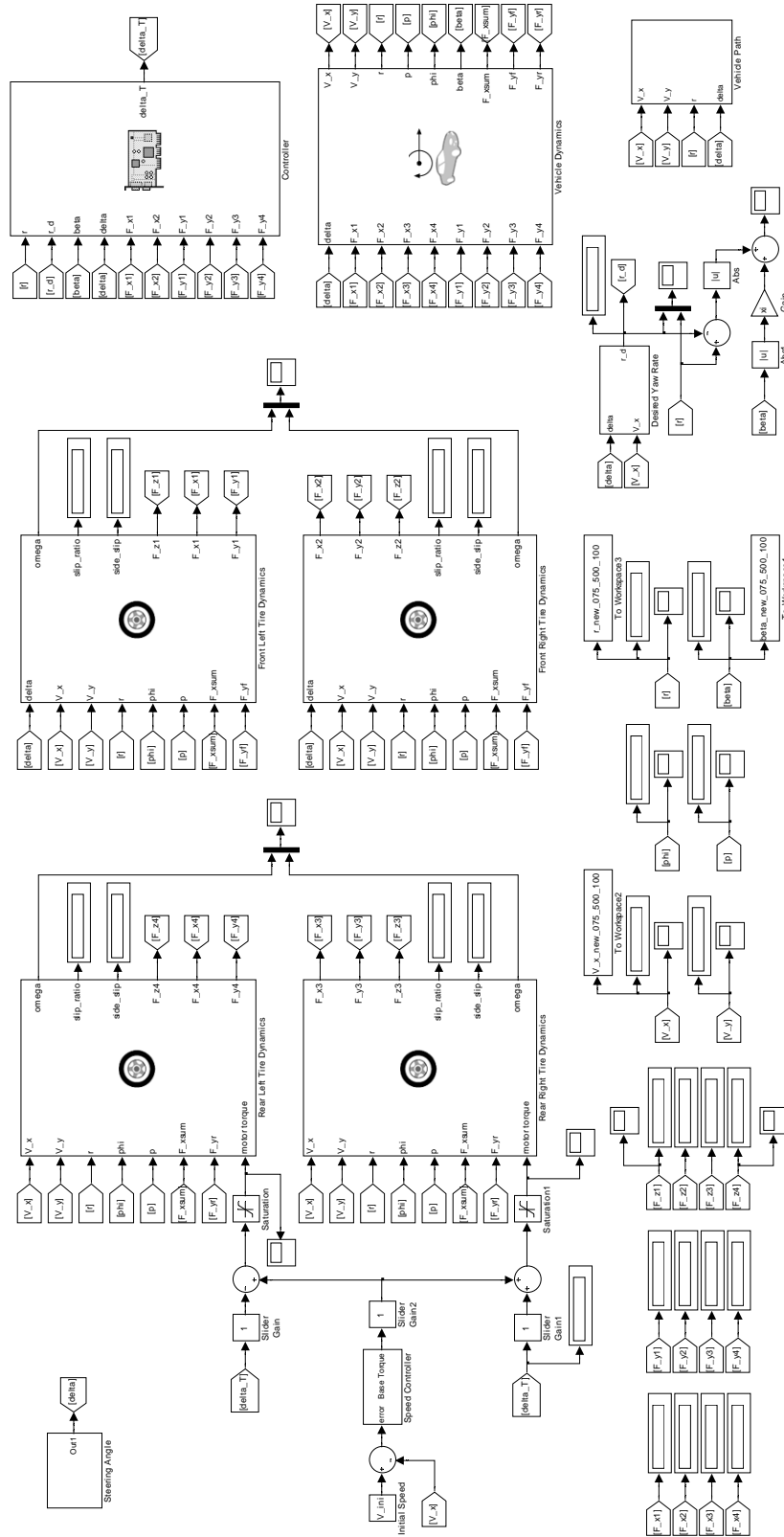P_ky2 = -4.816265;   %-6.138896;

%controller parameters

Kp = 1000;

Ki = 0;

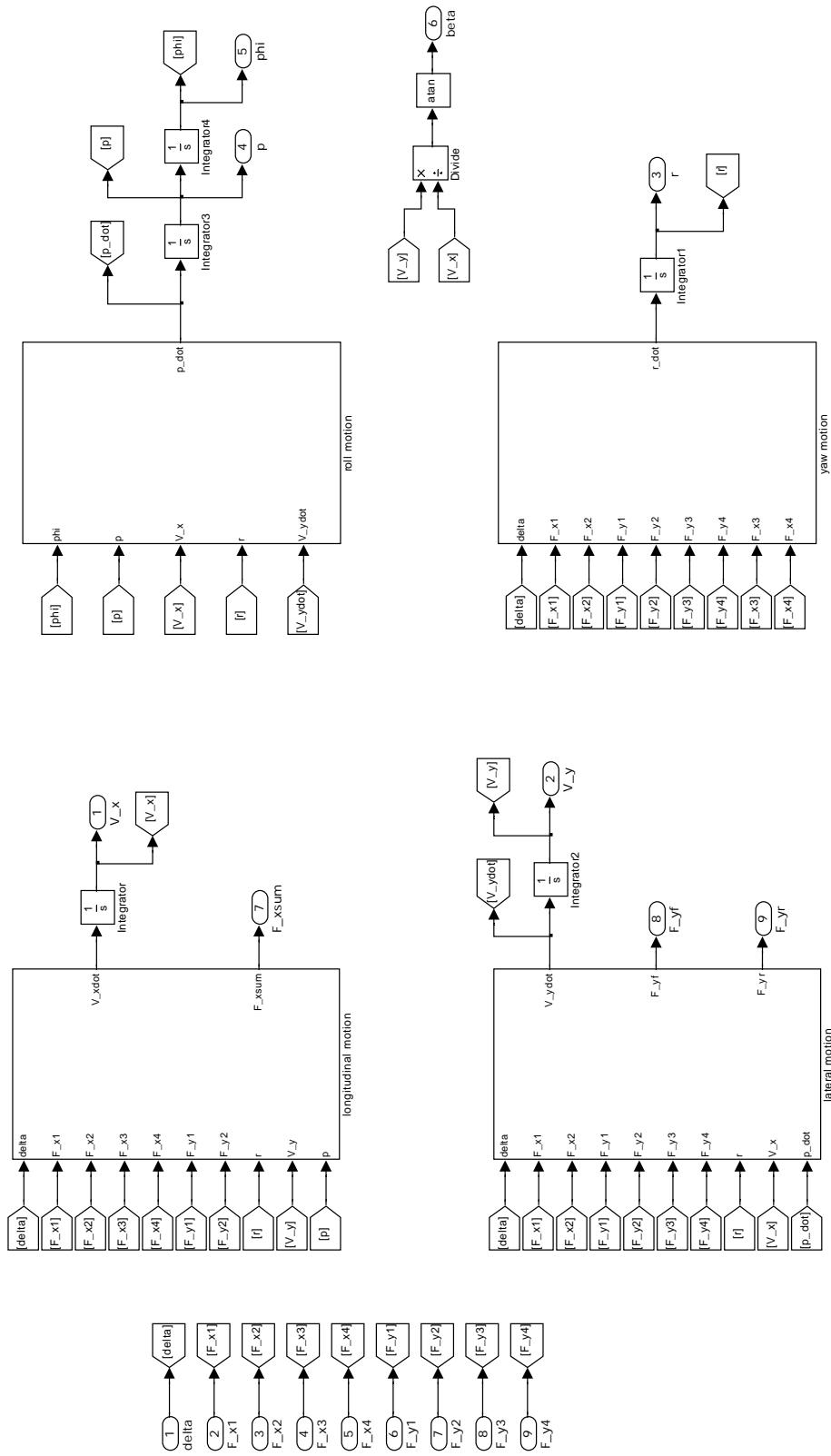Kd = 0;

xi = 5/3;

rho = 500;

boundary = 100;

%start simulation

open_system('new_control_model_7.mdl');

sim('new_control_model_7.mdl');

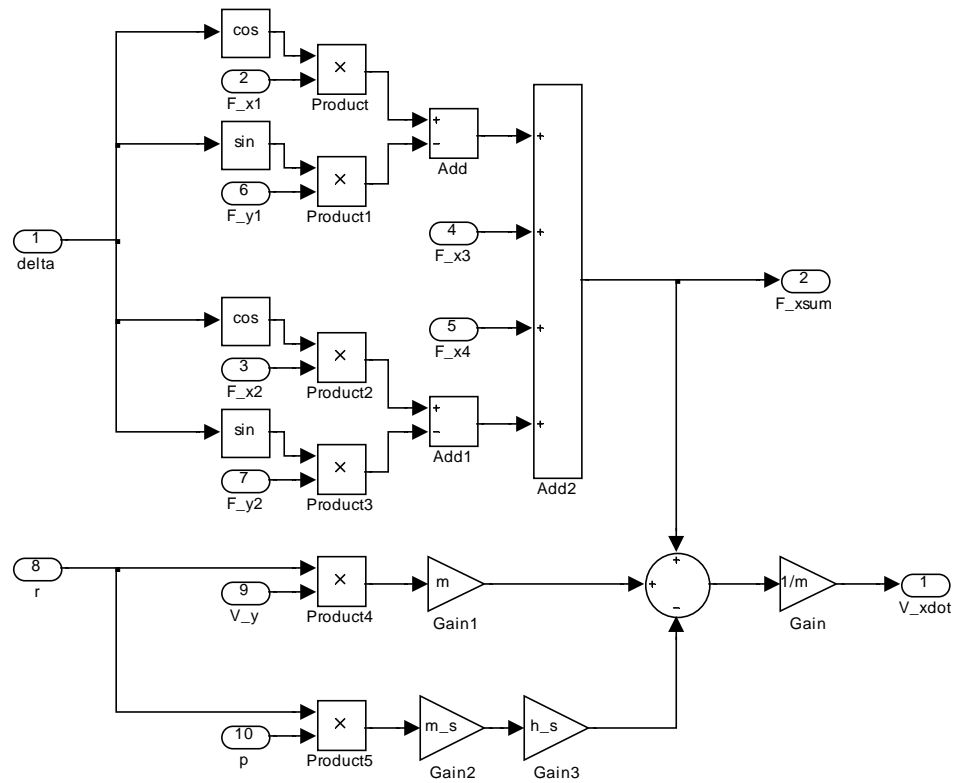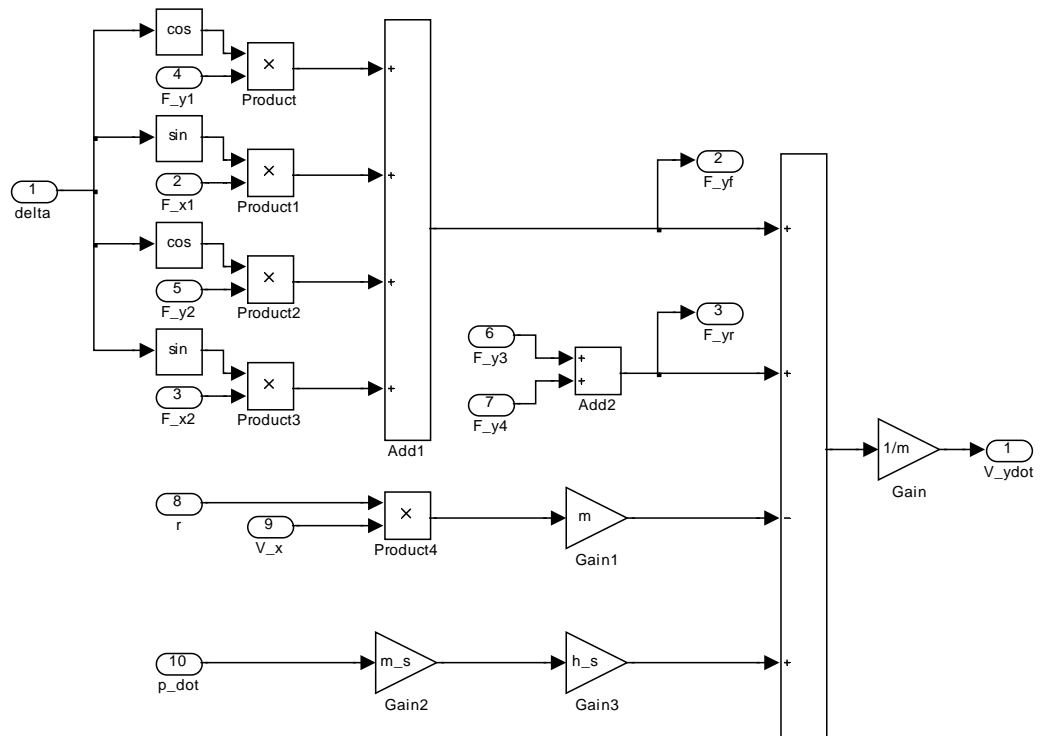# SIMULATION MODEL OVERVIEW (TURNED 90°)
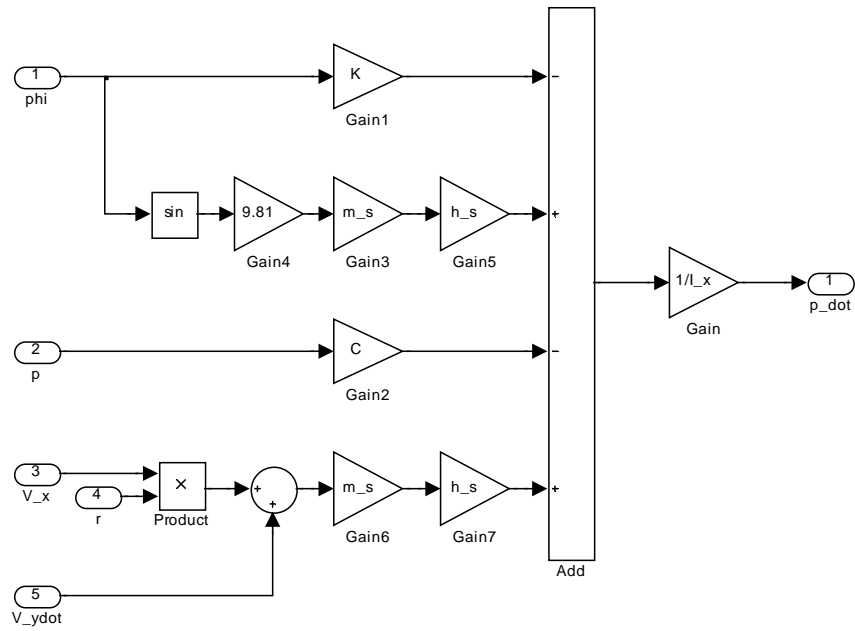
VEHICLE DYNAMICS SYSTEM (TURNED 90°)

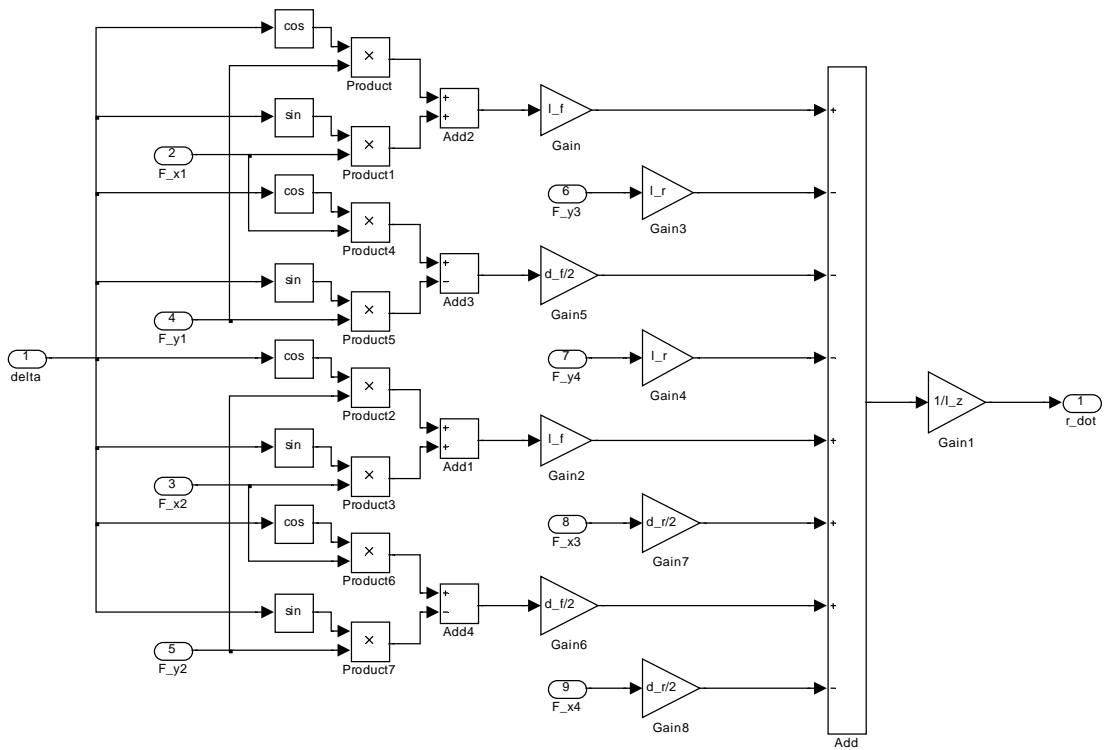## VEHICLE LONGITUDINAL MOTION SUBSYSTEM

VEHICLE LATERAL MOTION SUBSYSTEM

VEHICLE ROLL MOTION SUBSYSTEM

VEHICLE YAW MOTION SUBSYSTEM

DRIVING WHEEL SYSTEM (TURNED 90°)
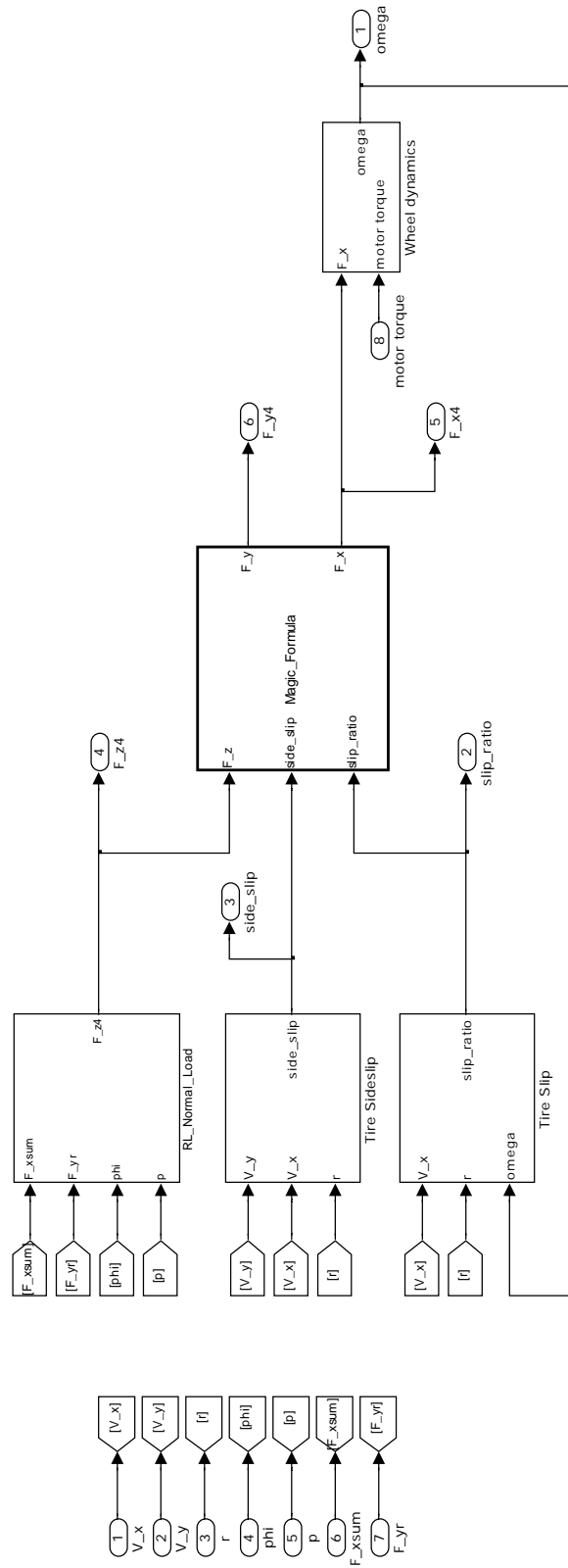
WHEEL NORMAL LOAD SUBSYSTEM
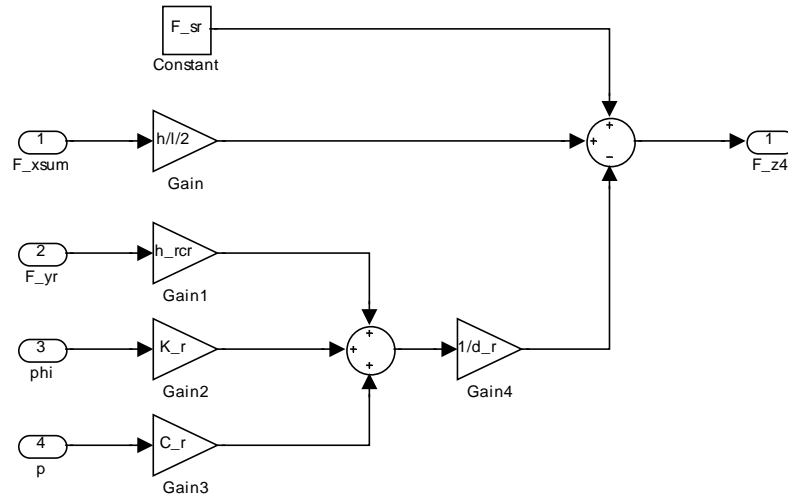
TIRE SLIP ANGLE SUBSYSTEM
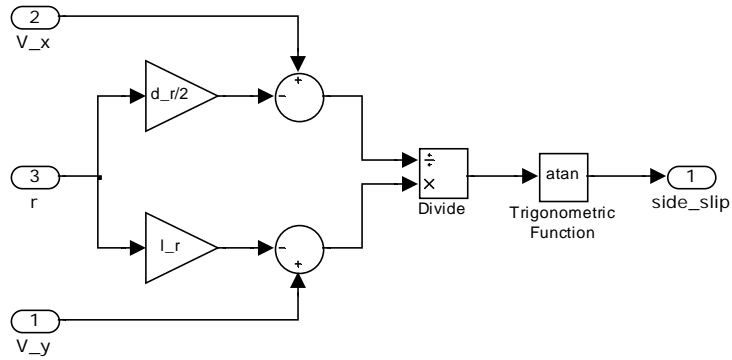
WHEEL SLIP RATIO SUBSYSTEM
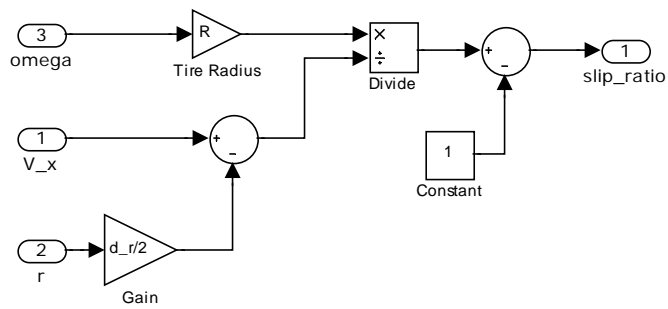
WHEEL DYNAMICS SUBSYSTEM
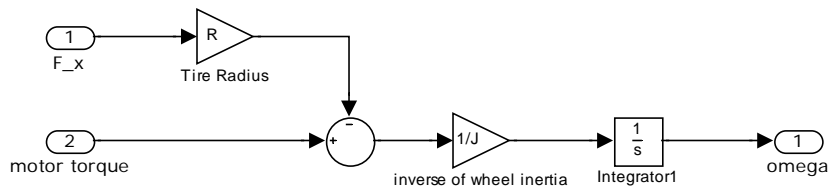
EMBEDDED FUNCTION FOR MAGIC FORMULA

function [F_y,F_x] = Magic_Formula(F_z, side_slip, slip_ratio, F_z0, P_dx1, P_dx2, P_cx1, P_ex1, P_ex2, P_ex3, P_ex4, P_kx1, P_kx2, P_kx3, P_dy1, P_dy2, P_cy1, P_ey1, P_ey2, P_ey3, P_ky1, P_ky2)

df_z = F_z/F_z0-1;

U_x = P_dx1+P_dx2*df_z;

C_x = P_cx1;

D_x = U_x*F_z;

E_x = (P_ex1+P_ex2*df_z+P_ex3*df_z^2)*(1-P_ex4*sign(slip_ratio));

K_x = F_z*(P_kx1+P_kx2*df_z)*exp(-P_kx3*df_z);

B_x = K_x/C_x/D_x;

F_x = D_x*sin(C_x*atan(B_x*(1-E_x)*slip_ratio+E_x*atan(B_x*slip_ratio)));

U_y = P_dy1+P_dy2*df_z;

C_y = P_cy1;

D_y = U_y*F_z;

E_y = (P_ey1+P_ey2*df_z)*(1-P_ey3*sign(side_slip));

K_y = P_ky1*F_z0*sin(2*atan(F_z/F_z0/P_ky2));

B_y = K_y/C_y/D_y;

F_y = -D_y*sin(C_y*atan(B_y*(1-E_y)*side_slip+E_y*atan(B_y*side_slip)));

CONTROLLER (TURNED $90°$)
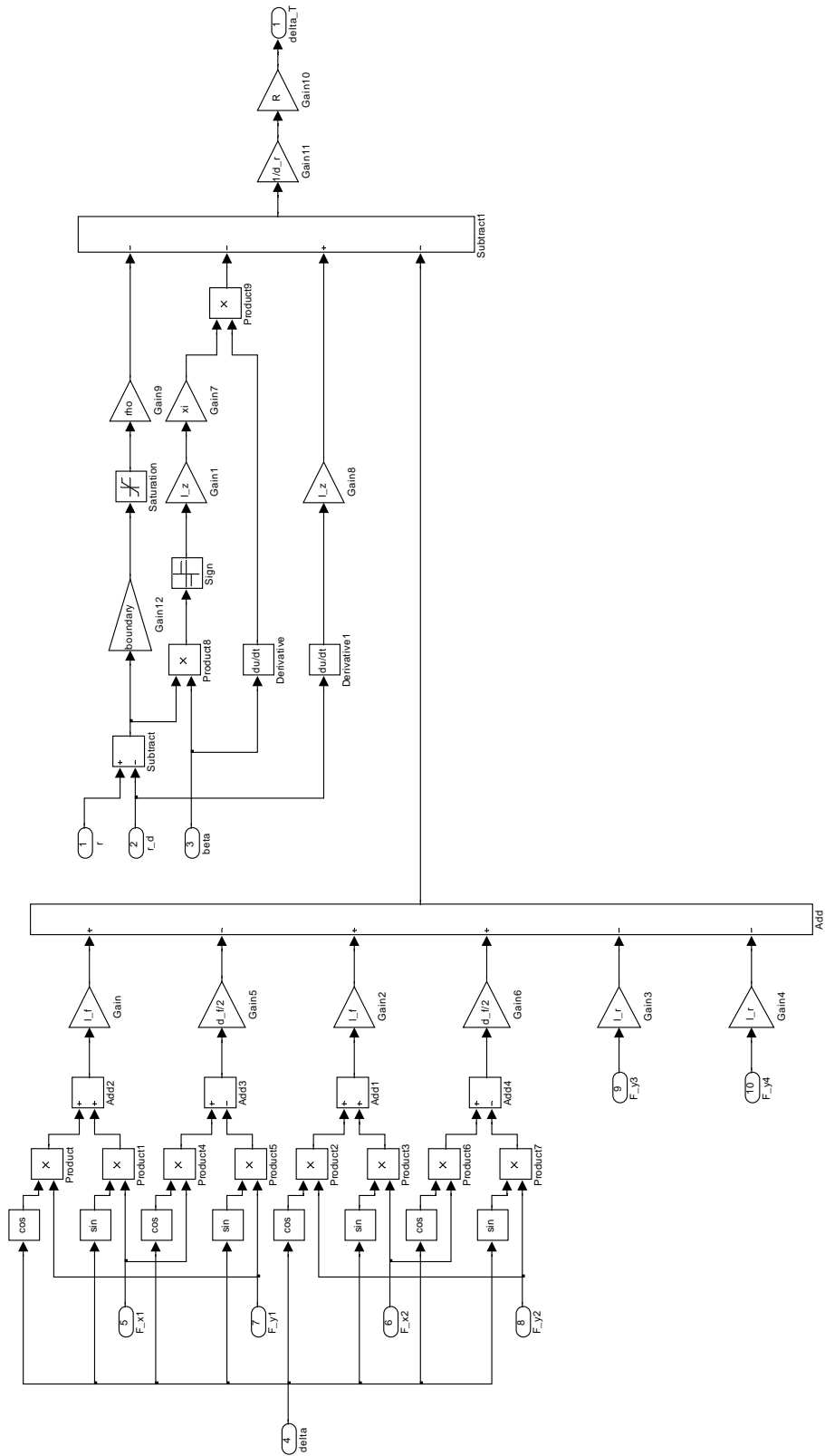
Bibliography

[1] M. Nagai, Y. Hirano, and S. Yamanaka, "Integrated control of active rear wheel steering and direct yaw moment control," *Vehicle System Dynamics*, vol. 27, no. 5-6, pp. 357–370, 1997.

[2] M. Aga and A. Okada, "Analysis of vehicle stability control (VSC)'s effectiveness from accident data," in *Proceedings - 18th International Technical Conference on the Enhanced Safety of Vehicles, ESV 2003*, no. 541, Wahington, DC, United States, 2003.

[3] A. Lie, C. Tingvall, M. Krafft, and A. Kullgren, "The effectiveness of electronic stability control (ESC) in reducing real life crashes and injuries," *Traffic Injury Prevention*, vol. 7, no. 1, pp. 38–43, 2006.

[4] A. Chouinard and J.-F. Lécuyer, "A study of the effectiveness of electronic stability control in canada," *Accident Analysis and Prevention*, vol. 43, no. 1, pp. 451–460, 2011.

[5] E. K. Liebemann, K. Meder, J. Schuh, and G. Nenninger, "Safety and performance enhancement: The bosch electronic stability control (ESP)," *SAE Technical Paper 2004-21-0060*, 2004.

[6] A. T. van Zanten, "Bosch ESP systems: 5 years of experience," *SAE Technical Paper 2000-01-1633*, 2000.

[7] B. Mashadi, S. Mostaani, and M. Majidi, "Vehicle stability enhancement by using an active differential," *Proceedings of the Institution of Mechanical Engineers. Part I: Journal of Systems and Control Engineering*, vol. 225, no. 8, pp. 1098–1114, 2011.

[8] M. Hancock, R. Williams, E. Fina, and M. Best, "Yaw motion control via active differentials," *Transactions of the Institute of Measurement and Control*, vol. 29, no. 2, pp. 137–157, 2007.

[9] M. Canale, L. Fagiano, A. Ferrara, and C. Vecchio, "Vehicle yaw control via second-order sliding-mode technique," *IEEE Transactions on Industrial Electronics*, vol. 55, no. 11, pp. 3908–3916, 2008.

[10] M. Hancock, R. Williams, T. Gordon, and M. Best, "A comparison of braking and differential control of road vehicle yaw-sideslip dynamics," *Proceedings of the Institution of Mechanical Engineers, Part D: Journal of Automobile Engineering*, vol. 219, no. 3, pp. 309–327, 2005.

[11] M. Canale, L. Fagiano, M. Milanese, and P. Borodani, "Robust vehicle yaw control using an active differential and imc techniques," *Control Engineering Practice*, vol. 15, no. 8, pp. 923–941, 2007.

[12] Y. Ushiroda, K. Sawase, N. Takahashi, K. Suzuki, and K. Manabe, "Development of super AYC," *Mitsubishi Motors Technical Review*, vol. 15, pp. 73–76, 2003.

[13] N. Mutoh, "Driving and braking torque distribution methods for front- and rear-wheel-independent drive-type electric vehicles on roads with low friction coefficient," *IEEE Transactions on Industrial Electronics*, vol. 59, no. 10, pp. 3919 – 3933, 2012.

[14] C. Fu, R. Hoseinnezhad, A. Bab-Hadiashar, and R. N. Jazar, "Direct yaw moment control for electric and hybrid vehicles with independent motors," *International Journal of Vehicle Design*, 2014, accepted.

[15] Y. Chen, J. Hedrick, and K. Guo, "A novel direct yaw moment controller for in-wheel motor electric vehicles," *Vehicle System Dynamics*, vol. 51, no. 6, pp. 925–942, 2013.

[16] C. Fu, R. Hoseinnezhad, A. Bab-Hadiashar, R. N. Jazar, and S. Watkins, "Electronic differential for high-performance electric vehicles with independent driving motors," *International Journal of Electric and Hybrid Vehicles*, vol. 6, no. 2, pp. 108–132, 2014.

[17] K. Uematsu and J. C. Gerdes, "A comparison of several sliding surfaces for stability control," in *Proceedings - 6th International Symposium on Advanced Vehicle Control, AVEC 2002*, Hiroshima, Japan, 2002, pp. 601–608.

[18] A. T. van Zanten, R. Erhardt, G. Pfaff, F. Kost, U. Hartmann, and T. Ehret, "Control aspects of the bosch-VDC," in *Proceedings - 3rd International Symposium on Advanced Vehicle Control, AVEC 1996*, Aachen, Germany, 1996, pp. 573–608.

[19] A. T. van Zanten, R. Erhardt, and G. Pfaff, "VDC, the vehicle dynamics control system of bosch," *SAE Technical Paper 950759*, 1995.

[20] R. N. Jazar, *Vehicle Dynamics: Theory and Application.* Springer, 2008, ch. 10, pp. 597–631.

[21] Y. Shibahata, K. Shimada, and T. Tomari, "Improvement of vehicle maneuverability by direct yaw moment control," *Vehicle System Dynamics*, vol. 22, no. 5-6, pp. 465–481, 1993.

[22] C. Fu, R. Hoseinnezhad, R. Jazar, A. Bab-Hadiashar, and S. Watkins, "Electronic differential design for vehicle side-slip control," in *Proceedings - 2012 International Conference on Control, Automation and Information Sciences, ICCAIS 2012*, Ho Chi Minh City, Vietnam, 2012, pp. 306 – 310.

[23] K. Yi, T. Chung, J. Kim, and S. Yi, "An investigation into differential braking strategies for vehicle stability control," *Proceedings of the Institution of Mechanical Engineers, Part D: Journal of Automobile Engineering*, vol. 217, no. 12, pp. 1081–1093, 2003.

[24] R. Tchamna and I. Youn, "Yaw rate and side-slip control considering vehicle longitudinal dynamics," *International Journal of Automotive Technology*, vol. 14, no. 1, pp. 53–60, 2013.

[25] K. R. Buckholtz, "Use of fuzzy logic in wheel slip assignment - part I: Yaw rate control," *SAE Technical Paper 2002-01-1221*, 2002.

[26] ——, "Use of fuzzy logic in wheel slip assignment - part II: Yaw rate control with sideslip angle limitation," *SAE Technical Paper 2002-01-1220*, 2002.

[27] G. A. Magallán, C. H. De Angelo, G. Bisheimer, and G. García, "A neighborhood electric vehicle with electronic differential traction control," in *Proceedings - 34th Annual Conference of the IEEE Industrial Electronics Society, IECON 2008*, Orlando, FL, United states, 2008, pp. 2757–2763.

[28] G. Magallán, C. De Angelo, and G. García, "A neighbourhood-electric vehicle development with individual traction on rear wheels," *International Journal of Electric and Hybrid Vehicles*, vol. 2, no. 2, pp. 115–136, 2009.

[29] P. M. Kelecy and R. D. Lorenz, "Control methodology for single inverter, parallel connected dual induction motor drives for electric vehicles," in *Proceedings - Power Electronics Specialists Conference, PESC'94 Record., 25th Annual IEEE*, vol. 2, Taipei, Taiwan, 1994, pp. 987–991.

[30] F. Profumo, Z. Zhang, and A. Tenconi, "Axial flux machines drives: A new viable solution for electric cars," *IEEE Transactions on Industrial Electronics*, vol. 44, no. 1, pp. 39–45, 1997.

[31] D. Platt and B. Smith, "Twin rotor drive for an electric vehicle," *IEE Proceedings B: Electric Power Applications*, vol. 140, no. 2, pp. 131–138, 1993.

[32] ——, "A twin, composite, axial flux induction machine for an electric vehicle drive," in *Proceedings - Electric Energy Conference 1987: An International Conference on Electric Machines and Drives*, Adelaide, Australia, 1987, pp. 53–56.

[33] B. Smith and D. Platt, "Compound, series, axial flux induction machines. single phase analogy," *IEE Proceedings B: Electric Power Applications*, vol. 137, no. 4, pp. 265–272, 1990.

[34] R. N. Jazar, *Vehicle Dynamics: Theory and Application.* Springer, 2008, ch. 7, pp. 379–395.

[35] M. Abe and W. Manning, *Vehicle Handling Dynamics: Theory and Application*, 1st ed. Oxford, UK: Butterworth-Heinemann, 2009, ch. 3, pp. 47–117.

[36] B. Jin, X. Zhang, and Q. Yang, "Low speed steering differential control model for pure electric vehicle," *Beijing Jiaotong Daxue Xuebao/Journal of Beijing Jiaotong University*, vol. 37, no. 4, pp. 158–161, 2013.

[37] H. Yu, M. Huang, and Z. Zhang, "Experimental research of electronic differential control for in-wheel motor drive electric vehicle," *Wuhan Ligong Daxue Xuebao/Journal of Wuhan University of Technology*, vol. 33, no. 5, pp. 147–151, 2011.

[38] K. Hartani, M. Bourahla, Y. Miloud, and M. Sekkour, "Direct torque control of an electronic differential for electric vehicle with separate wheel drives," *Journal of Automation and Systems Engineering*, vol. 2, no. 2, 2008.

[39] A. Cordeiro, D. Foito, and M. Guerreiro, "A sensolrless speed control system for an electric vehicle without mechanical differential gear," in *Proceedings - 2006 IEEE Mediterranean Electrotechnical Conference, MELECON 2006*, Malaga, Spain, 2006, pp. 1174–1177.

[40] A. Haddoun, M. E. H. Benbouzid, D. Diallo, R. Abdessemed, J. Ghouili, and K. Srairi, "Modeling, analysis, and neural network control of an EV electrical differential," *IEEE Transactions on Industrial Electronics*, vol. 55, no. 6, pp. 2286–2294, 2008.

[41] A. Haddoun, M. Benbouzid, D. Diallo, R. Abdessemed, J. Ghouili, and K. Srairi, "Design and implementation of an electric differential for traction application," in *Proceedings - 2010 IEEE Vehicle Power and Propulsion Conference, VPPC 2010*, Lille, France, 2010, pp. 1–6.

[42] Y.-e. Zhao and J. Zhang, "Modelling and simulation of the electronic differential system for an electric vehicle with two-motor-wheel drive," *International Journal of Vehicle Systems Modelling and Testing*, vol. 4, no. 1-2, pp. 117–131, 2009.

[43] Y. Zhao, J. Zhang, and X. Guan, "Modeling and simulation of electronic differential system for an electric vehicle with two-motor-wheel drive," in *Proceedings - 2009 IEEE Intelligent Vehicles Symposium*, Xi'an, China, 2009, pp. 1209–1214.

[44] F. J. Perez-Pinal, I. Cervantes, and A. Emadi, "Stability of an electric differential for traction applications," *IEEE Transactions on Vehicular Technology*, vol. 58, no. 7, pp. 3224 – 3233, 2009.

[45] A. Nasri, A. Hazzab, I. Bousserhane, S. Hadjeri, and P. Sicard, "Fuzzy logic speed control stability improvement of lightweight electric vehicle drive," *Journal of Electrical Engineering and Technology*, vol. 5, no. 1, pp. 129–139, 2010.

[46] Y. Zhou, S. Li, X. Zhou, and Z. Fang, "The control strategy of electronic differential for EV with four in-wheel motors," in *Proceedings - 2010 Chinese Control and Decision Conference, CCDC 2010*, Xuzhou, China, 2010, pp. 4190–4195.

[47] C. Doniselli, G. Mastinu, and R. Cal, "Traction control for front-wheel-drive vehicles," *Vehicle System Dynamics*, vol. 23, no. SUPPL, pp. 87–104, 1994.

[48] F. Tahami, R. Kazemi, S. Farhanghi, and B. Samadi, "Fuzzy based stability enhancement system for a four-motor-wheel electric vehicle," *SAE Technical Paper 2002-01-1588*, 2002.

[49] S. Motoyama, H. Uki, K. Isoda, and H. Yuasa, "Effect of traction force distribution control on vehicle dynamics," *Vehicle System Dynamics*, vol. 22, no. 5-6, pp. 455–464, 1993.

[50] H. Zhou and Z. Liu, "Vehicle yaw stability-control system design based on sliding mode and backstepping control approach," *IEEE Transactions on Vehicular Technology*, vol. 59, no. 7, pp. 3674–3678, 2010.

[51] K. Nam, S. Oh, H. Fujimoto, and Y. Hori, "Design of adaptive sliding mode controller for robust yaw stabilization of in-wheel-motor-driven electric vehicles," in *Proceedings - 26th Electric Vehicle Symposium 2012, EVS 2012*, vol. 2, Los Angeles, United States, 2012, pp. 1013–1022.

[52] M. Yamamoto, "Active control strategy for improved handling and stability," *SAE Technical Paper 911902*, 1991.

[53] K. Guo and H. Guan, "Modelling of driver/vehicle directional control system," *Vehicle System Dynamics*, vol. 22, no. 3-4, pp. 141–184, 1993.

[54] A. Goodarzi, E. Esmailzadeh, and G. Vossoughi, "Direct yaw moment control for motorized wheel electric vehicles," in *Proceedings of the ASME Design Engineering Technical Conference*, vol. 6 A, Pittsburgh, United States, 2001, pp. 215–222.

[55] Y. lkushima and K. Sawase, "A study on the effects of the active yaw moment control," *SAE Technical Paper 950303*, 1995.

[56] F. Tahami, S. Farhangi, and R. Kazemi, "A fuzzy logic direct yaw-moment control system for all-wheel-drive electric vehicles," *Vehicle System Dynamics*, vol. 41, no. 3, pp. 203–221, 2004.

[57] M. Abe, N. Ohkubo, and Y. Kano, "A direct yaw moment control for improving limit performance of vehicle handling - comparison and cooperation with 4WS," *Vehicle System Dynamics*, vol. 25, no. SUPPL., pp. 3–23, 1996.

[58] S. Inagaki, I. Kshiro, and M. Yamamoto, "Analysis on vehicle stability in critical cornering using phase-plane method," in *Proceedings of the International Symposium on Advanced Vehicle Control 1994*, Tsukuba-shi, Japan, 1994, pp. 287–292.

[59] K. Koibuchi, M. Yamamoto, Y. Fukada, and S. Inagaki, "Vehicle stability control in limit cornering by active brake," *SAE Technical Paper 960487*, 1996.

[60] Y. Yasui, K. Tozu, N. Hattori, and M. Sugisawa, "Improvement of vehicle directional stability for transient steering maneuvers using active brake control," *SAE Technical Paper 960485*, 1996.

[61] Y. Yasui, K. Tozu, N. Hattori, and M. Nishii, "Vehicle stability enhancement system using brake control," in *Proceedings of the FISITA 1996 World Automotive Congress*, Prague, Czech Republic, 1996, pp. 1–6.

[62] J. Tian, Y. Wang, and N. Chen, "Research on vehicle stability based on DYC and AFS integrated controller," *Applied Mechanics and Materials*, vol. 278-280, pp. 1510–1515, 2013.

[63] J. He, D. Crolla, M. Levesley, and W. Manning, "Coordination of active steering, driveline, and braking for integrated vehicle dynamics control," *Proceedings of the Institution of Mechanical Engineers, Part D: Journal of Automobile Engineering*, vol. 220, no. 10, pp. 1401–1421, 2006.

[64] Y. Furukawa and M. Abe, "Direct yaw moment control with estimating side-slip angle by using on-board-tire-model," in *Proceedings - 4th International*

Symposium on Advanced Vehicle Control, AVEC 1998, Nagoya, Japan, 1998, pp. 431–436.

[65] ——, "On-board-tire-model reference control for cooperation of 4WS and direct yaw moment control for improving active safety of vehicle handling," in *Proceedings - 3rd International Symposium on Advanced Vehicle Control, AVEC 1996*, Aachen, Germany, 1996, pp. 507–526.

[66] M. Abe, Y. Kano, K. Suzuki, Y. Shibahata, and Y. Furukawa, "Side-slip control to stabilize vehicle lateral motion by direct yaw moment," *JSAE Review*, vol. 22, no. 4, pp. 413–419, 2001.

[67] M. Abe, Y. Kano, Y. Shibahata, and Y. Furukawa, "Improvement of vehicle handling safety with vehicle side-slip control by direct yaw moment," *Vehicle System Dynamics*, vol. 33, no. SUPPL., pp. 665–679, 1999.

[68] M. Abe, "Vehicle dynamics and control for improving handling and active safety: From four-wheel steering to direct yaw moment control," *Proceedings of the Institution of Mechanical Engineers, Part K: Journal of Multi-body Dynamics*, vol. 213, no. 2, pp. 87–101, 1999.

[69] G. Baffet, A. Charara, and G. Dherbomez, "An observer of tire-road forces and friction for active security vehicle systems," *IEEE/ASME Transactions on Mechatronics*, vol. 12, no. 6, pp. 651–661, 2007.

[70] M. Doumiati, A. Victorino, A. Charara, and D. Lechner, "Onboard real-time estimation of vehicle lateral tire-road forces and sideslip angle," *IEEE/ASME Transactions on Mechatronics*, vol. 16, no. 4, pp. 601–614, 2011.

[71] Y. Fukada, "Slip-angle estimation for vehicle stability control," *Vehicle System Dynamics*, vol. 32, no. 4, pp. 375–388, 1999.

[72] F. Lin and C. Huang, "State-of-the-art of vehicle side slip angle estimation," *Zhongguo Jixie Gongcheng/China Mechanical Engineering*, vol. 24, no. 1, pp. 135–141, 2013.

[73] K. Nam, S. Oh, H. Fujimoto, and Y. Hori, "Estimation of sideslip and roll angles of electric vehicles using lateral tire force sensors through RLS and Kalman filter

approaches," *IEEE Transactions on Industrial Electronics*, vol. 60, no. 3, pp. 988–1000, 2013.

[74] H. Tseng, B. Ashrafi, D. Madau, T. Brown, and D. Recker, "The development of vehicle stability control at Ford," *IEEE/ASME Transactions on Mechatronics*, vol. 4, no. 3, pp. 223–234, 1999.

[75] A. Fazeli, M. Zeinali, and A. Khajepour, "Application of adaptive sliding mode control for regenerative braking torque control," *IEEE/ASME Transactions on Mechatronics*, vol. 17, no. 4, pp. 745–755, 2012.

[76] R. Kazemi and A. Janbakhsh, "Nonlinear adaptive sliding mode control for vehicle handling improvement via steer-by-wire," *International Journal of Automotive Technology*, vol. 11, no. 3, pp. 345–354, 2010.

[77] J.-J. E. Slotine and W. Li, *Applied Nonlinear Control.* Prentice-Hall, 1991, ch. 7, pp. 276–307.

[78] J. Li and X. Cui, "Steering stability improvement of electric vehicle by DYC based on new target defination," in *Proceedings - IEEE International Conference on Intelligent Computing and Intelligent Systems, ICIS 2009*, vol. 2, Shanghai, China, 2009, pp. 457–461.

[79] S. Yim and K. Yi, "Design of active roll control system and integrated chassis control for hybrid 4WD vehicles," in *Proceedings - 14th International IEEE Conference on Intelligent Transportation Systems, ITSC 2011*, Washington, DC, USA, 2011, pp. 1193–1198.

[80] B. Mashadi and M. Majidi, "Integrated AFS/DYC sliding mode controller for a hybrid electric vehicle," *International Journal of Vehicle Design*, vol. 56, no. 1-4, pp. 246–269, 2011.

[81] H. Zhang and J. Zhang, "Yaw torque control of electric vehicle stability," in *Proceedings - IEEE 6th International Conference on Information and Automation for Sustainability, ICIAfS 2012*, Beijing, China, 2012, pp. 318–322.

[82] Y. e Zhao and J. Zhang, "Yaw stability control of a four-independent-wheel drive electric vehicle," *International Journal of Electric and Hybrid Vehicles*, vol. 2, no. 1, pp. 64–76, 2009.

[83] O. Mokhiamar and M. Abe, "Simultaneous optimal distribution of lateral and longitudinal tire forces for the model following control," *Journal of Dynamic Systems, Measurement and Control, Transactions of the ASME*, vol. 126, no. 4, pp. 753–763, 2004.

[84] B. Kwak and Y. Park, "Robust vehicle stability controller based on multiple sliding mode control," *SAE Technical Paper 2001-01-1060*, 2001.

[85] T. Yoshioka, T. Adachi, T. Butsuen, H. Okazaki, and H. Mochizuki, "Application of sliding-mode control to control vehicle stability," in *Proceedings - 4th International Symposium on Advanced Vehicle Control, AVEC 1998*, Nagoya, Japan, 1998, pp. 455–460.

[86] ——, "Application of sliding-mode theory to direct yaw-moment control," *JSAE review*, vol. 20, no. 4, pp. 523–529, 1999.

[87] R. Chumsamutr and T. Fujioka, "Improvement of electric vehicle's cornering performance by direct yaw moment control," in *Proceedings - 5th International Symposium on Advanced Vehicle Control, AVEC 2000*, Ann Arbor, Michigan, USA, 2000, pp. 49–55.

[88] A. Goodarzi, B. Naderkhani, and E. Esmailzadeh, "Direct yaw moment controller design for vehicle dynamic control systems," in *Proceedings of the IASTED International Conference on Modelling, Simulation and Optimatization*, Banff, Alberta, Canada, 2003, pp. 120–124.

[89] C. Geng, L. Mostefai, M. Denai, and Y. Hori, "Direct yaw-moment control of an in-wheel-motored electric vehicle based on body slip angle fuzzy observer," *IEEE Transactions on Industrial Electronics*, vol. 56, no. 5, pp. 1411–1419, 2009.

[90] M. Shino, N. Miyamoto, Y. Wang, and M. Nagai, "Traction control of electric vehicles considering vehicle stability," in *Proceedings - 6th International Workshop on Advanced Motion Control, AMC 2000*, Nagoya, Japan, 2000, pp. 311–316.

[91] M. Shino and M. Nagai, "Yaw-moment control of electric vehicle for improving handling and stability," *JSAE Review*, vol. 22, no. 4, pp. 473–480, 2001.

[92] M. Nagai, M. Shino, and F. Gao, "Study on integrated control of active front steer angle and direct yaw moment," *JSAE Review*, vol. 23, no. 3, pp. 309–315, 2002.

[93] Y. Zhao, Y. Zhang, and Y. Zhao, "Stability control system for four-in-wheel-motor drive electric vehicle," in *Proceedings - 6th International Conference on Fuzzy Systems and Knowledge Discovery, FSKD 2009*, vol. 4, Tianjin, China, 2009, pp. 171–175.

[94] D. Kim, S. Hwang, and H. Kim, "Vehicle stability enhancement of four-wheel-drive hybrid electric vehicle using rear motor control," *IEEE Transactions on Vehicular Technology*, vol. 57, no. 2, pp. 727–735, 2008.

[95] T. Sun, H. Guo, J.-y. Cao, L.-j. Chai, and Y.-d. Sun, "Study on integrated control of active front steering and direct yaw moment based on vehicle lateral velocity estimation," *Mathematical Problems in Engineering*, vol. 2013, 2013.

[96] M. Abe and W. Manning, *Vehicle Handling Dynamics: Theory and Application*, 1st ed.   Oxford, UK: Butterworth-Heinemann, 2009, ch. 1, pp. 1–3.

[97] ——, *Vehicle Handling Dynamics: Theory and Application*, 1st ed.   Oxford, UK: Butterworth-Heinemann, 2009, ch. 6, pp. 165–198.

[98] H. Baruh, *Analytical Dynamics*.   WCB/McGraw-Hill, 1999, ch. 2, pp. 97–127.

[99] ——, *Analytical Dynamics*.   WCB/McGraw-Hill, 1999, ch. 8, pp. 431–443.

[100] R. Rajamani, G. Phanomchoeng, D. Piyabongkarn, and J. Lew, "Algorithms for real-time estimation of individual wheel tire-road friction coefficients," *IEEE/ASME Transactions on Mechatronics*, vol. 17, no. 6, pp. 1183–1195, 2012.

[101] C. Lee, K. Hedrick, and K. Yi, "Real-time slip-based estimation of maximum tire-road friction coefficient," *IEEE/ASME Transactions on Mechatronics*, vol. 9, no. 2, pp. 454–458, 2004.

[102] K. Nam, H. Fujimoto, and Y. Hori, "Advanced motion control of electric vehicles based on robust lateral tire force control via active front steering," *IEEE/ASME Transactions on Mechatronics*, vol. 19, no. 1, pp. 289–299, 2014.

[103] H. B. Pacejka and I. J. M. Besselink, "Magic formula tyre model with transient properties," *Vehicle System Dynamics*, vol. 27, no. Suppl, pp. 234–249, 1997.

[104] H. B. Pacejka, *Tire and Vehicle Dynamics*, 3rd ed. SAE International, 2012, ch. 2, pp. 61–68.

[105] L. Segel, "Theoretical prediction and experimental substantiation of the response of the automobile to steering control," *Proceedings of the Institution of Mechanical Engineers: Automobile Division*, vol. 10, no. 1, pp. 310–330, 1956.

[106] R. N. Jazar, *Vehicle Dynamics: Theory and Application.* Springer, 2008, ch. 3, pp. 135–145.

[107] ——, *Vehicle Dynamics: Theory and Application.* Springer, 2008, ch. 11, pp. 666–684.

[108] I. Karogal and B. Ayalew, "Independent torque distribution strategies for vehicle stability control," *SAE Technical Paper 2009-01-0456*, 2009.

[109] D. E. Smith and J. M. Starkey, "Effects of model complexity on the performance of automated vehicle steering controllers: controller development and evaluation," *Vehicle System Dynamics*, vol. 23, no. 8, pp. 627–645, 1994.

[110] W. F. Milliken and D. L. Milliken, *Race Car Vehicle Dynamics.* Warrendale, PA, U.S.A.: SAE International c1995, 1995, ch. 2, pp. 24–25.

[111] L. Imsland, T. Johansen, T. Fossen, H. Fjær Grip, J. Kalkkuhl, and A. Suissa, "Vehicle velocity estimation using nonlinear observers," *Automatica*, vol. 42, no. 12, pp. 2091–2103, 2006.

[112] E. M. Kasprzak and D. Gentz, "The formula SAE tire test consortium-tire testing and data handling," *SAE Technical Paper 2006-01-3606*, 2006.

[113] D. Piyabongkarn, R. Rajamani, J. A. Grogg, and J. Y. Lew, "Development and experimental evaluation of a slip angle estimator for vehicle stability control," *IEEE Transactions on Control Systems Technology*, vol. 17, no. 1, pp. 78–88, 2009.

[114] D. W. Pi, N. Chen, J. X. Wang, and B. J. Zhang, "Design and evaluation of sideslip angle observer for vehicle stability control," *International Journal of Automotive Technology*, vol. 12, no. 3, pp. 391–399, 2011.

[115] C. Fu, R. Hoseinnezhad, S. Watkins, and R. Jazar, "Direct torque control for electronic differential in an electric racing car," in *Proceedings - 4th International Conference on Sustainable Automotive Technologies 2012, ICSAT 2012*, Melbourne, Australia, 2012, pp. 177–183.

[116] D. E. Smith and J. M. Starkey, "Effects of model complexity on the performance of automated vehicle steering controllers: model development, validation and comparison," *Vehicle System Dynamics*, vol. 24, no. 2, pp. 163–181, 1995.